IChF
Institute of Physical Chemistry PAS

PhD Thesis

Theory and Computer Simulations of Systems Driven Out-of-Equilibrium by Local Energy Pumping

---

Yirui Zhang

IChF
Institute of Physical Chemistry PAS

POLISH ACADEMY OF SCIENCES

DOCTORAL THESIS

Theory and computer simulations of systems driven out-of-equilibrium by local energy pumping

---

Author:
Yirui ZHANG

Supervisor:
Dr. hab. Anna MACIOŁEK

A thesis submitted in fulfilment of the requirements
for the degree of Doctor of Philosophy

in the

Institute of Physical Chemistry
Polish Academy of Sciences

Warsaw May 17, 2021

This thesis was prepared within the International Ph.D. Studies of the Institute of Physical Chemistry of the Polish Academy of Sciences. Address: ul. Kasprzaka 44/52, 01-224 Warsaw

Theory and computer simulations of systems driven out-of-equilibrium by local energy pumping

by

Yirui ZHANG

"There are naive questions, tedious questions, ill-phrased questions, questions put after inadequate self-criticism. But every question is a cry to understand the world. There is no such thing as a dumb question. "

Carl Sagen

Abstract

Nonequilibrium phenomena are ubiquitous around us, present in both natural and artificial systems. A better understanding of nonequilibrium physics, and ultimately discovering an underlying theoretical framework, is both intriguing and essential. The last few decades have seen a development of the field on various fronts, which has expanded our understanding substantially. However, an underlying framework remains a mystery.

In this thesis, we approach this subject from the perspective of nonequilibrium thermodynamics. In particular, we search for variational principles by proposing hypotheses and then testing these hypotheses using various models. If a hypothesis is disproved by any test model, it is discarded, and a new hypothesis or an improved one is proposed instead. The test models are diverse in nature and are studied using distinct methods, including the ideal gas model, which is studied analytically, and the Ising model, which is studied using simulations. These models are driven to nonequilibrium steady states (NESS) by various energy supply schemes, including periodic (in time) and inhomogeneous (in space) supplies.

A major part of the thesis is devoted to the propositions of variational principles, or more precisely, of certain quantities hypothesized to be minimized in NESS. Among these propositions, three are extensively studied. The development of these quantities follows a chronological order – each hypothesis is built on the last. We start from a quantity $\mathcal{T}$, defined as the ratio of the stored energy to the total heat flow. This quantity is then adapted to a function of the energy and the heat flow. Finally, we come to a quantity analogous to the Helmholtz free energy, with an additional parameter proportional to $\mathcal{T}$.

In addition, using the Ising model, we study the energy storage at steady states under different methods of energy supply. We find that energy storage is sensitive to the details of the supply method, and energy is more effectively stored with rare and large deliveries than frequent and small deliveries.

Lastly, we discover a simple model that exhibits continuous nonequilibrium phase transitions and (beyond the critical point) multiple steady states. The model is an ideal gas with an adiabatic movable wall as the internal constraint and is driven to NESS by a homogeneous energy supply.

Contents

List of Publications

Some materials of this thesis have been published in peer-reviewed journals:

- Robert Hołyst, Anna Maciołek, Yirui Zhang, Marek Litniewski, Piotr Knychała, Maciej Kasprzak, and Michał Banaszak
  Flux and storage of energy in nonequilibrium stationary states
  Phys. Rev. E **99**, 042118 (2019) [1]

  Sections 2.2.1, 2.2.2, and 2.3.3 partially overlap or are equivalent with this publication.

- Yirui Zhang, Robert Hołyst, and Anna Maciołek
  Energy storage in steady states under cyclic local energy input
  Phys. Rev. E **101**, 012127 (2020) [2]

  Section 2.4 partially overlaps or is equivalent to this publication.

- Yirui Zhang, Konrad Giżyński, Anna Maciołek, and Robert Hołyst
  Storage of energy in constrained non-equilibrium systems
  Entropy **22**, 557 (2020) [3]

  Sections 2.2.1, 2.3.1 and 2.3.2 partially overlap or are equivalent with this publication.

Some materials are in preparation for submission and can be found in *arXiv*:

- Yirui Zhang, Marek Litniewski, Karol Makuch, Paweł Żuk, Anna Maciołek, and Robert Hołyst
  Continuous non-equilibrium transition driven by the heat flow
  arXiv: 2103.12765 [4]

  Section 4.1 and Chapter 5 partially overlap or are equivalent with this publication.

Chapter 1

Introduction

Nonequilibrium physics, as indicated by the term, deals with systems and processes that are not in equilibrium. This is a vast topic, as it can be argued that most processes (if not all) are nonequilibrium processes [5]. Hence, nonequilibrium physics contains the study of abundant processes across various scales.

It is well known that physics studies systems that are very large and very small. If we separate systems according to their scales, then relativity deals with macroscopic systems like the universe; quantum mechanics deals with microscopic systems like a hydrogen atom [6, 7]. However, most systems are in between these scales and usually consist of a large collection of particles. This vast range of systems contain, for example, macroscopic systems like the human body or the climate; mesoscopic systems like active matter [8]; biological systems and processes like molecular machines [9] and mRNA transcriptions [10]. Such systems and phenomena are the recent focus of nonequilibrium physics.

To study these systems and processes theoretically, statistical physics is essential, as it bridges the gap between various scales. Experimentally, the recent advancement of experimental techniques makes it possible to probe and control systems on mesoscopic and microscopic scales [11, 12].

Overview of the History [13]

From the early stage to the current frontier, the development of nonequilibrium physics can be roughly divided into three phases. The first phase is the phase of equilibrium thermodynamics, which starts around the 18th and 19th centuries. The development of thermodynamics during this time is driven by the invention of the steam engine and accompanies the first industrial revolution. Indeed, one important goal was to increase heat engine efficiency, which eventually leads to the discovery of the Carnot cycle [14]. Later, the central results of thermodynamics are summarised into the three laws of thermodynamics. This phase is concluded with the development of equilibrium statistical mechanics. Originated by Boltzmann and later highlighted by Gibbs [15], statistical mechanics explains the thermodynamic relations from the microscopic perspective. The central result, the statistical interpretation of a mysterious thermodynamic quantity – entropy – was given by Boltzmann as a measure of the state space volume.

The second phase is the phase of early nonequilibrium thermodynamics, developed during the past century [16–19]. This phase focuses on systems and processes close to equilibrium or within the *linear regime*. Examples of these processes are relaxation processes and equilibrium processes under small perturbations. Already from Boltzmann's H-theorem, attempts have been made to describe nonequilibrium processes [20]. Central results in this phase include linear irreversible thermodynamics, where the entropy production rate is given in the form of fluxes and affinities [16, 17, 21]. Moreover, phenomenological arguments lead to the formulation of the fluctuation-dissipation theorem (FDT), which is later formally derived within the linear response theory [22–24]. New mathematical tools are incorporated in this phase, most notably from stochastic dynamics: the Langevin equation, Markov processes, the Master equation, and much more [25, 26]. These tools are, of course, applicable beyond linear regimes.

The latest phase is marked by the development of stochastic thermodynamics during the last two to three decades. Within this phase, the range of study has been extended to small open systems with large fluctuations (an external heat-bath is still well defined), such as molecular motors, nano-devices, and chemical reactions [27, 28]. And the processes can be arbitrarily far away from equilibrium rather than limited to the linear regime.

In the beginning, various fluctuation theorems (FT) have been proved [29–34]. These theorems are also valid in deep nonequilibrium regimes. Independently, various attempts have been made to generalise FDT into nonequilibrium steady states (NESS) [24, 35, 36]. These results are later incorporated into the framework of stochastic thermodynamics, where a consistent derivation is provided [9, 36]. The central idea of stochastic thermodynamics is to generalise work, heat, and entropy onto trajectory levels. And interestingly, the entropy production is linked to a measure of time-asymmetry. The important mathematical techniques involved in this phase are path integrals and large deviations [37].

Just recently, within stochastic thermodynamics, the so-called *uncertainty relations* have been discovered. These relations show that the fluctuations of the currents are bounded by the entropy production rate [38–41]. Furthermore, a measure of the time-symmetric features of the process, termed *frenesy*, has been proposed by Maes [9, 42]. It is argued that the full framework of nonequilibrium physics would include both the time-symmetric quantity (frenesy) and the time-symmetry breaking quantity (entropy production). Under this scheme, the response theory (both linear and non-linear) can be proved systematically [36, 42]. Lastly, due to the similarity of Shannon entropy and the Gibbs entropy from statistical mechanics, the link between information theory and statistical physics has been explored. Notably, Jaynes provided an information interpretation (using inference) of the maximum entropy principle [43–45]. This idea has recently been extended by Polettini and Esposito in [46].

Scope and Structure of This Thesis

Nonequilibrium physics is an interesting and lively research area. Yet, despite the various advancements described above, a general framework remains a mystery. In this thesis, we approach the subject from the perspective of nonequilibrium thermodynamics, particularly variational principles. We wish to develop a framework similar to equilibrium thermodynamics.

As a starting point, we will focus on nonequilibrium steady states: the properties of the system do not change (like equilibrium states), but time-symmetry is not required. Our methodology mimics the development of thermodynamics: various hypotheses are proposed, each with a well-defined state function; each hypothesis is then examined over different test models. These test models are driven by various methods of energy supply, which can be space-time dependent. It is essential to our methodology to have test models that are distinct in nature and subjected to different energy supply protocols. This is because, like equilibrium thermodynamics, we expect nonequilibrium thermodynamic potentials to be "general".

This thesis is structured as follows. In this chapter, we will introduce certain aspects of nonequilibrium physics. The introduction roughly follows the three phases described above. Along the way, we will include theoretical backgrounds needed for this thesis. Due to the vastness of nonequilibrium physics and limited by the author's knowledge, the author by no means claims to be thorough. Rather, the author selectively gives information and derivations in an effort to trace important results in each phase. We will also take advantage of the giants of this field (historical and current) and present the work as easily as the author possibly can. Our goal in this chapter, after all, is understanding.

From Chapter 2 onwards, our goal is to explore. In Chapter 2, we will introduce and examine the first hypothesis. It concerns the ratio of the energy storage to the total heat flow, and the ratio is hypothesized to be minimum in NESS. We will also study energy storage, in particular, how it is influenced by the details of the energy supply method. The second hypothesis is introduced and studied in Chapter 3. The central quantity is termed the *embedded energy*. In Chapter 4, the *movable wall model* is defined and evaluated. This model exhibits a continuous nonequilibrium phase transition and is particularly helpful for testing nonequilibrium hypotheses. The final hypothesis is introduced and studied in Chapter 5. The central quantity is a Helmholtz-like nonequilibrium potential. A brief summary is given in Chapter 6.

1.1 Equilibrium Thermodynamics

In this section, we review the basics of equilibrium thermodynamics. Following Callen's approach in [47], the subject is introduced through a set of postulates. These postulates orginate *inductively* from the observations (experiments). In the case of thermodynamics, as stated in the overview, the postulates are justified under statistical mechanics.

We shall start with a summary of the postulates. And from these postulates, thermodynamic parameters are defined, and central thermodynamic relations are derived. Next, using the Legendre transform, these relations are generalised to systems defined by different external constraints. Lastly, we introduce the basic assumptions and important equations of equilibrium statistical mechanics.

1.1.1 Postulational Formulation

Fundamental Postulates

For simplicity, we restrict ourselves to consider only *simple systems*. These systems are static, homogeneous, and isotropic; under no external electromagnetic field or gravitational field; contain no chemical reactions. For such systems, the foundational postulates are summarised as follows [47, 48].

Postulate I establishes the existence of equilibrium states, defined as states that can be completely characterised by a list of extensive parameters: the internal energy U, volume V, and number of particles N. In the following, these extensive parameters will be collected denoted as $\{X_a\}$.

Postulate II asserts the existence of entropy and the maximum entropy principle. Entropy S, as defined here, is a quantity that exists for all equilibrium states. Furthermore, it is a function of the extensive parameters $S = S(\{X_a\})$. This function, $S = S(\{X_a\})$, is called the fundamental relation, as it contains all the thermodynamic information of the system. In addition, the maximum entropy principle states that the entropy of the system free of constraints is maximized with respect to all possible constraints.

Postulate III and *Postulate IV* define the properties of S. First, entropy is additive. For a system composed of subsystems $i = 1, 2, \cdots$, each characterised by a set of parameters $\{X_a^i\}$, the entropy of the whole system is the sum of the entropy of each subsystem

$$S(\{X_a\}) = \sum_i S(\{X_a^i\}). \tag{1.1}$$

Second, entropy is continuous and differentiable; it increases monotonically with respect to U. This property allows us to write the fundamental relation with respect to energy, $U = U(\{X_a\})$ with $X_0 = S$. This form is referred to as the *energy representation* of fundamental relation, and the fundamental relation (written using S) is also called the *entropy representation* of fundamental relation. Third, entropy is set to zero at $(\partial U/\partial S)_{V,N} = 0$.

Since temperature is defined as $T \equiv \partial U/\partial S$, this postulation reflects the third law of thermodynamics, which states that the entropy is zero at absolute zero temperature.

Thermodynamic Relations

The differential form and the integral form of the fundamental relation (both energy and entropy representation) are quite useful [48]. Starting with the entropy representation $S = S(\{X_a\})$, the differential form is given by

$$\mathrm{d}S(\{X_a\}) = \sum_a \frac{\partial S}{\partial X_a}\mathrm{d}X_a = \sum_a F_a \mathrm{d}X_a, \qquad F_a \equiv \left(\frac{\partial S}{\partial X_a}\right)_{\{X_b\}_{b\neq a}}, \tag{1.2}$$

where F_a is the entropic intensive parameter conjugate to X_a. The function $F_a = F_a(\{X_b\})$ is called the *equation of state*. Similarly, a differential form can be written for the energy representation

$$\mathrm{d}U(\{X_a\}) = \sum_a \frac{\partial U}{\partial X_a}\mathrm{d}X_a = \sum_a \mathcal{P}_a \mathrm{d}X_a, \qquad \mathcal{P}_a \equiv \left(\frac{\partial U}{\partial X_a}\right)_{\{X_b\}_{b\neq a}}, \tag{1.3}$$

where $\mathcal{P}_a$ is the energetic intensive parameter conjugate to X_a. The integral forms of the fundamental relations are obtained from Euler's homogeneous function theorem. This theorem states that a homogeneous function of degree one satisfies $f(\{cX_i\}) = cf(\{X_i\})$ where c is a constant. The fundamental relations are indeed such homogeneous functions since they are extensive. Using this theorem, the *Euler relations* are obtained

$$S = \sum_a F_a X_a, \tag{1.4}$$

$$U = \sum_a \mathcal{P}_a X_a. \tag{1.5}$$

Immediately, by taking the total differentials of Eqs. (1.4) and (1.5), and subtract Eqs. (1.2) and (1.3), we obtain the Gibbs-Duhem relations

$$\sum_a X_a \mathrm{d}F_a = 0, \tag{1.6}$$

$$\sum_a X_a \mathrm{d}\mathcal{P}_a = 0. \tag{1.7}$$

Another class of useful relations is the Maxwell relations. These are relations between the mixed second order derivatives of the fundamental relations; they arise from the symmetry of mixed derivatives

$$\frac{\partial^2 S}{\partial X_a X_b} = \frac{\partial^2 S}{\partial X_b X_a} \quad \text{and} \quad \frac{\partial^2 U}{\partial X_a X_b} = \frac{\partial^2 U}{\partial X_b X_a}. \tag{1.8}$$

Using the intensive parameters, these relations are written as

$$\frac{\partial F_a}{\partial X_b} = \frac{\partial F_b}{\partial X_a} \quad \text{and} \quad \frac{\partial \mathcal{P}_a}{\partial X_b} = \frac{\partial \mathcal{P}_b}{\partial X_a}. \tag{1.9}$$

As an example, consider a simple system characterised by fixed U, V and N, $\{X_a\} = \{U, V, N\}$. The differential forms are explicitly

$$\mathrm{d}S(U,V,N) = \frac{1}{T}\mathrm{d}U + \frac{P}{T}\mathrm{d}V - \frac{\mu}{T}\mathrm{d}N, \tag{1.10}$$

$$\mathrm{d}U(S,V,N) = T\mathrm{d}S - P\mathrm{d}V + \mu\mathrm{d}N, \tag{1.11}$$

where T is the temperature, P is the pressure, and μ is the chemical potential. And the integral forms are

$$S = \frac{1}{T}U + \frac{P}{T}V - \frac{\mu}{T}N, \tag{1.12}$$

$$U = TS - PV + \mu N. \tag{1.13}$$

The entropic and energetic intensive parameters are

$$\begin{aligned} F_U &= \frac{1}{T}, \qquad F_V = \frac{P}{T}, \qquad F_N = -\frac{\mu}{T}, \\ \mathcal{P}_S &= T, \qquad \mathcal{P}_V = -P, \qquad \mathcal{P}_N = \mu, \end{aligned} \tag{1.14}$$

respectively.

First Law of Thermodynamic

The first law of thermodynamics introduces two important quantities: work W and heat Q. The first law of thermodynamic can be formulated as

$$đW_{in} = \mathrm{d}U + đQ_{diss}, \tag{1.15}$$

that is, the work input into the system either changes the system energy or dissipates as heat.

These two quantities are not thermodynamic parameters – they depend on specific processes rather than thermodynamic states. This fact is also reflected in the symbol $đ$, which denotes inexact differentials. However, they can be linked to thermodynamic parameters for certain processes. Consider a closed system under a quasi-static compression process. The work input is identified as

$$đW_{in} = -P\mathrm{d}V. \tag{1.16}$$

Then, the dissipated heat is given by $đQ_{diss} = đW_{in} - \mathrm{d}U$. Since the system does not exchange particles with the environment, that is, $\mathrm{d}N = 0$, the differential form (1.11) becomes $\mathrm{d}U = T\mathrm{d}S - P\mathrm{d}V$. Therefore,

$$đQ_{diss} = -T\mathrm{d}S. \tag{1.17}$$

1.1.2 Legendre Transform and Thermodynamic Potentials

Using the Legendre transform, the fundamental relations can be equivalently written in several other forms [47]. These various forms are the thermodynamic potentials. Since no information is lost during a Legendre transform, these forms are equivalent, and each contains the full thermodynamic information of the system [49].

The definition of the Legendre transform is as follows [49]. Consider a function $f(x)$ that is strictly convex (or strictly concave, in which case we shall take $-f(x)$), the Legendre transform of $f(x)$ produces a new function $g(s)$ where

$$g(s) = sx(s) - f(s) \tag{1.18}$$

with

$$s(x) \equiv \frac{\mathrm{d}f(x)}{\mathrm{d}x}. \tag{1.19}$$

We remark that the new function is a function of the new variable s, *i.e.*, both x and $f(x)$ needs to be rewritten with respect to s. Specifically, $x(s)$ is obtained from the inverse of Eq. (1.19), and $f(s)$ from $f(x(s))$. It is easy to show that the Legendre transform of $g(s)$ is $f(x)$, *i.e.*,

$$f(x) = s(x)x - g(x), \qquad x(s) \equiv \frac{\mathrm{d}g(s)}{\mathrm{d}s}. \tag{1.20}$$

As we can see, the Legendre transform and the original function has a symmetric form,

$$g(s) + f(x) = sx, \tag{1.21}$$

where

$$\frac{\mathrm{d}g(s)}{\mathrm{d}s} = x \text{ and } \frac{\mathrm{d}f(x)}{\mathrm{d}x} = s, \tag{1.22}$$

with $g(s)$ and $f(x)$ encoding the same amount of information.

In equilibrium thermodynamics, the fundamental relations are multivariate functions of $\{X_a\}$. Their Legendre transforms can be performed with respect to one or several variables. To simplify the notation, we will separate the transformed variables from the untransformed ones by denoting the former with Greek subscripts "$-_\alpha$"; further, the transformed function with respect to x_α is denoted as $f[s_\alpha]$ where $s_\alpha \equiv \partial f/\partial x_\alpha$ (similar to Eq. (1.19)). When f is the thermodynamic fundamental relations, s_α becomes the entropic or energetic intensive parameter (see Eqs. (1.2) and (1.3)). In the end, a general Legendre transform of the entropic and energetic fundamental relation is written as

$$S[F_\alpha, \cdots] = \sum_\alpha F_\alpha X_\alpha - S(X_i, \cdots; F_\alpha, \cdots), \tag{1.23}$$

$$U[\mathcal{P}_\alpha, \cdots] = \sum_\alpha \mathcal{P}_\alpha X_\alpha - U(X_i, \cdots; P_\alpha, \cdots). \tag{1.24}$$

The familiar thermodynamic potentials can be identified as the (negative) Legendre transform of the energetic fundamental relation

$$\begin{aligned} F(T,V,N) &\equiv -U[T] = U - TS, \\ H(S,P,N) &\equiv -U[P] = U + PV, \\ G(T,P,N) &\equiv -U[T,P] = U - TS + PV, \\ J(T,V,\mu) &\equiv -U[T,\mu] = U - TS - \mu N. \end{aligned} \tag{1.25}$$

The minus signs before the transformations are due to convention. These potentials are the Helmholtz free energy F, the enthalpy H, the Gibbs free energy G, and the grand canonical potential J, respectively. The Legendre transforms of the entropy representation, on the other hand, are the generalised Massieu-Planck potentials [47].

Since the (entropic) fundamental relation is accompanied with the maximum entropy principle, each of the above potentials has a corresponding variational principle; and due to the negative sign, these variational principles are minimum principles. Each potential is further accompanied with a differential form, an integral form, and Maxwell relations. Specifically, the differential forms are

$$\begin{aligned} \mathrm{d}F(T,V,N) &= -S\mathrm{d}T - P\mathrm{d}V + \mu\mathrm{d}N, \\ \mathrm{d}H(S,P,N) &= T\mathrm{d}S + V\mathrm{d}P + \mu\mathrm{d}N, \\ \mathrm{d}G(T,p,N) &= -S\mathrm{d}T + V\mathrm{d}P + \mu\mathrm{d}N, \\ \mathrm{d}J(T,V,\mu) &= -S\mathrm{d}T - P\mathrm{d}V - N\mathrm{d}\mu, \end{aligned} \tag{1.26}$$

and the integral forms are

$$\begin{aligned} F &= -PV + \mu N, \\ H &= TS + \mu N, \\ G &= \mu N, \\ J &= -PV, \end{aligned} \tag{1.27}$$

respectively.

1.1.3 Equilibrium Statistical Mechanics

Equilibrium statistical mechanics is founded on two postulations, the *principle of equal probability* and the *Boltzmann principle* [50, 51]. The principle of equal probability states that, for an isolated system with energy within the interval E and $E + \delta E$ (where δE is the uncertainty), all quantum states (microstates) compatible with the energy interval are equally probable. Suppose that the number of quantum states within $(E, E + \delta E)$ is Ω, then the probability of the system in (any) state i is

$$p_i = \frac{1}{\Omega}. \tag{1.28}$$

This probability distribution is referred to as the microcanonical distribution. The Boltzmann principle, on the other hand, identifies entropy as a (logarithmic) measure of the number of states compatible with the external constraints,

$$S_B = k_\mathrm{B} \ln \Omega, \tag{1.29}$$

where k_B is the Boltzmann constant. This principle provides a crucial link between thermodynamics and statistical mechanics.

In reality, however, isolated systems are rare: almost all systems have some form of energy or matter exchange with the environment. The probability distribution of the microstates p_i of these systems can be derived from the principle of equal probability. This probability distribution is the basis from which all relevant quantities, such as macroscopic and mesoscopic observables, and fluctuations, are obtained. On the other hand, the entropy of a general system described by p_i is given by Gibbs [15]

$$S_G = -k_B \sum_i p_i \ln p_i. \tag{1.30}$$

An equivalence of the Gibbs entropy (1.30) and the Boltzmann entropy (1.29) can be seen by taking $p_i = 1/\Omega$ in Eq. (1.30).

As an example, consider a closed system in contact with a heat bath of temperature T. It can be shown that the probability of the system in microstate i, with energy between E_i and $E_i + \delta E_i$, is given by [51]

$$p_i = \frac{e^{-\beta E_i}}{\mathcal{Z}}, \qquad \mathcal{Z} \equiv \sum_i \exp(-\beta E_i), \tag{1.31}$$

where $\beta = 1/(k_B T)$ is the inverse temperature and $\mathcal{Z}$ the partition function. Using the probability distribution, the ensemble average of a macroscopic quantity O is given by

$$\langle O \rangle_{eq} = \sum_i p_i O_i. \tag{1.32}$$

In particular, the Helmholtz free energy is identified as

$$F \equiv -k_{\mathrm{B}} T \ln \mathcal{Z}. \tag{1.33}$$

The thermodynamic quantities calculated using Eq. (1.32) satisfy the thermodynamic relations described previously. Therefore, we say that equilibrium thermodynamics is justified by statistical mechanics.

1.2 Non-equilibrium Thermodynamics

In this section, we selectively introduce some results from phase two – the early nonequilibrium physics. We will start with nonequilibrium thermodynamics, where the expression of the entropy production rate is derived, and it's simplified form in the linear regime is given. Next, we review the minimum entropy production principle (MinEP). A brief derivation of MinEP for a simple system with heat conduction is given here. Lastly, we deal with nonequilibrium statistical mechanics. Using a simple model of Brownian motion, the Langevin equation and the Fokker-Planck equation are introduced.

1.2.1 Linear Irreversible Thermodynamics

The *local equilibrium assumption* is a central assumption of nonequilibrium thermodynamics. As a first step towards nonequilibrium, this assumption allows us to generalise equilibrium thermodynamic quantities into the nonequilibrium regime [5, 16, 21, 48, 52].

The local equilibrium assumption can be separated into two parts. First, it assumes a separation of timescales. In nonequilibrium processes, the macroscopic variables are assumed to evolve at a timescale much larger than that of microscopic interactions. Second, it assumes a separation of spatial scales. It assumes that a macroscopic system can be divided into smaller systems – each still large enough to be described thermodynamically. As a result, the thermodynamic extensive variables $\{X_a\}$ are extended to the local (and instantaneous) densities $\{x_a(\vec{r},t)\}$ with

$$X_a(t) = \int_V x_a(\vec{r},t)\mathrm{d}r^3, \tag{1.34}$$

where $\vec{r}$ is position and t is time. Since volume V has no local counterpart, it is removed from the collection of $\{x_a(\vec{r},t)\}$.

In particular, entropy is generalised to local entropy density; the fundamental relation is hence expressed as $s(\vec{r},t) = s(\{x_\alpha(\vec{r},t)\})$. The differential form (1.2) now holds locally,

$$\mathrm{d}s(\{x_a(\vec{r},t)\}) = \sum_a{}' F_a(\vec{r},t)\mathrm{d}x_a(\vec{r},t), \tag{1.35}$$

where the local intensive parameter conjugate to $x_a(\vec{r},t)$ is given by

$$F_a(\vec{r},t) \equiv \frac{\partial s(\vec{r},t)}{\partial x_a(\vec{r},t)}. \tag{1.36}$$

Balance Equation

Before going into the derivation of the entropy production rate, it is useful to introduce the local balance equation. For a continuous system, the global balance equation of any (scalar) extensive thermodynamics quantity $A(t)$ is given by [21]

$$\frac{\mathrm{d}A(t)}{\mathrm{d}t} + \oint_S \vec{J}_A(\vec{r},t)\mathrm{d}\vec{S} = \int_V \sigma_A(\vec{r},t)\mathrm{d}\vec{r}, \tag{1.37}$$

where $\vec{J}_A$ is the flux (or current) density of A; σ_A is the source (or sink) density from which $A(t)$ is created (or destroyed); V is the volume of the system with the boundary surface S. The unit surface area $\mathrm{d}\vec{S}$ is positive pointing to the outside of the system. Using the local density $a(\vec{r},t)$ of $A(t)$, the local balance equation reads

$$\frac{\partial a(\vec{r},t)}{\partial t} + \nabla \cdot \vec{J}_A(\vec{r},t) = \sigma_A(\vec{r},t). \tag{1.38}$$

For systems in steady states and for conserved quantities, $\partial_t a = 0$. Eq. (1.38) then takes the form of the continuity equation

$$\nabla \cdot \vec{J}_A(\vec{r},t) = \sigma_A(\vec{r},t). \tag{1.39}$$

Entropy Production Rate

From the second law of thermodynamics, nonequilibrium processes are characterised by a non-zero entropy production rate. In nonequilibrium thermodynamics, the entropy production rate σ_s is given by

$$\sigma_s(\vec{r},t) = \sum_a \vec{\mathcal{F}}_a(t,\vec{r})\vec{J}_a(t,\vec{r}), \tag{1.40}$$

where

$$\vec{\mathcal{F}}_a(t,\vec{r}) = \nabla F_a(\vec{r},t) \text{ and } \vec{J}_a(t,\vec{r}) = \frac{\partial}{\partial t}\nabla a(\vec{r},t). \tag{1.41}$$

$\vec{\mathcal{F}}_a(t,\vec{r})$ is termed *affinity* or *generalised force* and is conjugate to the local flux density $\vec{J}_a(t,\vec{r})$. The affinities are often interpreted as the cause of the nonequilibrium processes, whereas the local flux densities as the effect.

Since the entropy production rate is of central importance for nonequilibrium thermodynamics, a short derivation is given here. From the local balance equation (1.38), we have

$$\frac{\partial s(\vec{r},t)}{\partial t} + \nabla \cdot \vec{J}_s(\vec{r},t) = \sigma_s(\vec{r},t). \tag{1.42}$$

The source σ_s is termed the entropy production rate. The first term $\partial s/\partial t$ can be obtained from Eq. (1.35):

$$\frac{\partial}{\partial t}s(\vec{r},t) = \frac{\partial}{\partial t}s(\{x_a(\vec{r},t)\}) = \frac{\partial s(\{x_a(\vec{r},t)\})}{\partial x_a}\frac{\partial x_a}{\partial t} = \sum_a F_a(\vec{r},t)\frac{\partial x_a}{\partial t}. \tag{1.43}$$

According to the definition of flux density (1.41), the entropy flux density is given by

$$\begin{aligned}\vec{J}_s &= \frac{\partial}{\partial t}\nabla s(\{x_a(\vec{r},t)\}) = \frac{\partial}{\partial t}\sum_a \frac{\partial s(\{x_a\})}{\partial x_a}\nabla x_a(\vec{r},t) \\ &= \sum_a \frac{\partial s(\{x_a\})}{\partial x_a}\frac{\partial}{\partial t}\nabla x_a(\vec{r},t) = \sum_a F_a \vec{J}_a.\end{aligned} \tag{1.44}$$

Bringing Eqs. (1.43) and (1.44) into (1.42), the entropy production rate is linked with the thermodynamically defined fluxes and affinities,

$$\begin{aligned}\sigma_s &= \sum_a \left(F_a(\vec{r},t)\frac{\partial x_a}{\partial t} + \nabla \cdot F_a \vec{J}_a \right) \\ &= \sum_a \left(F_a(\vec{r},t)\frac{\partial x_a}{\partial t} + \nabla F_a \cdot \vec{J}_a + F_a \nabla \cdot \vec{J}_a \right) \\ &= \sum_a \left(\nabla F_a \cdot \vec{J}_a + F_a(\nabla \cdot \vec{J}_a + \frac{\partial x_a}{\partial t}) \right).\end{aligned} \tag{1.45}$$

Since all extensive parameters X_a are conserved quantities, there is no source or sink, *i.e.*, $\sigma_a = 0$. Then, according to Eq. (1.38), the term $\nabla \cdot \vec{J}_a + \partial_t x_a$ in Eq. (1.45) is zero. Therefore, Eq. (1.45) becomes

$$\sigma_s(t,\vec{r}) = \sum_a \nabla F_a \cdot \vec{J}_a = \sum_a \vec{\mathcal{F}}_a(t,\vec{r})\vec{J}_a(t,\vec{r}), \tag{1.46}$$

and we have retrieved Eq. (1.40).

Linear Forms

For near-equilibrium processes, the flux density can be further simplified. First, assuming that the system has no memories, in other words, Markovian, then the flux density depends only on instantaneous quantities. Further assuming that $\vec{J}_a$ is a function of affinities $\{\vec{\mathcal{F}}_a\}$, then it can be written using the Taylor expansion around equilibrium

$$\vec{J}_a(\{\vec{\mathcal{F}}_b(\vec{r},t)\}) = \vec{J}_a^{eq} + \sum_b L_{ab}\vec{\mathcal{F}}_b + \frac{1}{2!}\sum_{bc} L_{abc}\vec{\mathcal{F}}_b\vec{\mathcal{F}}_c + \cdots. \tag{1.47}$$

In equilibrium, there are no fluxes, and $\vec{J}_a^{eq} = 0$. Next, since the system is not far away from equilibrium, the affinities are assumed to be small. Then, the expansion can be truncated at second order, leaving only the linear term

$$\vec{J}_a(\{\vec{\mathcal{F}}_b(\vec{r},t)\}) = \sum_b L_{ab}\vec{\mathcal{F}}_b. \tag{1.48}$$

The tensor components L_{ab} are further simplified using Curie's symmetry principle [53] and the Onsager reciprocal relations [18, 19]. Curie's principle states that, "the symmetries of the causes are to be found in the effects". This principle decouples flux densities and affinities of different ranks. The Onsager reciprocal relations gives

$$L_{ab} = \epsilon_a \epsilon_b L_{ba} \tag{1.49}$$

where $\epsilon_a = \pm 1$ is the parity of x_a. These two principles reduce the degree of freedom of tensor $\mathbb{L}$. Finally, the values of tensor components L_{ab} are obtained from phenomenological laws, like Fourier's law for heat conduction and Fick's law for particle diffusion.

As an example, let us consider a simple system under heat conduction [21]. In the linear regime, the energy flux density is (from Eq. (1.48))

$$\vec{J}_E = L_{EE} \vec{\mathcal{F}}_E = L_{EE} \nabla F_E = L_{EE} \nabla \frac{1}{T}. \tag{1.50}$$

Phenomenologically, Fourier's law links the local energy flux linearly to the local temperature gradient,

$$\vec{J}_E = -k \nabla T. \tag{1.51}$$

where k is the thermal conductivity and is measured experimentally. Comparing with Eq. (1.50), the component L_{EE} is identified with $L_{EE} = kT_{av}^2$, where T_{av} is the averaged temperature used here as an approximate of the system temperature.

1.2.2 Minimum Entropy Production

Similar to equilibrium thermodynamics, various efforts have been made in search of variational principles for nonequilibrium thermodynamics. One important example is the minimum entropy production principle (MinEP). Here, we review a short derivation of MinEP. This derivation can be found in [5, 16, 54]. We will be using variational calculus and the Lagrangian multipliers for this derivation. An introduction of these techniques can be found in [55].

Consider the previous example again: a simple system is driven to nonequilibrium states under heat conduction. To be more specific, a one-dimensional heat conducting rod is placed at $x = 0, L$; both ends are heated to a fixed temperature, $T(0) = T_A$ and $T(L) = T_B$. The local entropy production rate is given by [54]

$$\sigma_s(t, x) = J_E \mathcal{F}_E = L_{EE}^{-1} J_E^2, \tag{1.52}$$

where it is written as a function of J_E. The total entropy production rate is then

$$\dot{S}_{tot}[J_E] = \int_0^L \sigma_s \mathrm{d}x = \int_0^L L_{EE}^{-1} J_E^2 \mathrm{d}x. \tag{1.53}$$

Now, we proceed to obtain the heat current function J_E that minimizes the total entropy production rate. The system is under the constraint

$$-\int_0^L \frac{J_E}{k}\mathrm{d}x = T_B - T_A \quad \text{or} \quad \int_0^L \frac{J_E}{k}\mathrm{d}x + (T_B - T_A) = 0, \tag{1.54}$$

where we have used Eq. (1.51). The minimization is obtained using variational calculus, and the constraint is added using the Lagrangian multiplier. This is equivalent to

$$\begin{gathered} \frac{\delta}{\delta J_E}\left(\dot{S}_{tot} - \lambda\left(\int_0^L \frac{J_E}{k}dx + T_B - T_A\right)\right) = 0, \\ \frac{\delta}{\delta J_E}\int_V L_{EE}^{-1}J_E^2 dV - \lambda\frac{\delta}{\delta J_E}\int_0^L \frac{J_E}{k}dx = 0. \end{gathered} \tag{1.55}$$

Performing functional derivative, we obtain

$$\int_0^L \left(2L_{EE}^{-1}J_E - \lambda\frac{1}{k}\right)dx = 0, \tag{1.56}$$

which is satisfied if the solution is $J_E^* = \lambda T_{av}^2/2$. To obtain λ, we substitute J_E^* into Eq. (1.54), and $\lambda = (T_A - T_B)2k/(T_{av}^2 L)$. Finally,

$$J_E^* = \frac{k}{L}(T_A - T_B), \tag{1.57}$$

which coincides with the steady state heat flux. Moreover, since the entropy production rate is always larger than zero, the extremum is a minimum.

1.2.3 Nonequilibrium Statistical Mechanics

For nonequilibrium statistical mechanics, the principle of equal probability no longer applies. The central idea of nonequilibrium statistical mechanics lies in treating the physical processes as stochastic processes. Consequently, the mathematical framework of stochastic dynamics is readily borrowed. Two important methods are the Langevin equation approach and the Fokker-Planck equation approach [25]. Here we provide the basic idea behind these techniques using the paradigm model – Brownian motion [56].

Brownian motion is the random movement of a colloidal particle in a solution. Consider the simplest case of a one-dimensional Brownian motion. The Langevin equation of the particle is given by [22, 25, 48, 52]

$$m\frac{\mathrm{d}v(t)}{\mathrm{d}t} = -\gamma v(t) + F_L(t), \tag{1.58}$$

$$\frac{\mathrm{d}x(t)}{\mathrm{d}t} = v(t), \tag{1.59}$$

where m is the mass of the particle, γ is the friction coefficient, and $\gamma v(t)$ is the friction force at time t. The term $F_L(t)$ is the random force due to microscopic collisions, satisfying

$$\langle F_L(t)\rangle = 0 \quad \text{and} \quad \langle F_L(t_i)F_L(t_j)\rangle = 2Bm^2, \tag{1.60}$$

where B is a constant that measures the strength of fluctuations. The Langevin description is similar to the Newtonian equation with an additional stochastic term. The Langevin equation is an example of the stochastic differential equation.

By integrating Eq. (1.58) and take the average, we have

$$\langle v(t)\rangle = e^{-t\gamma/m}\langle v(0)\rangle. \tag{1.61}$$

Similarly, the standard deviation is obtained,

$$\langle \delta v^2(t)\rangle = \langle (v(t) - \langle v(t)\rangle)^2\rangle = \frac{B}{m\gamma}(1 - e^{-2\gamma t/m}). \tag{1.62}$$

At the large time limit,

$$\lim_{t\to\infty}\langle v(t)\rangle = 0 \;\text{ and }\; \lim_{t\to\infty}\langle \delta v^2(t)\rangle = \frac{B}{m\gamma}. \tag{1.63}$$

On the other hand, the system reaches the equilibrium state at an infinite time. And the energy of the Brownian particle in equilibrium is given by the equipartition theorem

$$\frac{1}{2}mv^2 = \frac{1}{2}k_BT. \tag{1.64}$$

Combining with Eq. (1.63), we obtain

$$B = k_BT\gamma. \tag{1.65}$$

This relation is an example of the fluctuation-dissipation theorem, where the strength of fluctuations B is linked with the dissipation characterised by friction γ.

In the over-damped case, the Langevin equation (1.58) becomes

$$\gamma\frac{\mathrm{d}x}{\mathrm{d}t} = F_L. \tag{1.66}$$

By solving this differential equation and taking averages, we obtain a simpler form

$$\langle x(t)\rangle = 0 \;\text{ and }\; \langle \delta x^2(t)\rangle = \langle x(t)^2\rangle = \frac{2B}{\gamma^2}t. \tag{1.67}$$

On the other hand, the mean square movement (of one-dimension) is given by

$$\langle \delta x^2(t)\rangle = 2Dt, \tag{1.68}$$

where D is the diffusion constant. Combining with Eqs. (1.67) and (1.65), we obtain $D = k_B T/\gamma$, the Einstein-Smoluchowski relation [57–59].

The Fokker-Planck approach describes the evolution of the probability distribution. This approach assumes that the stochastic process is Markovian. And the probability distribution of a Markov process satisfies

$$p(x, t+\tau) = \int_{-\infty}^{\infty} p(x, t+\tau|x', t) p(x', t) \mathrm{d}x', \tag{1.69}$$

where $p(x,t)$ is the probability of finding the particle at x at time t; $p(x,t|x',t')$ is the conditional probability of measuring $p(x,t)$ given that the particle is found at x' at t'. For small time differences, we would expect to find the particle close to its position at t'. In other words, we expect $x - x' = \Delta$ to be small. We rewrite the integrand in Eq. (1.69), by first rewriting x' as $x - \Delta$, and then using the Taylor series to approximate the integrand around x,

$$\begin{aligned} p(x, t+\tau|x', t) p(x', t) &= p(x + \Delta - \Delta, t+\tau|x-\Delta, t) p(x-\Delta, t) \\ &= \sum_{n=0}^{\infty} \frac{(-1)^n \Delta^n}{n!} \frac{\partial^n}{\partial x^n} [p(x+\Delta, t+\tau|x, t) p(x, t)]. \end{aligned} \tag{1.70}$$

The integral is now

$$\begin{aligned} p(x, t+\tau) &= \sum_{n=0}^{\infty} \frac{(-1)^n}{n!} \frac{\partial^n}{\partial x^n} \left(\int_{-\infty}^{\infty} \Delta^n p(x+\Delta, t+\tau|x, t) \mathrm{d}\Delta \right) p(x, t), \\ &= \sum_{n=0}^{\infty} \frac{(-1)^n}{n!} \frac{\partial^n}{\partial x^n} M^{(n)}(x, t+\tau, t) p(x, t), \end{aligned} \tag{1.71}$$

where $M^{(n)}(x, t+\tau, t) = \langle (x(t+\tau) - x(t))^n \rangle$ is the n-th moment of $x(t)$. The Fokker-Planck equation originates from the truncated version of Eq. (1.71) at order 2. Explicitly,

$$p(x, t+\tau) = p(x, t) - \frac{\partial}{\partial x} \left(\mathcal{M}^{(1)} p(t, x) \right) + \frac{1}{2} \frac{\partial^2}{\partial x^2} \left(\mathcal{M}^{(2)} p(t, x) \right), \tag{1.72}$$

with

$$\mathcal{M}^{(1)} = \langle x(t+\tau) - x(t) \rangle \text{ and } \mathcal{M}^{(2)} = \langle (x(t+\tau) - x(t))^2 \rangle. \tag{1.73}$$

For the over-damped Brownian motion, the first and second moment are given by (1.67). Then, Eq. (1.72) becomes

$$p(x, t+\tau) = p(x, t) + Dt \frac{\partial^2}{\partial x^2} p(t, x), \tag{1.74}$$

which is equivalently

$$\frac{\partial p(t, x)}{\partial t} = D \frac{\partial^2}{\partial x^2} p(t, x). \tag{1.75}$$

This equation is exactly Fick's diffusion equation.

1.3 Stochastic Thermodynamics and Much More

The central idea of stochastic thermodynamics is to generalise heat, work, and entropy down to the trajectory level. In this section, we illustrate this idea using the paradigm model – Brownian motion [9, 56].

Consider again a one-dimensional Brownian motion in a heat bath of temperature T. Suppose that, in the general case, the system is under a potential field $V(x)$ and driven by an external force $f(x)$; both of them are under the influence of an external control parameter $\lambda(t)$, giving $f(x,\lambda)$ and $V(x,\lambda)$. The forces are collected to the term $F(x,\lambda) = -\partial_x V(x,\lambda) + f(x,\lambda)$. The trajectory of the particle, measured between $t=0$ and $t=\tau$, is denoted as $[x(t)]$. In the simplest case, we consider a constant control parameter $\lambda(t) = \lambda$, and the over-damped motion. The Langevin equation reads

$$\frac{\mathrm{d}x}{\mathrm{d}t} = \mu F(x,\lambda) + \mu F_L(t), \tag{1.76}$$

where $\mu = 1/\gamma$ is the mobility. The first and second moment are given by

$$\mathcal{M}^{(1)} = \mu F t \quad \text{and} \quad \mathcal{M}^{(2)} = 2Dt. \tag{1.77}$$

Therefore, the Fokker-Planck equation is

$$\partial_t p(x,t) = -\partial_x \Big(\mu F(x,t) p(x,t) - D \partial_x p(x,t) \Big) \equiv -\partial_x j(x,t), \tag{1.78}$$

where $j(x,t)$ is the probability current density.

The first law of thermodynamics (1.15) is generalised to the stochastic level as [9]

$$đw_{in} = \mathrm{d}U + đq_{diss}. \tag{1.79}$$

Each quantity is identified as follows. First, the system energy difference is identified as the change in potential energy

$$\mathrm{d}U = \mathrm{d}V = \frac{\partial V}{\partial \lambda}\mathrm{d}\lambda + \frac{\partial V}{\partial x}\mathrm{d}x. \tag{1.80}$$

Second, the work input is identified from the contribution of λ to the potential, and the external force f applied to the particle along the trajectory, *i.e.,*

$$đw_{in} = \frac{\partial V}{\partial \lambda}\mathrm{d}\lambda + f\mathrm{d}x. \tag{1.81}$$

Hence, the dissipated heat is given by

$$đq_{diss} = đw_{in} - \mathrm{d}U = F\mathrm{d}x. \tag{1.82}$$

This form is consistent with the physical intuition at the macroscopic level, where the heat is the total force over a distance. The work and heat over the trajectory $[x(t)]$ are given by the integration

$$w[x(t)] = \int_0^\tau \left(\frac{\partial V}{\partial \lambda} \dot{\lambda} + f \dot{x} \right) \mathrm{d}t, \tag{1.83}$$

$$q[x(t)] = \int_0^\tau (F\dot{x})\, \mathrm{d}t. \tag{1.84}$$

And the first law over the whole trajectory is

$$w[x(t)] = \Delta U + q[x(t)]. \tag{1.85}$$

The generalisation of entropy starts from the definition of the system entropy on the stochastic level,

$$s(t) \equiv -\ln p(x(t), t), \tag{1.86}$$

where the time dependent $x(t)$ suggests that this is a trajectory specific quantity; $p(x(t), t)$ is the solution to the Fokker-Planck equation (1.78) restricted to $x = x(t)$. Specifically, the initial condition is in accordance with that of the trajectory; after obtaining $p(x, t)$, x is further restricted to the path specific $x(t)$. Taking the time derivative, we have

$$\dot{s}(t) = -\left(\frac{\partial_t p(x,t)}{p(x,t)} + \frac{\partial_x p(x,t)}{p(x,t)} \dot{x} \right)_{x(t)} = \left(\frac{j}{T\mu p} \dot{x} - \frac{\partial_t p}{p} - \frac{F}{T} \dot{x} \right)_{x(t)}. \tag{1.87}$$

The subscript $x(t)$ denotes that the solution is evaluated at this trajectory. Next, the entropy exchanged with the environment is identified as the heat dissipation divided by the heat bath temperature

$$\Delta s_{med}[x(t)] \equiv \frac{q[x(t)]}{T} = \int_0^\tau \frac{F\dot{x}}{T} \mathrm{d}t. \tag{1.88}$$

The last term of Eq. (1.87), therefore, is identified as $\dot{s}_{med}(t)$. Finally, the entropy production rate $\dot{s}_{tot}(t)$ is obtained

$$\dot{s}_{tot}(t) = \dot{s}(t) - \dot{s}_{med}(t) = \left(\frac{j}{T\mu p} \dot{x} - \frac{\partial_t p}{p} \right). \tag{1.89}$$

In stochastic thermodynamics, the entropy production rate is linked with the time-asymmetric part of a trajectory [42]. Using path integrals, the probability of the trajectory with a fixed initial point x_0, $[x(t)|x_0]$, is given by

$$p[x(t)|x_0] = \mathbf{N} \exp[-\mathbf{A}([x(t), \lambda(t)])], \tag{1.90}$$

with the normalisation factor **N** and action **A**

$$\mathbf{A}([x(t), \lambda(t)]) \equiv \frac{1}{4D} \int_0^\tau dt[(\dot{x} - \mu F)^2 + \frac{\mu}{2} \partial_x F]. \tag{1.91}$$

It turns out that the action of the inverse trajectory $\widetilde{x}(t)$ driven by the inverse protocol $\widetilde{\lambda}(t)$ is linked with the action of the forward trajectory,

$$\mathbf{A}([\widetilde{x}(t), \widetilde{\lambda}(t)]) - \mathbf{A}([x(t), \lambda(t)]) = \frac{1}{T} \int_0^{\tau} dt \dot{x} F = \Delta s_{med}[x(t)]. \tag{1.92}$$

In other words,

$$\frac{p[\widetilde{x}(t), \widetilde{\lambda}(t) | \widetilde{x}_0]}{p[x(t), \lambda(t) | x_0]} = e^{-\Delta s_{med}[x(t)]} = e^{-\Delta q[x(t)]/T}, \tag{1.93}$$

the probability of the inverse trajectory (with the initial point $\widetilde{x}_0 = x(\tau)$), relative to the probability of the forward trajectory, is measured by the heat dissipation along the forward trajectory. This equation is an example of the (detailed) fluctuation theorem.

Chapter 2

Storage of Energy in Constrained Systems

2.1 Introduction: Energy Storage and the First Hypothesis

Nonequilibrium systems can store energy in steady states. This energy storage originates from the non-zero heat flow (linked to the entropy production rate) that is ever-present in the nonequilibrium systems [28, 60]. This quantity has become important to the study of nonequilibrium physics. However, energy storage and its interplay with heat flow have been overlooked.

Focusing on nonequilibrium steady states (NESS), we define the energy storage as the energy difference between the system energy in this steady state U and its equilibrium value U_{eq}, $\Delta U \equiv U - U_{eq}$. Additionally, as stated previously, a constant heat flow J_U is present in this steady state. This heat flow is necessary for maintaining the system out of equilibrium. In this chapter, we will study nonequilibrium steady states via the lens of these two quantities.

In this chapter, we will address two issues in particular. First, we study energy storage under various methods of energy supply. These driving methods will be referred to as protocols in the following sections. These protocols are chosen to reflect common physical realizations. From the details of the driving protocols, we obtain the energy in steady states U and the energy input rate $\dot{E}_{in}$, either analytically or numerically. We will show that energy storage depends not only on the amount of energy supply, but also on the details of the protocol.

Second, we propose a hypothesis of variational principle. This is the first hypothesis of the thesis. We define a quantity $\mathcal{T}$ as the ratio of the stored energy to the heat flow,

$$\mathcal{T} \equiv \frac{U - U_{eq}}{J_U}. \tag{2.1}$$

This quantity has a dimension of time. Using the Lennard-Jones simulation (see Sec. 2.2.2), it is shown that $\mathcal{T}$ coincides with the initial characteristic relaxation time for the system to return to equilibrium. In other words, it coincides with the characteristic time at which the system dissipates its stored energy immediately after the removal of the external energy supply. Based on this quantity, we propose the following hypothesis,

Hypothesis 2.1.1. $\mathcal{T}$ is minimized in nonequilibrium steady states.

To test this hypothesis, we use two approaches that are inspired by the method of obtaining equilibrium entropy S. As stated in Section 1.1.1, the maximum entropy principle states that $S \geq S_{\text{constrained}}$, where $S_{\text{constrained}}$ is the entropy of the system under any possible constraints. To obtain equilibrium entropy, practically, one can introduce various constraints into the system and measure $\{S_{\text{constrained}}\}$. The equilibrium entropy S is then the maximum of $\{S_{\text{constrained}}\}$.

Our methodology is as follows. First, let us consider the formulation using constraints. This formulation will be used frequently in this thesis. We introduce various constraints into the system and measure the energy storage ΔU_i and the outgoing heat flow J_{U_i} for each subsystem i. The total energy storage and the total outgoing heat flow are then

$$\Delta U_{tot} = \sum_i U_i - U_{eq}, \tag{2.2}$$

$$J_{tot} = \sum_i J_{U_i}. \tag{2.3}$$

We define $\mathcal{T}$ for the constrained system as

$$\mathcal{T}_{1|2} = \frac{\Delta U_{tot}}{J_{tot}}. \tag{2.4}$$

Using various test models, we compare $\mathcal{T}$ with $\mathcal{T}_{1|2}$. If the hypothesis were true, we expect to find

$$\mathcal{T} \leq \mathcal{T}_{1|2}. \tag{2.5}$$

Alternatively, let us consider a second formulation using systems with competing steady states. For a system that exhibits multiple nonequilibrium steady states, we measure $\mathcal{T}$ for each steady state. If the hypothesis were true, we expect to find the stable steady state the one with the lowest $\mathcal{T}$,

$$\mathcal{T}_{\text{stable state}} \leq \{\mathcal{T}_{\text{steady states}}\}. \tag{2.6}$$

We would like to point out that these two approaches, however, should not be considered as proof. In other words, while a violation of relations (2.5) and (2.6) certainly disproofs the hypothesis, an agreement with these relations does not verify the hypothesis. Nonetheless, each example in support of the hypothesis is relevant, as it can help with finding general arguments supporting the hypothesis. Short of proof, this may be the best scientific method. And in time, as one gains understanding through observations, the hypothesis evolves as well.

To summarize our methodology, for each test model, we first define explicitly the function of the external energy supply. The stored energy and the outgoing heat flow are thus obtained (analytically or numerically). Next, for systems that exhibit competing steady states, we measure and compare $\mathcal{T}$ for all possible steady states. Otherwise, for testing systems in general, the first formulation is used. In which case, an internal constraint, often an adiabatic wall or a diathermal wall, is introduced into the system. The same quantities, energy storage and heat flow, are obtained for each subsystem. Finally, we compare $\mathcal{T}$ of the constrained system with the unconstrained system and discuss the implications.

This chapter is a collection of models used to study energy storage and test Hypothesis 2.1.1. Depending on the nature of the energy delivery method, this chapter is organized as follows: in Sec. 2, we will present test models under various bulk energy supplies; in Sec. 3, models are subjected to an external heat flow or matter flow; in Sec. 4, the energy is delivered periodically and locally. A summary is presented in Sec. 5.

2.2 Systems under Bulk Energy Supply

In this section, we compile models that are subjected to a bulk energy supply. Here, a bulk energy supply refers to situations when the energy is supplied via an external energy source and is applied to every point in the system. The primary test systems are an ideal gas and a Lennard-Jones fluid. In the ideal gas, we analyse five models. And in the Lennard-Jones fluid, we present the results of three models. A list of the models with their corresponding protocols is summarized in Table 2.1.

Ideal Gas		LJ
Adiabatic	Diathermal	Adiabatic
$\sigma_E = \lambda_1$ $\sigma_E = \lambda_2 T(x)$ $\sigma_E = \lambda_3 \rho(x)$	$\sigma_E = \lambda_1$	$\sigma_E = \lambda_1$ $\sigma_E = \lambda_2 T(x)$ $\sigma_E = \lambda_3 \rho(x)$
$\sigma_E = \lambda_1$ with $k = c\sqrt{T}$		

Table 2.1: List of Models. *Adiabatic* and *Diathermal* refer to the type of constraints *adiabatic wall* and *diathermal wall*. σ_E is the energy source density. Without specification, the heat conductivity k is taken to be a constant. For the ideal gas under an adiabatic wall, we also study the case where $k = c\sqrt{T}$.

The author would like to point out that the results of the Lennard-Jones liquid are reproduced from paper [1], where the simulations were performed by Dr. Litniewski. These results are presented here to provide a more holistic view.

2.2.1 Ideal Gas

2.2.1.1 General Analysis

Consider a closed ideal gas model of a fixed number of particles N and volume V, in a heat bath of temperature T_0. The system is driven out-of-equilibrium by a bulk energy delivery. The energy delivery protocols are realised by the local energy source function $\sigma_E(\vec{r})$, where an amount of energy $\sigma_E(\vec{r})$ is delivered at position $\vec{r}$ per unit time. We remark that σ_E has the unit of energy per unit volume and unit time.

In steady states, the local energy does not change in time. Therefore, from local energy conservation (1.39), we have

$$\nabla \cdot \vec{J}_E = -k\nabla^2 T(\vec{r}) = \sigma_E(\vec{r}). \tag{2.7}$$

Here, we have assumed Fourier's law for the local heat flux, as in Eq. (1.51)

$$\vec{J}_E(\vec{r}) = -k\nabla T(\vec{r}), \tag{2.8}$$

where k is the heat conductivity and $T(\vec{r})$ is the local temperature. Unless stated otherwise, we take k as a constant. In kinetic theory, however, the heat conductivity is given by $k \sim \sqrt{T}$, which we will discuss in **case 4**.

We further assume local equilibrium. Under this assumption, we extend the ideal gas law and the equipartition theorem to hold locally in NESS. A discussion of the local equilibrium assumption can be found in Sec. 1.2.1. Finally, we assume that the pressure is constant across the system. Since for the ideal gas, the energy density is proportional to the pressure, the energy density is constant as well. This assumption is based on an observation from the Lennard-Jones simulations of a gas-liquid system [61]. In this paper, the authors found that the mechanical force redistribution process is much faster than the heat flow process. We generalise this idea to an ideal gas in NESS. In other words, we assume the system to have a constant pressure on the timescale that we focus on – the timescale at which we observe heat transfer.

To summarize, for an ideal gas in NESS, we assume that the ideal gas law holds locally

$$P = n(\vec{r})k_B T(\vec{r}), \tag{2.9}$$

where P is the pressure, $n(\vec{r})$ is the local particle density with $\int_V \mathrm{d}^3 r n(\vec{r}) = N$, k_B is the Boltzmann constant which we will take to be unity. From equipartition, the energy density of a three-dimensional monoatomic ideal gas is proportional to the pressure,

$$\epsilon \equiv \frac{U}{V} = \frac{3}{2}n(\vec{r})k_B T(\vec{r}) = \frac{3}{2}P. \tag{2.10}$$

Both P and ϵ are assumed to be constant across the system.

From Eq. (2.10), we obtain the energy density by observing that

$$\epsilon \int_V \frac{\mathrm{d}^3 r}{T(\vec{r})} = \frac{3}{2} k_B \int_V \mathrm{d}^3 r n(\vec{r}) = \frac{3}{2} k_B N = \frac{\epsilon_0}{T_0} V, \tag{2.11}$$

where ϵ_0 is the energy density at equilibrium, and the last equality comes from the equipartition theorem $\epsilon_0 V = 3Nk_B T_0/2$. Therefore, we obtain the following relation between the energy density and the temperature profile

$$\epsilon = \frac{3}{2} N k_B \frac{1}{\displaystyle\int_V \frac{\mathrm{d}^3 r}{T(\vec{r})}} = \frac{\epsilon_0}{T_0} \frac{V}{\displaystyle\int_V \frac{\mathrm{d}^3 r}{T(\vec{r})}}. \tag{2.12}$$

And from ϵ, the energy storage is obtained,

$$\Delta U \equiv U - U_{eq} = (\epsilon - \epsilon_0) V. \tag{2.13}$$

For the models in this section, all energies are supplied through local energy sources. The rate of energy flowing into the system is given by

$$\dot{E}_{in} = \int_V \sigma_E(\vec{r}) \mathrm{d}^3 r. \tag{2.14}$$

In NESS, this rate matches the rate of energy flowing out, $\dot{E}_{in} = \dot{E}_{out}$. On the other hand, the outgoing heat flow rate J_U is defined as

$$J_U \equiv \int_S \vec{J}_E \cdot \hat{n} \mathrm{d}S, \tag{2.15}$$

where S is the surface through which the heat flows out, and $\hat{n}$ is the unit normal vector. Without performing work (as is the case for our systems), all energy flows out in the form of heat. In other words, for systems without performing work, we have

$$\dot{E}_{in} = \dot{E}_{out} = J_U. \tag{2.16}$$

By introducing geometrical constraints, the system is partitioned into multiple subsystems, and the system reaches a new steady state. The constraints are introduced such that, upon removal, the system returns to the original unconstrained steady state. These constraints do not change the local relation of $\vec{J}_E(\vec{r})$ and $T(\vec{r})$. Also, for each subsystem i, the definition of the stored energy U_i remains the same. In the following, we will denote the variables of subsystem i with subscription $-_i$. In general, the subsystem energy density will depend on the constraint. However, in all cases, we will keep the overall number density in each subsystem constant, *i.e.*, $N_i/V_i = N/V = n_0$, where n_0 is the number density at equilibrium. And for each subsystem, we have $\int_{V_i} \mathrm{d}^3 r n_i(\vec{r}) = N_i$.

Thus,

$$\epsilon_i \int_{V_i} \frac{\mathrm{d}^3 r}{T_i(\vec{r})} = \frac{3}{2} k_B N_i = \frac{\epsilon_0}{T_0} V_i. \tag{2.17}$$

As a result, the expression of ϵ_i has the same form as (2.12). Explicitly,

$$\epsilon_i = \frac{3}{2} N_i k_B \frac{1}{\displaystyle\int_{V_i} \frac{\mathrm{d}^3 r}{T_i(\vec{r})}} = \frac{\epsilon_0}{T_0} \frac{V_i}{\displaystyle\int_{V_i} \frac{\mathrm{d}^3 r}{T_i(\vec{r})}}. \tag{2.18}$$

The heat flow of each subsystem J_{U_i}, on the other hand, is obtained from the energy supply (per time) in each subsystem

$$J_{U_i} = \int_{V_i} \sigma_E(\vec{r}) \mathrm{d}^3 r. \tag{2.19}$$

The total energy storage for the constrained system is given by Eq. (2.2),

$$\Delta U_{tot} = \sum_i \epsilon_i V_i - \epsilon_0 V, \tag{2.20}$$

and the total outgoing heat flow is given by Eq. (2.3). For every case studied in this paper, we will compare the ratio $\mathcal{T}_{1|2}$ of the constrained system (2.4) with the ratio $\mathcal{T}$ (2.1).

In the following, we will show the results of five different ideal gas models where, as shown in Table 2.1, four models are under the adiabatic constraints, and one model is under the diathermal constraint.

2.2.1.2 Adiabatic Constraint

case 1. $\sigma_E = \lambda_1$ To further simplify the model, we specify that the ideal gas is three-dimensional, placed between two diathermal walls of area $\mathcal{A}$ ($\mathcal{A} \to \infty$), and that the walls are fixed at $x = \pm L$. The walls will be at temperature T_0. In the simplest case, the energy source is distributed homogeneously over the system with $\sigma_E(\vec{r}) = \lambda_1$. As internal constraints, an adiabatic wall is fixed at $x_1 \in (-L, L)$. This constraint separates the system into two subsystems (denoted as 1 and 2) with volumes $V_1 = \mathcal{A}(L + x_1)$ and $V_2 = \mathcal{A}(L - x_1)$, respectively. A scheme of the system is shown in Fig. 2.1.

Consider first $\mathcal{T}$ of the unconstrained system. As the coordinates y and z do not influence the temperature profile, it is sufficient to consider $x-$dependence. The temperature profile $T(x)$ is obtained by solving Eq. (2.7), which now has the form $-k\partial_x^2 T = \lambda_1$. Using dimensionless variables $\widetilde{\lambda}_1 = \lambda_1 L^2/kT_0$, $\widetilde{T}(x) = T(x)/T_0$ and normalize x to $\widetilde{x} = x/L$, we obtain

$$\widetilde{T}(\widetilde{x}) = -\frac{\widetilde{\lambda}_1}{2}\widetilde{x}^2 + 1 + \frac{\widetilde{\lambda}_1}{2}. \tag{2.21}$$

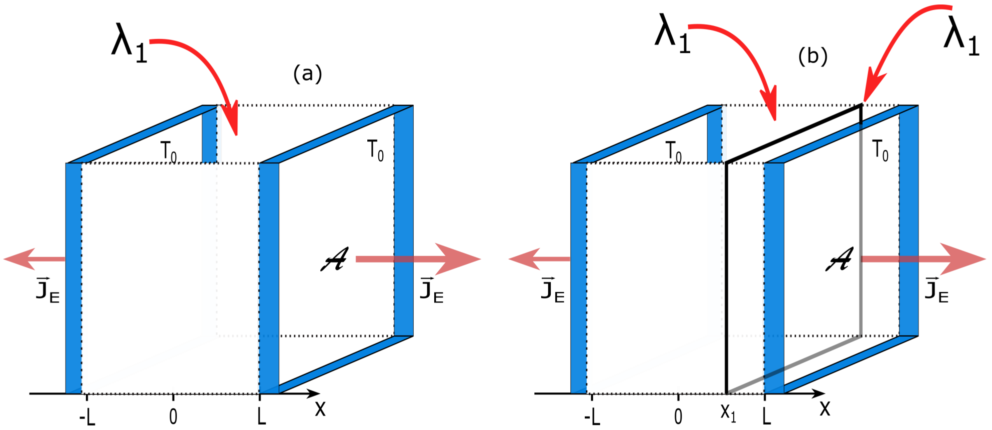

Figure 2.1: Schemes of (a) unconstrained and (b) constrained ideal gas model under an external energy supply. The two diathermal walls of area $\mathcal{A}$ ($\mathcal{A} \to \infty$) and temperature T_0 are positioned at $x = \pm L$. External energy is supplied homogeneously to the bulk with a density λ_1. The heat flux density $\vec{J}_E$ flows out of the system through boundaries. In (b), the vertical plane at $x = x_1$ represents the internal constraint, which is an adiabatic wall.

Using Eq. (2.12), we find the energy density to be

$$\epsilon = \frac{\epsilon_0 \sqrt{\widetilde{\lambda}_1(\widetilde{\lambda}_1 + 2)}}{2\,\mathrm{Arctanh}(\sqrt{\widetilde{\lambda}_1/(\widetilde{\lambda}_1 + 2)})}. \tag{2.22}$$

As stated above, the outgoing heat flow equals the incoming energy flow, $\dot{E}_{in} = 2L\mathcal{A}\lambda = J_U$. Combining with Eq. (2.22), we find

$$\mathcal{T} = \frac{\Delta U}{J_U} = \frac{\epsilon - \epsilon_0}{\lambda_1}. \tag{2.23}$$

In the presence of an adiabatic wall, there are additional boundary conditions at the wall, namely $\partial_x T_i|_{x_1} = 0$ (since there is no heat flux at the constraint). The temperature profile of each subsystem is given by

$$\begin{aligned} \widetilde{T}_1(\widetilde{x}) &= -\frac{\widetilde{\lambda}_1}{2}(\widetilde{x} - \widetilde{x}_1)^2 + \frac{\widetilde{\lambda}_1}{2}(1 + \widetilde{x}_1)^2 + 1, \\ \widetilde{T}_2(\widetilde{x}) &= -\frac{\widetilde{\lambda}_1}{2}(\widetilde{x} - \widetilde{x}_1)^2 + \frac{\widetilde{\lambda}_1}{2}(1 - \widetilde{x}_1)^2 + 1, \end{aligned} \tag{2.24}$$

where $\widetilde{x}_1$ is the rescaled x_1/L. Next, the subsystem energy densities are obtained,

$$\begin{aligned} \epsilon_1 &= \frac{\epsilon_0}{2} \frac{\sqrt{\widetilde{\lambda}_1(1 + \widetilde{x}_1)^2(\widetilde{\lambda}_1(1 + x_1)^2 + 2)}}{\mathrm{Arctanh}\sqrt{\widetilde{\lambda}_1(1 + \widetilde{x}_1)^2/(\widetilde{\lambda}_1(1 + \widetilde{x}_1)^2 + 2)}} = \frac{\epsilon_0}{2} \frac{\sqrt{\Lambda_+(\Lambda_+ + 2)}}{\mathrm{Arctanh}\sqrt{\Lambda_+/(\Lambda_+ + 2)}}, \\ \epsilon_2 &= \frac{\epsilon_0}{2} \frac{\sqrt{\widetilde{\lambda}_1(1 - \widetilde{x}_1)^2(\widetilde{\lambda}_1(1 - \widetilde{x}_1)^2 + 2)}}{\mathrm{Arctanh}\sqrt{\widetilde{\lambda}_1(1 - \widetilde{x}_1)^2/(\widetilde{\lambda}_1(1 - \widetilde{x}_1)^2 + 2)}} = \frac{\epsilon_0}{2} \frac{\sqrt{\Lambda_-(\Lambda_- + 2)}}{\mathrm{Arctanh}\sqrt{\Lambda_-/(\Lambda_- + 2)}}, \end{aligned} \tag{2.25}$$

where $\Lambda_\pm = \tilde{\lambda}_1(1 \pm \tilde{x}_1)^2$. Additionally, the total heat flux is not changed by the constraint, $J_{tot} = J_U = 2L\mathcal{A}\lambda$. Eventually, we obtain

$$\begin{aligned} \mathcal{T}_{1|2} = \frac{\Delta U_{tot}}{J_{tot}} &= \frac{\epsilon_1(1+\tilde{x}_1) + \epsilon_2(1-\tilde{x}_1) - 2\epsilon_0}{2\lambda_1} \\ &= \frac{\epsilon_0}{\lambda_1}\Big(f_1(\tilde{x}_1) + f_2(\tilde{x}_1) - 1\Big), \end{aligned} \tag{2.26}$$

where

$$f_1(\tilde{x}_1) = \frac{(1+\tilde{x}_1)\sqrt{\Lambda_+(\Lambda_+ + 2)}}{4\,\mathrm{Arctanh}\,\sqrt{\Lambda_+/(\Lambda_+ + 2)}}, \tag{2.27}$$

$$f_2(\tilde{x}_1) = \frac{(1-\tilde{x}_1)\sqrt{\Lambda_-(\Lambda_- + 2)}}{4\,\mathrm{Arctanh}\,\sqrt{\Lambda_-/(\Lambda_- + 2)}}. \tag{2.28}$$

Finally, we compare $\mathcal{T}_{1|2}$ with $\mathcal{T}$. This comparison reduces to the comparison between

$$f_1(\tilde{x}_1) + f_2(\tilde{x}_1) \quad \text{and} \quad f_0 = \frac{\sqrt{\tilde{\lambda}_1(\tilde{\lambda}_1 + 2)}}{2\,\mathrm{Arctanh}\,\sqrt{\tilde{\lambda}_1/(\tilde{\lambda}_1 + 2)}}. \tag{2.29}$$

It is easy to verify that, for all values of λ_1, $f_1(\tilde{x}_1)$ and $f_2(\tilde{x}_1)$ lie above their tangent line at $\tilde{x}_1 = 0$, *i.e.*, $f_1(\tilde{x}_1) \geq f_1(0) + f_1'(0)\tilde{x}_1$ and $f_2(\tilde{x}_1) \geq f_2(0) + f_2'(0)\tilde{x}_1$. Noticing that $f_1(0) = f_2(0) = f_0/2$ and $f_1'(0) = -f_2'(0)$, we find $f_1(\tilde{x}_1) + f_2(\tilde{x}_1) \geq f_0$. Hence, we have shown $\mathcal{T} \leq \mathcal{T}_{1|2}$ for all values of λ_1.

An example of the (normalised) temperature profiles and (normalised) energy storage comparison is shown in Fig. 2.2. The comparison of the energy storage is equivalent to the comparison between $\mathcal{T}$, since the total heat flow is the same under constraint.

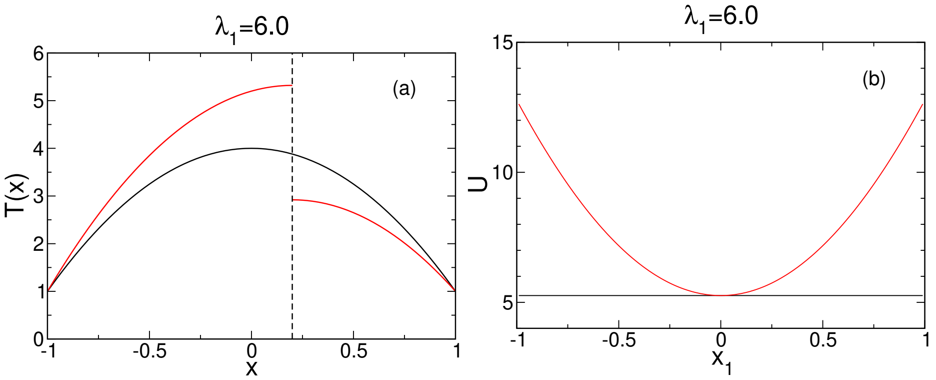

Figure 2.2: Comparison between constrained (in red) and unconstrained system (in black) of **case 1**: ideal gas under a homogeneous energy supply of density λ_1. (a) Comparison of temperature profiles $T(x)$. The vertical dashed line denotes the constraint placed at $x = 0.2$. T measured in units of T_0 and x in L. (b) Total energy U in steady states plotted against various positions of the constraint x_1. U is measured in units of U_{eq} and x_1 in L. As the heat flow does not change under constraint, this is equivalent to comparing $\mathcal{T}$ and $\mathcal{T}_{1|2}$.

case 2. $\sigma_E(\vec{r}) = \lambda_2 T(\vec{r})$ We now consider an energy supply scheme where the local energy source is proportional to the local temperature, $\sigma_E(\vec{r}) = \lambda_2 T(\vec{r})$. Eq. (2.7) is now $-k\partial_x^2 T(x) = \lambda_2 T(x)$, or

$$\frac{d^2T}{dx^2} + \frac{\lambda_2}{k}T(x) = 0. \tag{2.30}$$

The boundary conditions are the same as **case 1**: $T(\pm L) = T_0$. And the temperature profile is,

$$\widetilde{T}(\widetilde{x}) = \frac{\cos\left(\widetilde{x}\sqrt{\widetilde{\lambda}_2}\right)}{\cos\left(\sqrt{\widetilde{\lambda}_2}\right)}, \tag{2.31}$$

where $\widetilde{\lambda}_2 = \lambda_2 L^2/k$ is the dimensionless energy supply rate in this case. Since temperature must be positive, we require that $0 < \sqrt{\widetilde{\lambda}} < \pi/2$. For larger values of $\widetilde{\lambda}$, the solutions are not stable. Similarly, using $\partial_x T|_{x_1} = 0$, the temperature profiles of subsystems are

$$\widetilde{T}_1(\widetilde{x}) = \frac{\cos\left(\sqrt{\widetilde{\lambda}_2}(\widetilde{x} - \widetilde{x}_1)\right)}{\cos\left(\sqrt{\Lambda_+}\right)}, \tag{2.32}$$

$$\widetilde{T}_2(\widetilde{x}) = \frac{\cos\left(\sqrt{\widetilde{\lambda}_2}(\widetilde{x} - \widetilde{x}_1)\right)}{\cos\left(\sqrt{\Lambda_-}\right)}, \tag{2.33}$$

where $\Lambda_\pm = \widetilde{\lambda}_2(1 \pm \widetilde{x}_1)^2$.

From Eq. (2.12), the energy density is obtained,

$$\epsilon = \epsilon_0 \frac{\sqrt{\widetilde{\lambda}_2}}{\cos\left(\sqrt{\widetilde{\lambda}_2}\right) \ln\left(\dfrac{\cos\left(\sqrt{\widetilde{\lambda}_2}/2\right) + \sin\left(\sqrt{\widetilde{\lambda}_2}/2\right)}{\cos\left(\sqrt{\widetilde{\lambda}_2}/2\right) - \sin\left(\sqrt{\widetilde{\lambda}_2}/2\right)}\right)}. \tag{2.34}$$

And for the subsystems under a constraint at $x = x_1$,

$$\epsilon_1 = \epsilon_0 \frac{\sqrt{\Lambda_+}}{\cos\left(\sqrt{\Lambda_+}\right)} \frac{1}{\ln\left(\dfrac{\cos\left(\sqrt{\Lambda_+}/2\right) + \sin\left(\sqrt{\Lambda_+}/2\right)}{\cos\left(\sqrt{\Lambda_+}/2\right) - \sin\left(\sqrt{\Lambda_+}/2\right)}\right)}, \tag{2.35}$$

$$\epsilon_2 = \epsilon_0 \frac{\sqrt{\Lambda_-}}{\cos\left(\sqrt{\Lambda_-}\right)} \frac{1}{\ln\left(\dfrac{\cos\left(\sqrt{\Lambda_-}/2\right) + \sin\left(\sqrt{\Lambda_-}/2\right)}{\cos\left(\sqrt{\Lambda_-}/2\right) - \sin\left(\sqrt{\Lambda_-}/2\right)}\right)}. \tag{2.36}$$

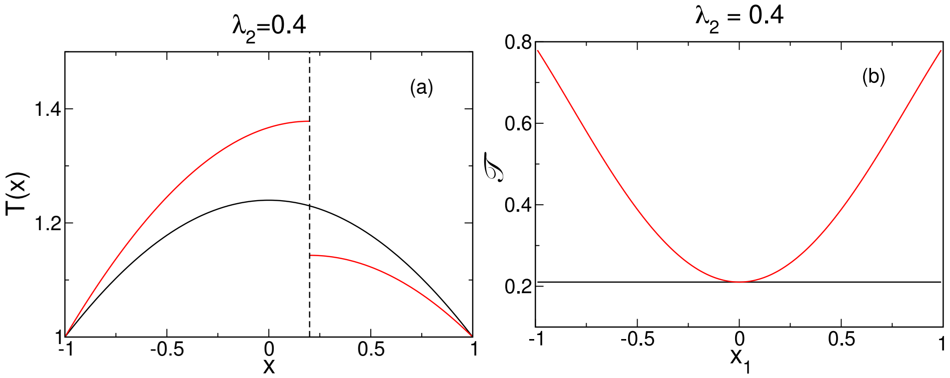

Figure 2.3: Comparison between constrained (red) and unconstrained system (black) of **case 2**: ideal gas under energy supply scheme $\sigma_E(x) = \lambda_2 T(x)$. (a) Comparison between the normalised temperature profiles $T(x)$. The vertical dashed line is the constraint at $x = 0.2$. (b) Comparison between (reduced) $\mathcal{T}$ plotted against constraint position x_1 (in units of L).

In addition, the outgoing heat flow is obtained using Eq. (2.14),

$$J_U = \frac{\mathcal{A}kT_0}{L} \cdot 2\sqrt{\widetilde{\lambda}_2}\,\tan\left(\sqrt{\widetilde{\lambda}_2}\right). \tag{2.37}$$

Similarly, for each subsystem,

$$J_{U_1} = \frac{\mathcal{A}kT_0}{L} \cdot \sqrt{\widetilde{\lambda}_2}\,\tan\left(\sqrt{\Lambda_+}\right), \tag{2.38}$$

$$J_{U_2} = \frac{\mathcal{A}kT_0}{L} \cdot \sqrt{\widetilde{\lambda}_2}\,\tan\left(\sqrt{\Lambda_-}\right), \tag{2.39}$$

and the total heat flow is

$$J_{tot} = \frac{\mathcal{A}kT_0}{L}\sqrt{\widetilde{\lambda}_2}\left(\tan\left(\sqrt{\Lambda_+}\right) + \tan\left(\sqrt{\Lambda_-}\right)\right). \tag{2.40}$$

Eliminating common denominators, the comparison between $\mathcal{T}$ and $\mathcal{T}_{1|2}$ becomes

$$\frac{\widetilde{\epsilon} - 1}{\tan\left(\sqrt{\widetilde{\lambda}_2}\right)} \quad \text{and} \quad \frac{\widetilde{\epsilon}_1(1 + \widetilde{x}_1) + \widetilde{\epsilon}_2(1 - \widetilde{x}_1) - 2}{\tan\left(\sqrt{\Lambda_+}\right) + \tan\left(\sqrt{\Lambda_-}\right)}, \tag{2.41}$$

where $\widetilde{\epsilon} = \epsilon/\epsilon_0$ and $\widetilde{\epsilon}_i = \epsilon_i/\epsilon_0$. And equivalently, between

$$\frac{\tan\left(\sqrt{\Lambda_+}\right) + \tan\left(\sqrt{\Lambda_-}\right)}{\tan\left(\sqrt{\widetilde{\lambda}_2}\right)} \quad \text{and} \quad \frac{\widetilde{\epsilon}_1(1 + \widetilde{x}_1) + \widetilde{\epsilon}_2(1 - \widetilde{x}_1) - 2}{\widetilde{\epsilon} - 1}. \tag{2.42}$$

Due to the complex form of ϵ_i, analytical analysis of this relationship is difficult. Instead, we perform numerical analysis of $\mathcal{T}$ and $\mathcal{T}_{1|2}$ at several λ_2 within the valid range. These results indicate that the inequality $\mathcal{T} \leq \mathcal{T}_{1|2}$ holds. An example of the temperature profiles and $\mathcal{T}$ of **case 2**, with and without constraint, is shown in Fig. 2.3.

case 3. $\sigma_E(\vec{r}) = \lambda_3 n(\vec{r})$ In **case 3**, we consider a local energy input proportional to the local particle number density, $\sigma_E(\vec{r}) = \lambda_3 n(\vec{r})$. In this case, Eq. (2.7) becomes

$$\frac{\mathrm{d}^2 T}{\mathrm{d}x^2} + \frac{\lambda_3}{k} n(x) = 0. \tag{2.43}$$

Using the dimensionless variables described previously and the dimensionless energy supply density $\widetilde{\lambda}_3 \equiv \lambda_3 L^2 n_0 / kT_0$, this becomes

$$\frac{\mathrm{d}^2 \widetilde{T}}{\mathrm{d}\widetilde{x}^2} + \widetilde{\lambda}_3 \widetilde{n}(\widetilde{x}) = 0. \tag{2.44}$$

Since the local particle density is linked to the local temperature through Eq. (2.10), this equation is rewritten as

$$\frac{\mathrm{d}^2 \widetilde{T}}{\mathrm{d}\widetilde{x}^2} + \frac{\widetilde{\lambda}_3 \widetilde{\epsilon}}{\widetilde{T}(\widetilde{x})} = 0. \tag{2.45}$$

In general, differential equations of the form $T''(x) + aT^{-1}(x) = 0$ can be solved as follows [62]. First, upon introducing an extra variable $y = \mathrm{d}\widetilde{T}/\mathrm{d}\widetilde{x}$, the second order differential equation is reduced into a first order one. This reduction is achieved by recognizing that $\mathrm{d}^2\widetilde{T}/\mathrm{d}\widetilde{x}^2 = y\mathrm{d}y/\mathrm{d}\widetilde{T}$, and the original equation becomes

$$y \frac{\mathrm{d}y}{\mathrm{d}\widetilde{T}} = -\frac{\widetilde{\lambda}_3 \widetilde{\epsilon}}{\widetilde{T}}. \tag{2.46}$$

Then, this first order differential equation (with respect to $y(\widetilde{T})$) can be solved as usual. The boundary condition of Eq. (2.46), due to symmetry of the temperature profile at $\widetilde{x} = 0$, is $y(\widetilde{T}(0)) = \mathrm{d}_{\widetilde{x}} T|_{\widetilde{x}=0} = 0$. Therefore,

$$y = \frac{\mathrm{d}\widetilde{T}}{\mathrm{d}\widetilde{x}} = \begin{cases} \sqrt{2\widetilde{\lambda}_3 \widetilde{\epsilon} \ln\left(\widetilde{T}(0)/\widetilde{T}\right)} & \text{if } -1 < \widetilde{x} \leq 0, \\ -\sqrt{2\widetilde{\lambda}_3 \widetilde{\epsilon} \ln\left(\widetilde{T}(0)/\widetilde{T}\right)} & \text{if } 0 < \widetilde{x} < 1. \end{cases} \tag{2.47}$$

Now, the equation is a first order differential equation with respect to $T(x)$. We would like to point out that $\widetilde{T}(0)/\widetilde{T} \geq 1$, and hence that $\ln(\widetilde{T}(0)/\widetilde{T})$ is always non-negative.

Next, we proceed to obtain $\widetilde{T}(\widetilde{x})$. Using separation of variables again, we have

$$\int \frac{\mathrm{d}\widetilde{T}}{\sqrt{\ln(\widetilde{T}(0)/\widetilde{T})}} = \int \sqrt{2\widetilde{\lambda}_3 \widetilde{\epsilon}} \mathrm{d}\widetilde{x}. \tag{2.48}$$

Let $z = \sqrt{\ln(\widetilde{T}(0)/\widetilde{T})}$ and rewrite the left hand side as a function of z. Notice that $\widetilde{T}(z) = \widetilde{T}(0)\exp(-z^2)$ and $\mathrm{d}\widetilde{T} = -\widetilde{T}(0)\exp(-z^2)2z\mathrm{d}z$. The integral becomes

$$\int e^{-z^2} \mathrm{d}z = \frac{\sqrt{\pi}}{2}\,\mathrm{erf}(z) = \sqrt{\frac{\widetilde{\lambda}_3 \widetilde{\epsilon}}{2\widetilde{T}(0)^2}}\widetilde{x}. \tag{2.49}$$

And we obtain the temperature profile,

$$\widetilde{T}(x) = \widetilde{T}(0)\exp\left[-\operatorname{erf}^{-1}\left(\sqrt{\frac{\widetilde{\lambda}_3\widetilde{\epsilon}}{2\widetilde{T}(0)^2}}\widetilde{x}\right)\right]. \tag{2.50}$$

The above expression contains two unknown quantities, $\widetilde{\epsilon}$ and $T(0)$. First, let us consider $\widetilde{\epsilon}$. It turns out that it is not necessary to obtain ϵ from the integration of temperature profile as before. Instead, integrating Eq. (2.44) over the whole volume, we obtain

$$\left.\frac{\mathrm{d}\widetilde{T}}{\mathrm{d}\widetilde{x}}\right|_{\widetilde{x}=-1}^{\widetilde{x}=1} = 2y(1) = 2\widetilde{\lambda}_3, \tag{2.51}$$

where we have used $\int n(\widetilde{x})d\widetilde{x} = 2n_0$; $\mathrm{d}\widetilde{T}/\mathrm{d}\widetilde{x}$ is symmetric at $\widetilde{x} = \pm 1$; and $y(\widetilde{T}_0) = y(1) = \sqrt{2\widetilde{\lambda}_3\widetilde{\epsilon}\ln(\widetilde{T}(0))}$. To simplify notations, we define $\omega \equiv \sqrt{\ln \widetilde{T}(0)}$. Then, ϵ is linked to $\widetilde{T}(0)$ in (2.51) with

$$\widetilde{\epsilon} = \frac{\widetilde{\lambda}_3}{2\ln\widetilde{T}(0)} = \frac{\widetilde{\lambda}_3}{2\omega^2}. \tag{2.52}$$

Next, consider another relation that links $\widetilde{\epsilon}$ and $\widetilde{T}(0)$, Eq. (2.49). Notice that at $\widetilde{x} = 1$, $\widetilde{T} = 1$ and $z = \omega$; and $\widetilde{T}(0) = \exp(\omega^2)$. Then, (2.49) can be rewritten as a relation of ω: the second term becomes $\sqrt{\pi}\operatorname{erf}(\omega)/2$; the last term becomes $\widetilde{\lambda}_3\exp(-\omega^2)/2\omega$, where we have substituted Eq. (2.52). Rearrange terms, we get

$$\operatorname{erf}(\omega) = \frac{\widetilde{\lambda}_3}{\sqrt{\pi}}\frac{\exp(-\omega^2)}{\omega}. \tag{2.53}$$

From this implicit function, ω and hence $\widetilde{T}(0)$ are obtained numerically. Consequently, the energy density is obtained using Eq. (2.52). Moreover, using ω, the expression of the temperature profile (2.50) is simplified to

$$\widetilde{T}(\widetilde{x}) = \exp\left[\omega^2 - \left(\operatorname{erf}^{-1}\left(\operatorname{erf}(\omega)\widetilde{x}\right)\right)^2\right], \tag{2.54}$$

which is also obtained.

Since the total number of particles is fixed, the total heat flow is

$$J_U = \frac{\mathcal{A}kT_0}{L}2\widetilde{\lambda}_3. \tag{2.55}$$

Together with the energy density given by Eq. (2.52), we obtain

$$\mathcal{T} = \frac{\epsilon_0}{n_0\lambda_3}\left(\frac{\widetilde{\lambda}_3}{2\ln\widetilde{T}(0)} - 1\right) = \frac{\epsilon_0}{n_0\lambda_3}\left(\frac{\widetilde{\lambda}_3}{2\omega^2} - 1\right). \tag{2.56}$$

Following the same procedure, the energy density of the subsystem satisfies

$$\tilde{\epsilon}_1 = \frac{\tilde{\lambda}_3(1+\tilde{x}_1)^2}{2\omega_1^2} \quad \text{and} \quad \tilde{\epsilon}_2 = \frac{\tilde{\lambda}_3(1-\tilde{x}_1)^2}{2\omega_2^2}, \tag{2.57}$$

with $\omega_1 = \sqrt{\ln \tilde{T}_1(\tilde{x}_1)}$ and $\omega_2 = \sqrt{\ln \tilde{T}_2(\tilde{x}_1)}$. Their values can be obtained from the implicit functions

$$\operatorname{erf}(\omega_1) = \frac{\tilde{\lambda}_3(1+\tilde{x}_1)^2}{\sqrt{\pi}} \frac{\exp(-\omega_1^2)}{\omega_1}, \tag{2.58}$$

$$\operatorname{erf}(\omega_2) = \frac{\tilde{\lambda}_3(1-\tilde{x}_1)^2}{\sqrt{\pi}} \frac{\exp(-\omega_2^2)}{\omega_2}. \tag{2.59}$$

The total outgoing heat flow remains the same $J_{tot} = J_U$. Finally,

$$\begin{aligned} \mathcal{T}_{1|2} &= \frac{\epsilon_0}{\lambda_3 n_0}\left(\frac{(1+\tilde{x}_1)^3\tilde{\lambda}_3}{4\ln \tilde{T}_1(\tilde{x}_1)} + \frac{(1-\tilde{x}_1)^3\tilde{\lambda}_3}{4\ln \tilde{T}_2(\tilde{x}_1)} - 1\right), \\ &= \frac{\epsilon_0}{\lambda_3 n_0}\left(\frac{(1+\tilde{x}_1)^3\tilde{\lambda}_3}{4\omega_1^2} + \frac{(1-\tilde{x}_1)^3\tilde{\lambda}_3}{4\omega_2^2} - 1\right). \end{aligned} \tag{2.60}$$

An example of the comparison between the constrained and unconstrained system is shown in Fig. 2.4. Due to the presence of the implicit functions, analytical analysis of the comparison is difficult. Instead, like **case 2**, we directly inspect the system at several λ_3 and find the inequality $\mathcal{T} \leq \mathcal{T}_{1|2}$ holds in these instances.

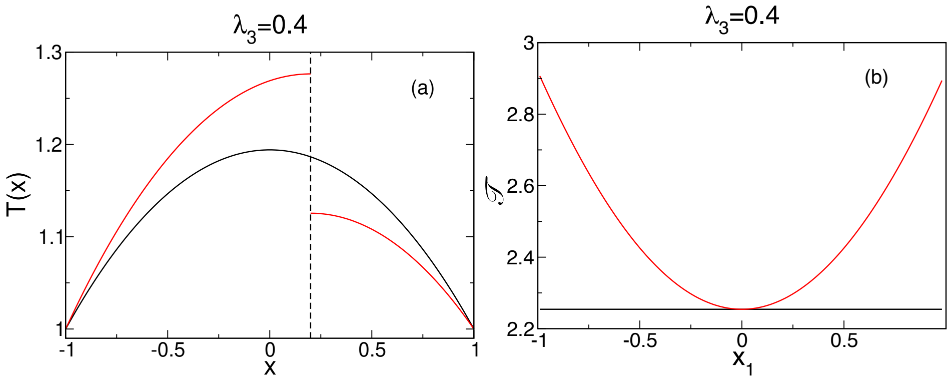

Figure 2.4: Comparison between constrained (red) and unconstrained system (black) of **case 3**: ideal gas under energy supply scheme $\sigma_E(\vec{r}) = \lambda_3 n(\vec{r})$. (a) Comparison of the normalised temperature profiles $T(x)$. The constraint is at $x = 0.2$, denoted by the vertical dashed line. (b) Comparison between (reduced) $\mathcal{T}$ at various constraint positions x_1 (in units of L).

case 4. $k \propto \sqrt{T}$ from kinetic theory In previous cases, we have assumed the heat conductivity to be constant, $k = \text{const}$. In this case, we consider the heat conductivity given by the kinetic theory, $k \sim \sqrt{T}$. From the kinetic theory, we have explicitly [52]

$$k = \frac{mC_V}{3\sqrt{2}\sigma}\langle v \rangle, \tag{2.61}$$

where m is the mass of the particle, C_V is the heat capacity, σ is the collision cross section and $\langle v \rangle = \sqrt{8T/\pi m}$ is the averaged velocity. To simplify, we collect all constants into $c = (2/3)C_V\sqrt{m/\pi}$, and write $k = c\sqrt{T}$. Eq. (2.7) is now

$$\nabla \cdot (-k\nabla T) = -c\frac{\mathrm{d}}{\mathrm{d}x}\left(\sqrt{T}\frac{\mathrm{d}}{\mathrm{d}x}T\right) = \sigma_E. \tag{2.62}$$

Furthermore, by assigning $k' \equiv 2c/3$, the equation is simplified to

$$\frac{\mathrm{d}^2}{\mathrm{d}x^2}\left(T^{3/2}\right) + \frac{\sigma_E}{k'} = 0. \tag{2.63}$$

Here, we focus on the simplest case where $\sigma_E = \lambda_1$. The analysis can be applied to other cases of σ_E.

As always, to obtain temperature profiles, we rewrite Eq. (2.63) in the dimensionless form

$$\frac{\mathrm{d}^2}{\mathrm{d}\widetilde{x}^2}\left(\widetilde{T}^{3/2}\right) + \widetilde{\lambda}_1 = 0. \tag{2.64}$$

with $\widetilde{\lambda}_1 = \lambda_1 L^2/(k' T_0^{3/2})$. The only difference between Eq. (2.64) with that of **case 1** is the power $3/2$. Therefore, the temperature profile is

$$\widetilde{T}(\widetilde{x}) = \left(-\frac{\widetilde{\lambda}_1}{2}\widetilde{x}^2 + \frac{\widetilde{\lambda}_1}{2} + 1\right)^{2/3}, \tag{2.65}$$

and for subsystems under a constraint at $x_1 = \widetilde{x}_1 L$,

$$\widetilde{T}_1(\widetilde{x}) = \left(-\frac{\widetilde{\lambda}_1}{2}(\widetilde{x} - \widetilde{x}_1)^2 + \frac{\widetilde{\lambda}}{2}(1 + \widetilde{x}_1)^2 + 1\right)^{2/3}, \tag{2.66}$$

$$\widetilde{T}_2(\widetilde{x}) = \left(-\frac{\widetilde{\lambda}_1}{2}(\widetilde{x} - \widetilde{x}_1)^2 + \frac{\widetilde{\lambda}_1}{2}(1 - \widetilde{x}_1)^2 + 1\right)^{2/3}. \tag{2.67}$$

The energy densities are obtained with the help of the following integrals

$$A = \int_{-1}^{1} \frac{1}{\widetilde{T}(\widetilde{x})}\mathrm{d}\widetilde{x}, \quad B = \int_{-1}^{\widetilde{x}_1} \frac{1}{\widetilde{T}_1(\widetilde{x})}\mathrm{d}\widetilde{x}, \quad C = \int_{\widetilde{x}_1}^{1} \frac{1}{\widetilde{T}_2(\widetilde{x})}\mathrm{d}\widetilde{x}. \tag{2.68}$$

And the energy densities of the system and subsystems are

$$\widetilde{\epsilon} = \frac{2}{A}, \quad \widetilde{\epsilon}_1 = \frac{1 + \widetilde{x}_1}{B} \quad \text{and} \quad \widetilde{\epsilon}_2 = \frac{1 - \widetilde{x}_1}{C}, \tag{2.69}$$

respectively. The integrals A, B, and C are hypergeometric functions, and their values are obtained numerically. In addition, the total outgoing heat flow is not changed by the constraint $J_{tot} = J_U = 2L\mathcal{A}\lambda_1$. Now, we have obtained all the quantities needed for $\mathcal{T}$ and $\mathcal{T}_{1|2}$.

Values of $\mathcal{T}$ and $\mathcal{T}_{1|2}$ are obtained numerically. Due to the presence of hypergeometric functions, it is difficult to compare $\mathcal{T}$ and $\mathcal{T}_{1|2}$ analytically. We again analyse their values numerically at several λ_1, and results show that $\mathcal{T} \leq \mathcal{T}_{1|2}$. Here, we present results of two situations, $\widetilde{\lambda}_1 = 0.5$ and 15, in Fig. 2.5.

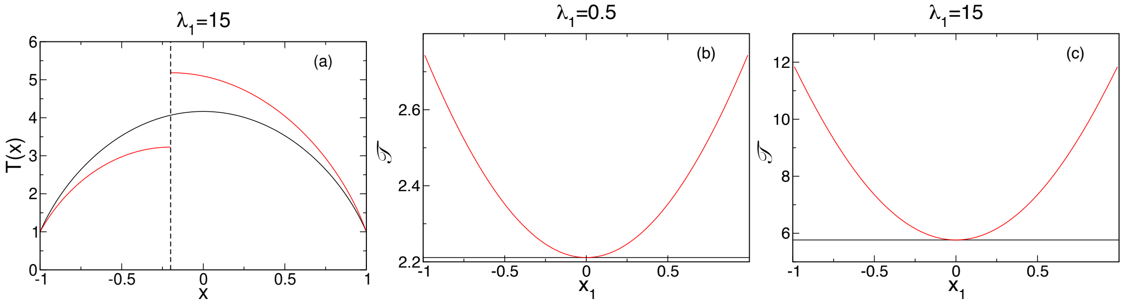

Figure 2.5: Comparison between constrained (red) and unconstrained system (black) of **case 4**: an ideal gas with heat conductivity $k = c\sqrt{T}$ and local energy supply rate $\sigma_E = \lambda_1$. (a) Comparison between the normalised temperature profiles $T(x)$. (b) Comparison between (reduced) $\mathcal{T}$ at $\lambda_1 = 0.5$ and (c) at $\lambda_1 = 15$. λ_1 is measured in units of $k'T^{3/2}/L^2$.

2.2.1.3 Diathermal Constraint

case 5. $\sigma_E = \lambda_1$ with diathermal constraint In this model, we consider again the case of a homogeneous energy supply. The internal constraint, however, is a diathermal wall. As a result, the subsystems are now coupled through heat exchange.

In the presence of the diathermal wall, new boundary conditions are introduced at the constraint. These new conditions are $T_1(x_1) = T_2(x_1)$ and $\mathrm{d}T_1(x)/\mathrm{d}x|_{x_1} = \mathrm{d}T_2(x)/\mathrm{d}x|_{x_1}$ for a constraint at x_1. In other words, the subsystem temperature profile $T_i(x)$ is not changed by the constraint, *i.e.*, $T_1(x) = T_2(x) = T(x)$ in their respective domains. Consequently, the energy densities are

$$\epsilon_1 = \frac{\epsilon_0(1+\widetilde{x}_1)\sqrt{\widetilde{\lambda}_1(\widetilde{\lambda}_1+2)}}{2\,\mathrm{Arctanh}\left(\sqrt{\widetilde{\lambda}_1/(\widetilde{\lambda}_1+2)}\right) + 2\,\mathrm{Arctanh}\left(\widetilde{x}_1\sqrt{\widetilde{\lambda}_1/(\widetilde{\lambda}_1+2)}\right)}, \tag{2.70}$$

$$\epsilon_2 = \frac{\epsilon_0(1-\widetilde{x}_1)\sqrt{\widetilde{\lambda}_1(\widetilde{\lambda}_1+2)}}{2\,\mathrm{Arctanh}\left(\sqrt{\widetilde{\lambda}_1/(\widetilde{\lambda}_1+2)}\right) - 2\,\mathrm{Arctanh}\left(\widetilde{x}_1\sqrt{\widetilde{\lambda}_1/(\widetilde{\lambda}_1+2)}\right)}. \tag{2.71}$$

In addition, the total outgoing heat flow is not changed by the constraint, $J_{U_1} + J_{U_2} = J_U = 2L\mathcal{A}\lambda_1$.

Combining the above relations, we obtain $\mathcal{T}_{1|2}$ through

$$\mathcal{T}_{1|2} = \frac{\epsilon_1(1+\widetilde{x}_1) + \epsilon_2(1-\widetilde{x}_1) - 2\epsilon_0}{2\lambda_1}. \tag{2.72}$$

And the expression of $\mathcal{T}$ has been obtained in Eq. (2.23). The comparison between $\mathcal{T}$ and $\mathcal{T}_{1|2}$ reduces to the comparison of

$$\epsilon \text{ and } \frac{\epsilon_1(1+\widetilde{x}_1)}{2} + \frac{\epsilon_2(1-\widetilde{x}_1)}{2}. \tag{2.73}$$

Let us assume that $\epsilon \leq (\epsilon_1(1+\widetilde{x}_1) + \epsilon_2(1-\widetilde{x}_1))/2$. Dividing both sides by ϵ gives,

$$1 \leq \frac{(1+\widetilde{x}_1)^2}{2+2a} + \frac{(1-\widetilde{x}_1)^2}{2-2a}, \tag{2.74}$$

where $a = \operatorname{Arctanh}(\widetilde{x}_1\sqrt{\widetilde{\lambda}/(\widetilde{\lambda}+2)})/\operatorname{Arctanh}(\sqrt{\widetilde{\lambda}/(\widetilde{\lambda}+2)})$. We note that for $\widetilde{x}_1 \in (-1,1)$, $a \in (-1,1)$, and hence the common denominator is positive, $(2+2a)(2-2a) \geq 0$. Multiplying both sides of Eq. (2.74) by this common denominator and rearranging terms, we obtain

$$0 \leq (a - \widetilde{x}_1)^2, \tag{2.75}$$

which is always true. Hence, we have verified for all values of λ_1 that $\mathcal{T} \leq \mathcal{T}_{1|2}$. This model supports Hypothesis 2.1.1.

2.2.2 Lennard-Jones Fluid

The assumptions of local equilibrium and constant pressure are central to our analysis of the ideal gas model. But how accurate are these assumptions? To test the validity of our analytical results of the ideal gas model, we compare our results with the simulation results of a Lennard-Jones system. The results in this section are reproduced from [1].

In reference [1], a Lennard-Jones system under external energy supply is simulated using *molecular dynamics* (MD). In MD simulations, particles evolve according to Newtonian equations of motion, and physical quantities are obtained through direct time averages. Therefore, in this simulation method, no assumptions are made regarding local equilibrium, constant pressure, or constant heat conductivity. Nevertheless, the authors observe that the system stays close to local equilibrium. A violation of the local equilibrium assumption is expected when the system experiences an energy flow much faster than the local energy distribution rate, such as a shock wave.

The parameters of the simulation system are as follows. The system has a fixed number of particles $N = 266,240$, with a fixed volume of dimensions $L_x = L_y = 35.22$ and $L_z = 281.76$ in the x, y and $z-$axis. Here, all lengths are measured in units of $r_0 = 0.35nm$. Periodic boundary conditions are applied in x and y directions. The boundary temperatures are kept at $T_0 = 0.8$, in units of ε/k_B which is set to $120K$. In addition, as the internal constraint, a thin wall of width $\Delta = 4.4$ is present in the system. This constraint separates the system into two subsystems of length L_1 and L_2. The constants are chosen such that they correspond to the experimental results of liquid argon [63]. A schematic representation of this system is shown in Fig. 2.6.

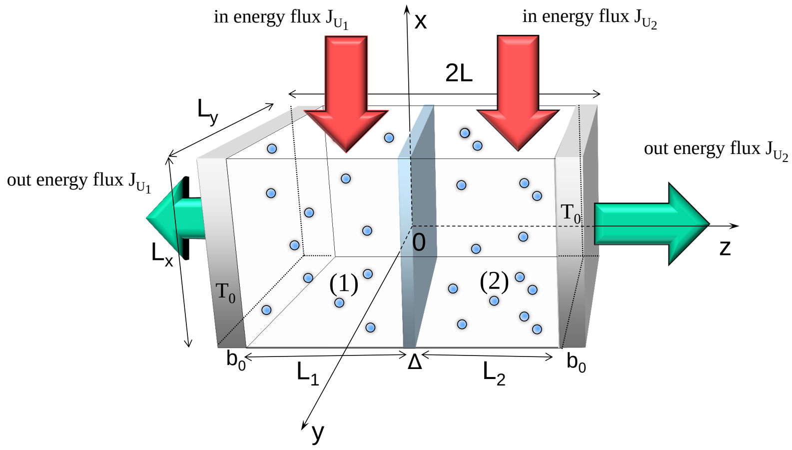

Figure 2.6: Scheme of Lennard-Jones simulation system. The system has dimensions of $L_x = L_y = 35.22$ and $L_z = 281.76$ denoted as $2L$. Lengths are measured in units of $r_0 = 0.35nm$. The walls at the boundaries are of width $b_0 = 2.2$. The internal constraint is of width Δ, separating the system into subsystems of width L_1 and L_2. Energy is dissipated through the boundaries, denoted as J_{U_1} and J_{U_2}. Figure reproduced from [1].

Particles interact via the shifted Lennard-Jones potential [64]

$$u(r_{ij}) = \begin{cases} 4\left(\frac{1}{r_{ij}^{12}} - \frac{1}{r_{ij}^{6}}\right) - u(r_c) & r_{ij} \leq r_c, \\ 0 & r_{ij} > r_c, \end{cases} \tag{2.76}$$

where r_{ij} is the distance between a pair of particles i and j, and all energies are measured in units of $\varepsilon = 120k_B$. This potential is truncated and shifted, such that the potential is 0 beyond a cut off distance $r_c = 2.5$. The particles interact with the boundary walls repulsively, via potential

$$u(z) = (z - z_0)^2 \cdot \theta(\mp(z - z_0)), \tag{2.77}$$

where θ is the Heaviside function; z_0 is the position of the external boundaries with $z_0 = 0$ and $2L$ for the left and right boundary, respectively; the coefficient in θ is -1 for $z_0 = 0$ and $+1$ for $z_0 = 2L$. We remark that at the thickness of the constraint Δ, the particles do not interact. Hence, the constraint is effectively adiabatic.

In total, simulations are performed for three methods of energy input, corresponding to **case 1, 2** and **3** of the ideal gas model in Sec. 2.2.1.2. In each case, the total energy flowing into the system is kept constant regardless of the position of the constraint, *i.e.*, $J_U = J_{U_1} + J_{U_2}$. Additionally, J_U is kept the same for all three cases for later comparison.

Energies are added every 10 time steps (time step measured in units of $(mr_0^2/\varepsilon)^{1/2} \approx 2.16 \times 10^{-12}s$) in the following manner. For **case 1**, where the energy input is homogeneous $\sigma_E = \lambda_1$, the total amount of kinetic energy is separated proportional to the subsystem volume, then distributed equally among the particles. For **case 2**, where the local energy source is proportional to the local temperature $\sigma_E = \lambda_2 T(\vec{r})$, each particle receives a kinetic energy that is proportional to its current kinetic energy. Finally, for **case 3**, where the local energy source is proportional to the local particle density $\sigma_E = \lambda_3 n(\vec{r})$, each particle receives the same amount of energy.

Simulation results are shown in Fig. 2.7. The figure is taken from paper [1]: panels (a)-(b) are in the supplementary; panels (c)-(e) are in Fig. 2 of the paper. All quantities are presented in dimensionless forms with units described previously. First of all, a comparison between temperature profiles under different protocols, three cases from the Lennard-Jones simulation and three cases from the ideal gas model, are shown in panel (a). The analytical results are with fitted $\lambda_i, i = 1, 2, 3$, such that $T(0)$ matches the temperature at 0 from the simulation results. Qualitatively, the simulation results agree with the analytical results. Second, the total energy storage (per particle) is shown in panel (c). These results show that $\Delta U = \Delta U_{tot}(L_1 = L) \leq \Delta U_{tot}$, in agreement with the hypothesis $\mathcal{T} \leq \mathcal{T}_{1|2}$.

In addition, to better understand the physical meaning of $\mathcal{T}$, authors in [1] also measure the energy relaxation of subsystem 1 after the shut-down of the external energy supply. Specifically, Fig. 2.7 (b) shows that the energy storage of subsystem 1 decays exponentially, initially; (e) shows that, except for small L_i, the decay time $\mathcal{T}$ (of subsystem 1) approximates $2\Delta U_1/J_{U_1}$. These two results show that the initial energy decay (of subsystem 1) follows $\exp(-t/\mathcal{T})$, where $\mathcal{T} = 2\Delta U_1/J_{U_1}$. Factor 2 appears because the subsystem energy dissipates via only one boundary. Therefore, the authors conclude that in the general system with energy storage ΔU and total heat flow J_U, the initial decay time is given by $\mathcal{T} = \Delta U/J_U$. Finally, panel (d) remarks that the energy storage is not extensive.

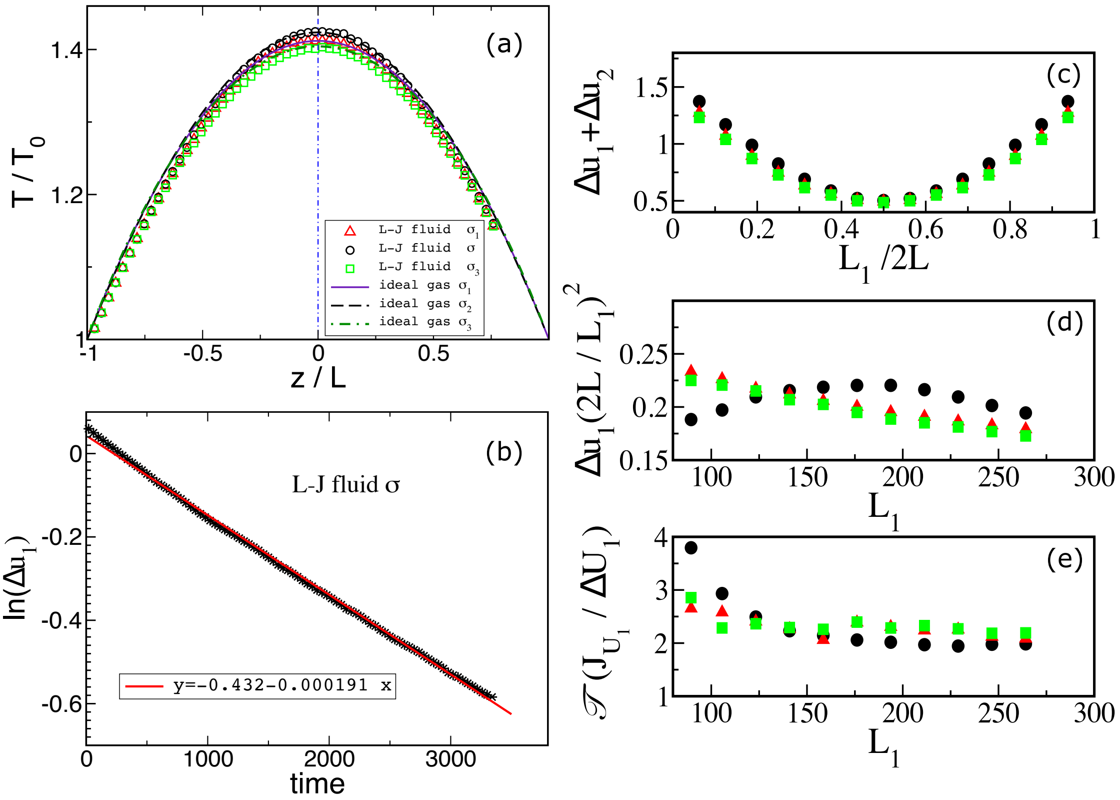

Figure 2.7: Reproduced from [1]. (a) Scaled temperature profiles in steady states under three methods of energy supply: **case 1**, $\sigma_E = \lambda_1$ (red triangles); **case 2**, $\sigma_E = \lambda_2 T(z)$ (black circles); **case 3**, $\sigma_E = \lambda_3 n(z)$ (green squares). Simulation results are shown in symbols; analytical results of the ideal gas are shown in lines of the same colour. The coefficients $\lambda_i, i = 1, 2, 3$ are chosen such that $T(z)$ matches the simulation results at $z/L = 0$. (b) Initial decay of the energy storage of subsystem 1 per particle, Δu_1, as a function of time t after shut-down of the energy flux into the system. Time is measured in units of $(mr_0^2/\varepsilon)^{1/2} \approx 2.16 \times 10^{-12}s$. (c) Total energy storage per particle plotted against the (normalised) size of subsystem 1, L_1. (d) Energy storage per particle of subsystem 1 plotted against L_1. Energy is measured in units of $(L_1/2L)^2$. (e) Characteristic time $\mathcal{T}$ as a function of the size of subsystem 1.

2.3 Systems under Flow

In the previous section, we have described models subjected to bulk energy supplies. In this section, we will present models driven by an external energy flow. This energy flow can come in the form of heat or matter.

We consider three models, each based on a distinct system. In the first case, we consider an ideal gas driven by an external heat flow. In the second case, we consider a Poiseuille flow – a fluid system driven by a matter flow. In the final case, we present the simulation results of a two-dimensional Rayleigh-Bénard system, a fluid system driven by an external heat flow and under gravitation.

The author would like to point out that, as with the results in Sec. 2.2.2, the results of the Rayleigh-Bénard system is reproduced from [1], where the simulation is performed by the group of Prof. Banaszak. Again, these results are presented here for a more holistic view.

2.3.1 Heat Flow in Ideal Gas

2.3.1.1 Set-up

Consider a three-dimensional ideal gas confined between two walls. The walls are kept at different temperatures T_1 and T_0 with $T_1 \geq T_0$. This temperature gradient generates a constant heat flow across the system. The system reaches nonequilibrium steady states without the need for a bulk energy supply, *i.e.*, $\sigma_E(\vec{r}) = 0$. Therefore, the equation for obtaining temperature profile (2.7) is now a Laplace equation

$$\nabla^2 T(\vec{r}) = 0. \tag{2.78}$$

The system is closed with a fixed number of particles N and volume V. The walls are of a large area $\mathcal{A} = H \times Z$ with height H and width Z, and are placed at $x = 0$ and $x = L$. The volume is hence $V = \mathcal{A} \times L$. A scheme of the system is shown in Fig. 2.8 (a).

As internal constraints, adiabatic walls with predefined shapes are used. At first, one may consider choosing the horizontal surface at $x = y = 0$ as the constraint. Yet, since this constraint does not alter the temperature profile, it does not change the total heat flow J_U. However, in this section, we intend to study models where J_U can be altered by the constraint. Therefore, the constraint is chosen with particular shapes that can modify J_U. Additionally, these configurations need to satisfy two criteria. First, all constraints needs to be fixed at the line $(x, y, z) = (L/2, 0, 0) + t(0, 0, 1)$. Thereby the resulting subsystems are symmetric. Furthermore, they need to ensure a non-zero heat flow in each subsystem. In other words, each subsystem is always in contact with both boundaries.

Under the above considerations, we consider three configurations which we refer to as *vertical*, *linear*, and *cosine*. In *verticle*, the constraint extends from left to right in a zigzag manner. The parameter that we can adjust is the height of the wall h. In *linear*,

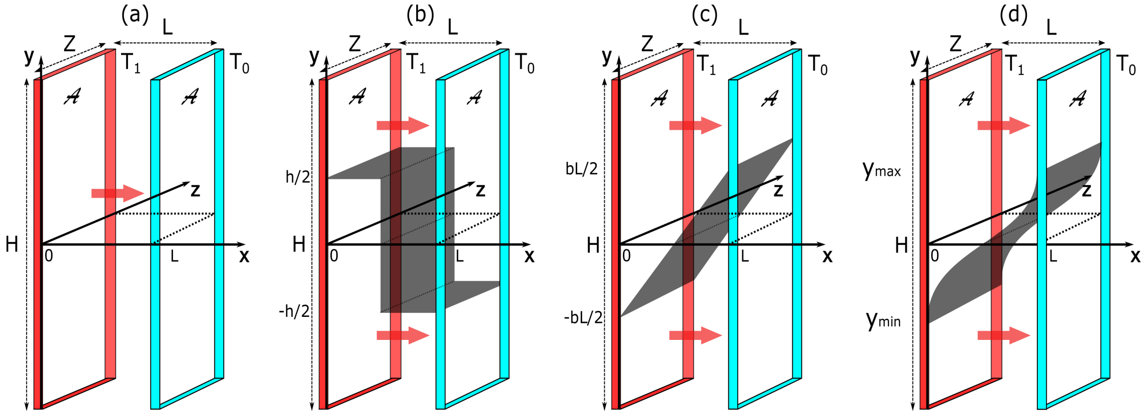

Figure 2.8: Schemes of (a) unconstrained and $(b)(c)(d)$ constrained ideal gas systems under an external heat flow. Two diathermal walls are placed at $x = 0$ and L, kept at temperatures T_1 and T_0, respectively. The constraints are adiabatic walls, denoted in black. In (b), the constraint has a height h and extends from $(0, h/2)$ to $(L/2, h/2)$ to $(L/2, -h/2)$ to $(L, -h/2)$. In (c), the constraint has a slope b and stretches from $(0, -bL/2)$ to $(L, bL/2)$. In (d), the constraint is in the shape of a cosine function of wavenumber $\hat{k}$. It extends from $(0, H/2 + \pi/2\hat{k})$ to $(0, H/2 - \pi/2\hat{k})$, corresponding to phase $(0, \pi)$. The red arrows denote the heat flux.

the constraint is a flat surface with an adjustable slope b. In *cosine*, the shape of the constraint is a cosine function between phase $(0, \pi)$. In this way, it connects smoothly to the boundaries. The parameter to adjust is the wavenumber $\hat{k}$. These constraints are explicitly expressed as

$$\begin{cases} \text{vertical:} & y = \frac{h}{2} - h \cdot \theta(x - \frac{L}{2}), \\ \text{linear:} & y = b(x - \frac{L}{2}), \\ \text{cosine:} & x = \frac{L}{2} \cos\left(\hat{k}(y - \frac{H}{2}) + \frac{\pi}{2}\right) + \frac{L}{2}, \end{cases} \tag{2.79}$$

wherein *vertical*, $\theta(x)$ is the Heaviside function; in *cosine*, the function is valid within the range,

$$y \in \left(\frac{H}{2} - \frac{\pi}{2\hat{k}}, \frac{H}{2} + \frac{\pi}{2\hat{k}}\right). \tag{2.80}$$

Schemes of these constraints are shown in Fig. 2.8.

The energy storage and the total heat flow of the unconstraint system are straightforward. The temperature profile depends solely on x, $T(\vec{r}) = T(x)$. Eq. (2.78) is now $\partial_x^2 T(x) = 0$, with boundary conditions $T(0) = T_1$ and $T(L) = T_0$. Solving this equation, we have

$$T(x) = \frac{T_0 - T_1}{L} x + T_1, \tag{2.81}$$

i.e., the temperature profile is linear. The energy density (2.12) is hence,

$$\epsilon = \epsilon_0 \frac{\widetilde{T}_1 - 1}{\ln \widetilde{T}_1}, \tag{2.82}$$

where $\widetilde{T_1} = T_1/T_0$.

The heat flow is obtained using Eq. (2.15), where we need the expressions of the local heat flux $\vec{J}_E$ and the normal of the enclosing surface $\hat{n}$. The normal of the left and right boundary is $\hat{n} = (-1,0,0)$ and $(1,0,0)$ respectively. The local heat flux is given by

$$\vec{J}_E(\vec{r}) = -k\Big(\partial_x T(\vec{r}), \partial_y T(\vec{r}), \partial_z T(\vec{r})\Big), \tag{2.83}$$

where k is the heat conductivity, same as before. Since we have set $T_1 \geq T_0$, the heat flows from the left boundary to the right boundary. Moreover, since all incoming and outgoing energy of the system is in the form of heat, the total heat flow J_U can be calculated at either boundary,

$$\begin{aligned} \dot{E}_{in} &= \dot{Q}_{in} = k \int_Z \mathrm{d}z \int_Y \partial_x T(\vec{r}) \mid_{x=0} \mathrm{d}y, \\ \dot{E}_{out} &= \dot{Q}_{out} = k \int_Z \mathrm{d}z \int_Y \partial_x T(\vec{r}) \mid_{x=L} \mathrm{d}y. \end{aligned} \tag{2.84}$$

For the unconstrained case, this gives

$$J_U = \frac{k\mathcal{A}T_0}{L}(\widetilde{T_1} - 1). \tag{2.85}$$

Together with Eq. (2.82), we obtain

$$\mathcal{T} = \frac{L^2}{kT_0}\frac{\epsilon_0}{\ln \widetilde{T_1}}. \tag{2.86}$$

We now present general expressions for ΔU and J_U of the constrained system. For the constrained system, generally, the temperature profile depends on both x, y-coordinate, $T(\vec{r}) = T(x,y)$. To obtain this temperature profile is to solve the 2-dimensional Laplace equation $\nabla^2 T(x,y) = 0$ with the following boundary conditions,

$$\begin{cases} T_1(0,y) = T_1, & T_2(0,y) = T_1, \\ T_1(L,y) = T_0, & T_2(L,y) = T_0, \\ T_1(x,-\frac{H}{2}) = \frac{T_0 - T_1}{L}x + T_1, & T_2(x,\frac{H}{2}) = T_2(x,-\frac{H}{2}), \\ \partial_{\hat{n}} T_1(x,y) \mid_{y=w(x)} = 0, & \partial_{\hat{n}} T_2(x,y) \mid_{y=w(x)} = 0, \end{cases} \tag{2.87}$$

These boundary conditions are: Dirichlet boundary conditions at the left and right boundaries $x = 0$ and L, since the system is in contact with the plates; Dirichlet boundary conditions at $y = \pm H/2$, as the system is bounded adiabatically at the top and bottom plates; Neumann boundary conditions at the constraints $w(x)$ (expressions given by Eq. (2.79)), since the constraints are adiabatic, where $\hat{n}$ is the normal of the constraints.

The above Laplace equation is solved numerically using the *finite element method* (FEM). We will explain this method in the following subsection. For now, let us assume that we have already obtained the temperature profile $T(x,y)$ numerically. From this, the energy storage is again calculated using Eq. (2.18) with numerical integration. And the total heat flow J_{tot} is calculated according to Eq. (2.84). The integration can be separated into integrals over each subsystem, explicitly written as

$$\begin{aligned} J_{tot} = J_{U_1} + J_{U_2} &= kZ \int_{-H/2}^{y_0^*} \partial_x T_1(x,y) \mid_{x=0} \mathrm{d}y + kZ \int_{y_0^*}^{H/2} \partial_x T_2(x,y) \mid_{x=0} \mathrm{d}y, \\ &= kZ \int_{-H/2}^{y_L^*} \partial_x T_1(x,y) \mid_{x=L} \mathrm{d}y + kZ \int_{y_L^*}^{H/2} \partial_x T_2(x,y) \mid_{x=L} \mathrm{d}y, \end{aligned} \tag{2.88}$$

where y_0^* and y_L^* are the crossing points between the constraint and the left and right boundary, respectively.

2.3.1.2 Finite Element Method

The *finite element method* (FEM) is the most powerful method for solving differential equations and variational problems numerically. It can be applied to problems defined on arbitrary domains, arbitrary dimensions, and complex boundary conditions. It is thus widely used in mathematics and physics. It is also widely used in industrial applications, ranging from automobile and aerospace industries, to pharmaceutical and biotechnological industries [65–67].

To explain the basic idea behind FEM, let us look at an example. Consider a simple one-dimensional time independent differential equation that one would like to solve [65],

$$u''(x) = f(x). \tag{2.89}$$

We intend to find the best approximation function $\widetilde{u}(x)$ in the functional space with basis $\phi_i(x)$. The approximate function $\widetilde{u}(x)$ is a combination of chosen basis functions $\phi_i(x)$

$$\widetilde{u}(x) = \sum_i^N a_i \phi_i(x). \tag{2.90}$$

This gives a residual

$$R(x) = \widetilde{u}''(x) - f(x). \tag{2.91}$$

The problem of finding the best approximation then becomes the problem of finding the least residual.

Various methods can be employed to minimize the residual, such as the least square method, collocation method, and the Galerkin method [65]. We briefly introduce the Galerkin method here, as it is frequently used. In this method, using a series of test functions $w_i(x)$ with $i = 1, \cdots, N$, the problem of minimizing the residual is equivalently formalised to solve a series of

$$\int R(x) w_i(x) dx = 0, \tag{2.92}$$

for the N unknown variables a_i. In general, one can simply choose the basis functions as the weighted functions. Then the above integration functions can be rewritten using the inner product $(f,g) \equiv \int fg dx$,

$$\left(\widetilde{u}'' - f, \phi_i\right) = \left(\widetilde{u}'', \phi_i\right) - (f, \phi_i) = \sum_j a_j \left(\phi_j'', \phi_i\right) - (f, \phi_i) = 0. \tag{2.93}$$

Using integration by parts, the second order derivative can be reduced to

$$\left(\phi_j'', \phi_i\right) = \left(\phi_j', \phi_i'\right) - [\phi_j' \phi_i]_0^L. \tag{2.94}$$

Let us assume for simplicity, that the boundary conditions are such that $[\phi_j' \phi_i]_0^L = 0$. Then, the weighted residual equations can be written in the matrix format,

$$\sum_j a_j \mathrm{A}_{ij} - b_i = 0 \quad \text{or} \quad \vec{a}\mathbf{A} - \vec{b} = 0 \tag{2.95}$$

with the matrix elements $\mathrm{A}_{ij} = \left(\phi_j', \phi_i'\right)$ and vector components $b_i = (f, \phi_i)$ that concern only the basis functions and f.

The weighted residual method can be applied to an arbitrary region. However, using basis functions ϕ_i that are defined on the whole region of interest may result in large errors. FEM improves on this aspect by breaking any region into smaller regions called finite elements. Instead of global polynomials $\psi_i(x)$, finite element basis functions $\phi_i(x)$ are used. These basis functions are chosen such that they are only non-zero in a few of these elements (locally), and zero otherwise. An example of such basis functions is the Lagrange polynomials. Within each finite element, the solution function is approximated using the residual minimization method explained above. Finally, solutions in each finite element are combined to obtain the global solution.

Modern implementation of FEM often automated much of the process of generating mesh and obtaining the final approximation function through residual minimization. In this section, we use FEM implemented in Mathematica to obtain the temperature profiles numerically.

2.3.1.3 Results and Discussions

The temperature profiles of the constrained systems are obtained using FEM. From these profiles, we obtain the energy storage and heat flow using Eqs. (2.18) and (2.88). Examples of the temperature profiles are shown in Fig. 2.9.

The results of temperature profiles are subjected to numerical errors. The errors may come from two sources. The first major source of error is the conflicting boundary conditions, either at the crossing points between the constraint and external boundaries or the turning points of the constraint. To aid our explanation, in the schematic plot Fig. 2.10, each vertex on the graphs of the six subsystems – three different configurations, each

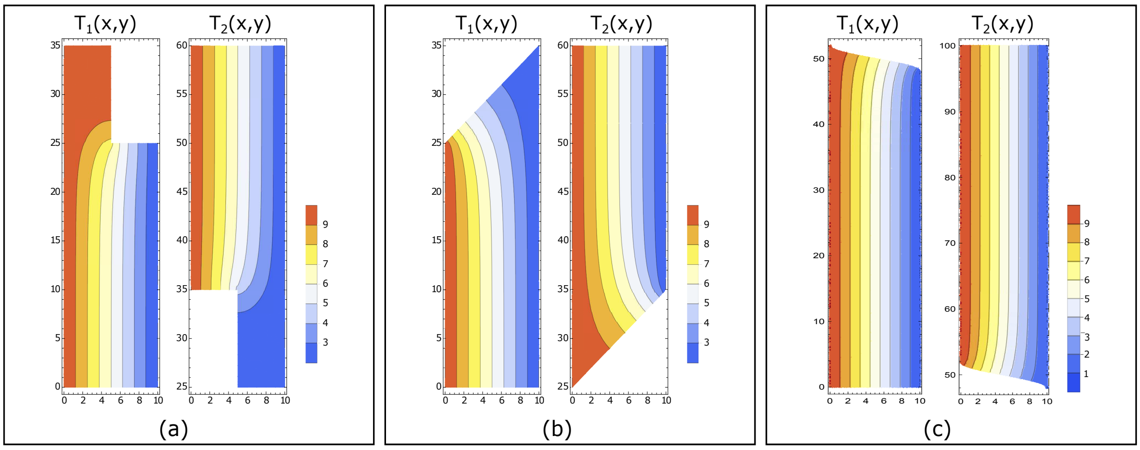

Figure 2.9: Contour plots of subsystem temperature profiles $T(x,y)$ under three constraint configurations. (a) Results under constraint *vertical*. The system is of size $(L,H) = (10,60)$; the height of the constraint is $h = 10$; the temperatures at the left and right boundaries are $T_1 = 10$ and $T_0 = 2$, respectively. (b) Results under constraint *linear*. The system size is $(L,H) = (10,60)$; the slope of the constraint is $b = 1$; $T_1 = 10$ and $T_0 = 2$. (c) Results under constraint *cosine*. The system size is $(L,H) = (10,100)$; the wavenumber of the constraint is $\hat{k} = 0.8$; $T_1 = 10$ and $T_0 = 1$.

with two subsystems – is denoted with v_i. The crossing points of all configurations are denoted as v_1 and v_4. For configuration *vertical*, there are additional turning points denoted with v_5, v_6.

Consider first the subsystems under constraint *linear*. At v_1 and v_4, heat fluxes are required, by the Dirichlet boundary conditions $T_i = \text{const}$, to be normal to the edge, $\vec{J}_E \propto (1,0,0)$. The heat flux, however, is also required, by the Neumann boundary condition at the constraint, to flow along the constraint $\vec{J}_E \propto (1,b,0)$. This conflict results in the numerical errors of $T(x,y)$ around v_1 and v_4. Similarly, numerical errors occur around the same regions for *cosine*. For *vertical*, since the constraint at v_1 and v_4 are normal to the boundaries, the heat flux directions agree. Errors appear, however, at v_6 and v_5, where the sharp turning of the constraint results in conflicting heat flux directions.

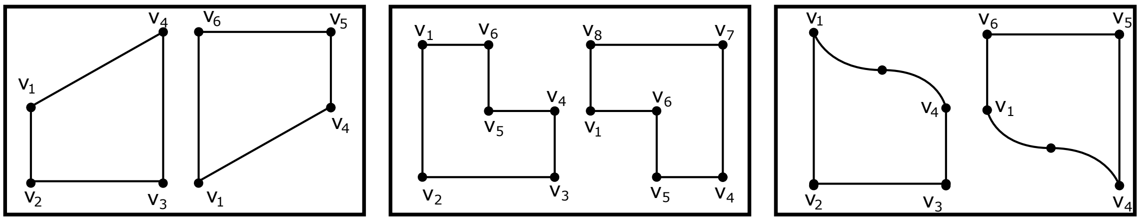

Figure 2.10: Schematics of graphs of subsystems under constraint configurations *linear, vertical*, and *cosine*. Each node is denoted with v_i.

Practically, using FEM, we observe that errors at these vertices are influenced by the angles. Errors at obtuse angles are larger than at acute angles, and are negligible for some acute angles. An example of the normal heat flux along the linear constraint $\partial_{\hat{n}} T(x,y)$ is shown in Fig. 2.11. One possible reason for the relation between error and angle is the size of the mesh. When the angle is small, the number of meshes in the region is small.

Since the variation of temperature profile within each region is small, it leaves little room for "overfitting". For obtuse angles, however, more meshes are present. Temperature profiles closer to each edge will "adapt" to the boundary condition on that edge. This may result in large temperature fluctuations in the region between the edges, and therefore large errors. Another way of interpretation is that, in the situation where conflicting boundary conditions are present, overfitting is not desirable. Obtuse angles are more likely to "overfit", which results in larger errors.

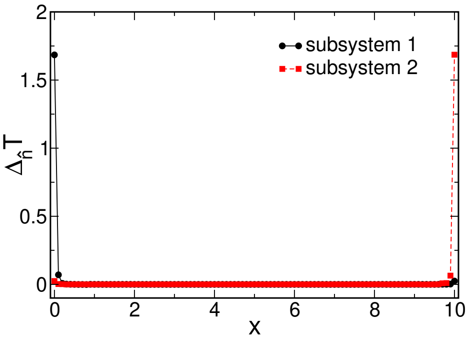

Figure 2.11: Numerical values of the normal heat flux along the adiabatic constraint $\nabla_{\hat{n}}T$. The model is under constraint configuration *linear* with slope $b = 0.5$. The dimension of the whole model is $L = 10, H = 100$. The left and right boundary temperature are $T_1 = 10.0$ and $T_0 = 1.0$, respectively.

Another source of error may come from the finite size effect. To estimate $\mathcal{T}$ in the thermodynamic limit, the range of parameters needs to be restricted to regions where this effect is negligible.

Due to the above-mentioned sources of error, it is important to obtain a valid range of parameters (with acceptable errors) for each model, before obtaining the final results of $\mathcal{T}$. Let us consider the first kind of numerical errors (the second kind of error will be discussed later). We notice that this source of error causes a discrepancy between J_{U_i} calculated from the left and right boundary, $J_{U_i}|_{x=0}$ and $J_{U_i}|_{x=L}$. A measure of error is defined from this discrepancy:

$$\text{error}_1 = \frac{J_{U_1}|_{x=L} - J_{U_1}|_{x=0}}{J_{U_1}|_{x=0}} \quad \text{and} \quad \text{error}_2 = \frac{J_{U_2}|_{x=L} - J_{U_2}|_{x=0}}{J_{U_2}|_{x=0}}. \tag{2.96}$$

In this section, we examine a variety of test models. Specifically, for constraints *linear* and *vertical*, we study models of dimensions $L = 10$, $H = 60, 80, 100, 150, 180, 200, 400$ and 600; for *cosine*, models of dimensions $L = 10$, $H = 80, 100, 120$. In addition, the boundary temperatures of these models are set to $T_1 = 10.0$ and $T_0 = 1.0$. For each model, error_i is evaluated at different parameter values, and the valid range of the parameter is restricted to $\text{error}_i \leq 1\%$. Results of error_i are shown in Fig. 2.12, and the corresponding valid range of the parameters is listed in Table 2.2.

The scaled energy storage $\Delta U_{tot}/V$, scaled total heat flow $J_{tot}/\mathcal{A}$, and $\mathcal{T}_{1|2}$ are evaluated at the scaled parameters x, where x represents $h/H, b/H$, and $1/\hat{k}H$ for *vertical*,

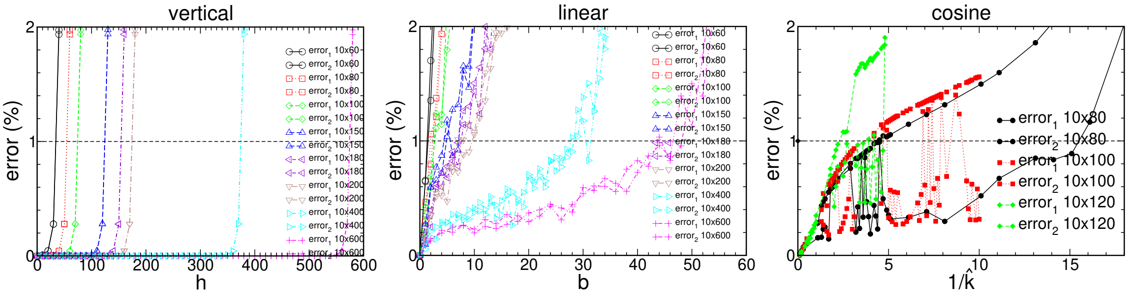

Figure 2.12: Error analysis of various models under three types of constraint configurations. The errors are plotted against the parameter of the constraints: height h for constraint *vertical*; slope b for *linear*; the inverse of wavenumber $1/\hat{k}$ for *cosine*. Errors are shown in percentages.

ver and *lin*

L, H	range h	range b
$10, 60$	$[0, 40)$	$[0, 2)$
$10, 80$	$[0, 60)$	$[0, 3)$
$10, 100$	$[0, 80)$	$[0, 4)$
$10, 150$	$[0, 130)$	$[0, 5)$
$10, 180$	$[0, 160)$	$[0, 8)$
$10, 200$	$[0, 180)$	$[0, 10)$
$10, 400$	$[0, 380)$	$[0, 29)$
$10, 600$	$[0, 580)$	$[0, 48)$

cos

L, H	range $1/\hat{k}$
$10, 80$	$(0, 4.6)$
$10, 100$	$(0, 4.2)$
$20, 120$	$(0, 2.4)$

Table 2.2: List of valid parameter ranges of different models. Each model is specified with length L, height H, and the valid parameter range of its internal constraint: range of height h for constraint configuration *vertical*; range of slope b for *vertical*; range of wavenumber (inverse) $1/\hat{k}$ for *cosine*.

linear, and *cosine* constraint, respectively. Results under these three types of constraints are shown in Fig. 2.13, 2.14, and 2.15, respectively. Each curve corresponds to a specific model whose size is denoted in the legend. In each figure, the parameters vary within the range in Table 2.2. For *linear* and *vertical*, each figure has an inset, showing results in a broader range. In all evaluated models, results show that $\mathcal{T}_{1|2}(x) \geq \mathcal{T}_{1|2}(0)$. Furthermore, $\mathcal{T}$ of the unconstrained system is the same as that of the constrained system under an equal partition, *i.e.*, $\mathcal{T}_{1|2}(0) = \mathcal{T}$. Therefore, for all tested models $\mathcal{T} \leq \mathcal{T}_{1|2}$, in accordance with Hypothesis 2.1.1.

It is worth pointing out that the results $\Delta U_{tot}/V$ can be used to discuss the error due to the finite size effect, the second source of error. The finite size effect can be observed from scaled functions: regions influenced by this effect will show data separation; regions unaffected will show data collapsing. For constraint *vertical*, Fig. 2.13 (a) shows that, except the model of dimension $L = 10, H = 60$, data collapse well over the whole range of h/H. And for *linear*, Fig. 2.14 (a) shows data collapsing over the whole range of b/H for models of dimensions $L = 10, H = 400, 600$. For *cosine*, the models examined are relatively small, and Fig. 2.15 (a) shows data collapsing over the range $1/\hat{k}H < 0.01$. For models with larger H, however, we expect data collapsing over the full range of $1/\hat{k}H$, same as in *vertical* and *linear*. Nevertheless, this second source of error does not influence our conclusion of $\mathcal{T} \leq \mathcal{T}_{1|2}$, since $\mathcal{T}_{1|2}$ is monotonic for all models within the valid range.

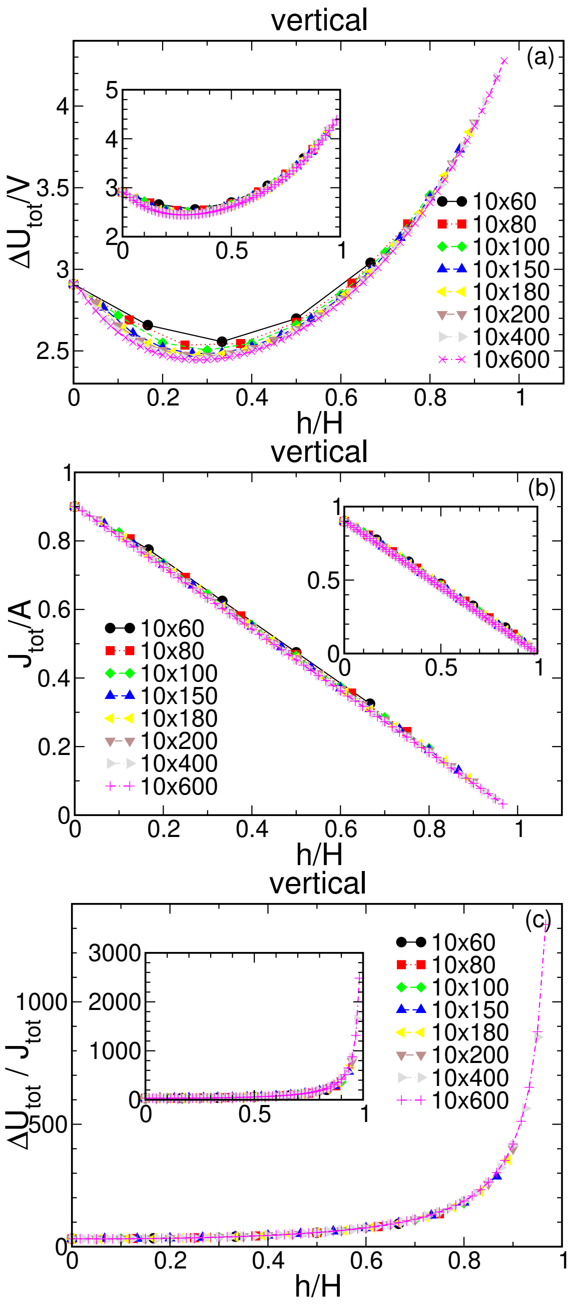

Figure 2.13: Plots of (a) total energy storage per unit volume $\Delta U_{tot}/V$, (b) total outgoing heat flow per unit area $J_{tot}/\mathcal{A}$, and (c) their ratio $\mathcal{T}_{1|2} = \Delta U_{tot}/J_{tot}$ against the normalised height h/H of constraint type *vertical*. Each panel is evaluated for six different system sizes of heights $H = 60$, 80, 100, 200, 400 and 600, and a fixed-length $L = 10$.

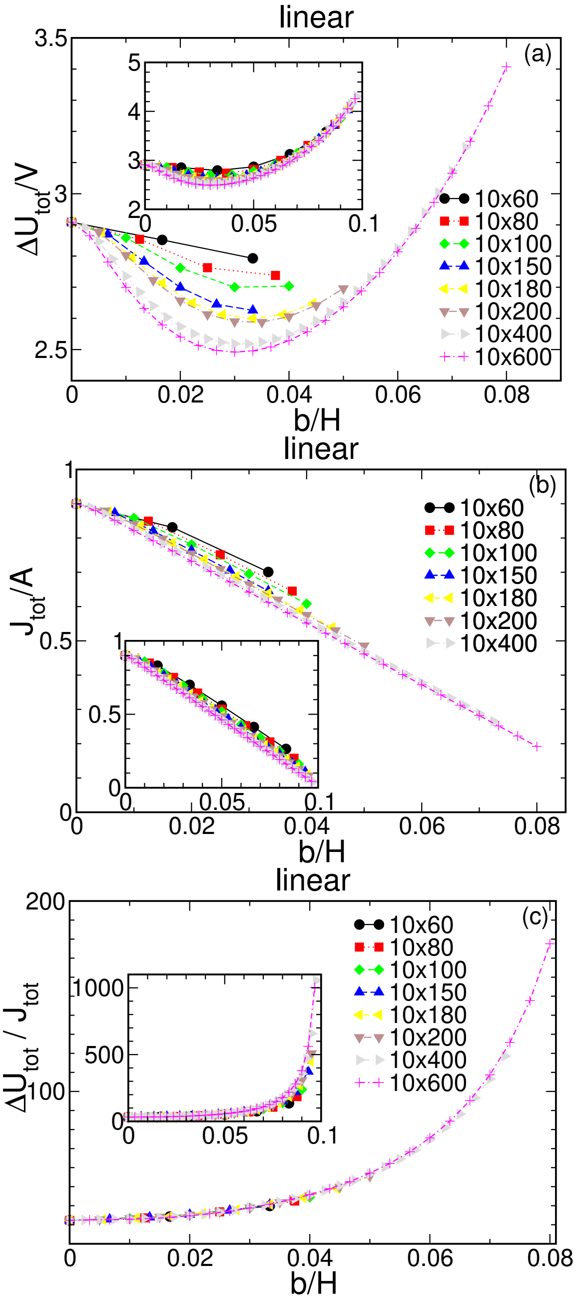

Figure 2.14: Plots of (a) total energy storage per unit volume $\Delta U_{tot}/V$, (b) total outgoing heat flow per unit area $J_{tot}/\mathcal{A}$, and (c) their ratio $\mathcal{T}_{1|2} = \Delta U_{tot}/J_{tot}$ against the normalised slope b/H of constraint type *linear*. Each panel is evaluated for six different system sizes of heights $H = 60$, 80,100, 200, 400 and 600, and a fixed-length $L = 10$.

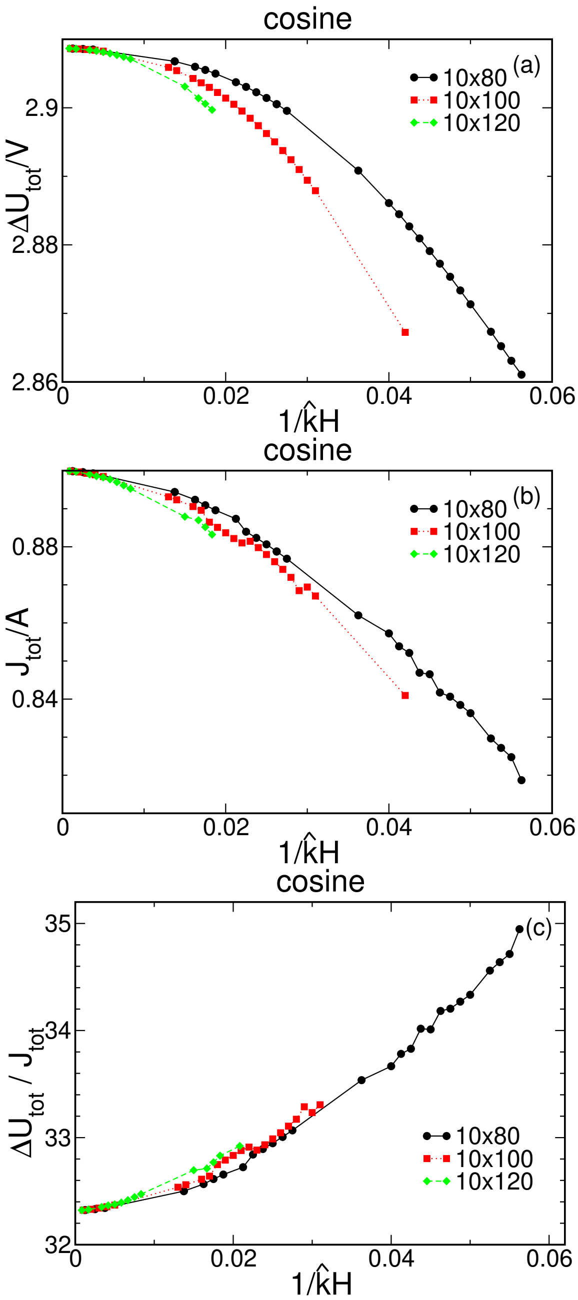

Figure 2.15: Plots of (a) total energy storage per unit volume $\Delta U_{tot}/V$, (b) total outgoing heat flow per unit area $J_{tot}/\mathcal{A}$, and (c) their ratio $\mathcal{T}_{1|2} = \Delta U_{tot}/J_{tot}$ against the scaled inverse of wavenumber $1/\hat{k}H$ of constraint type *cosine*. Each panel is evaluated for three different system sizes of heights $H = 80, 100$, and 120 and a fixed-length $L = 10$.

2.3.2 Matter Flow in Fluid: Hagen-Poiseuille Flow

We now consider the Hagen-Poiseuille flow model. This model is an extensively studied fluid model driven by matter flow [68]. Following the general settings, a fluid is placed between two parallel planar walls located at $y = \pm h$. A constant pressure gradient is applied along the x-axis, *i.e.*, $\partial_x P(x) = -\mathbb{P}$. This pressure gradient results in a constant matter flow that drives the system to nonequilibrium steady states. In addition, the fluid is assumed to be incompressible, the flow laminar. Both walls are kept at temperature T_0 and assumed to be non-slip. As the constraint, an adiabatic slip wall is introduced into the system. The constraint is placed at $y = y_1, 0 \leq y_1 \leq 1$. A scheme of the system is shown in Fig. 2.16.

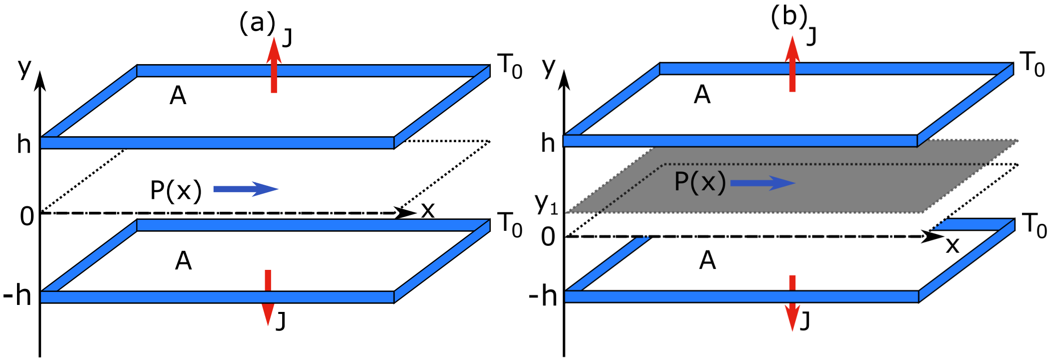

Figure 2.16: Schemes of (a) unconstrained and (b) constrained Poiseuille flow. The system is bounded by two plates of a fixed temperature T_0 and area $\mathcal{A}$, placed at $y = \pm h$. A constant pressure gradient is applied across the system. In (b), the system is divided by an adiabatic slip wall placed at $y = y_1$.

The properties of a Poiseuille flow between two parallel plates are well studied and have been derived in various textbooks [68]. Next, we will recapture the derivation of some of these quantities, which we will use to calculate the energy storage and heat flow.

We start by obtaining the velocity profile from the Navier-Stokes equation. In fluid mechanics, the central quantity is the velocity profile. The fluid flows along the x-axis and is y dependent, *i.e.*, $\vec{v} = (v(y), 0, 0)$. The Navier-Stokes equation becomes

$$\frac{\partial^2 v}{\partial y^2} = -\frac{\mathbb{P}}{\mu}, \tag{2.97}$$

where μ is the viscosity. Given the non-slip conditions at the boundaries $v(\pm h) = 0$, we find

$$v(y) = \frac{\mathbb{P}}{2\mu}(h^2 - y^2). \tag{2.98}$$

Second, with the velocity profile, we explicitly write the stress tensor and the tensor of the rate of deformation

$$\tau = \begin{pmatrix} -\mathbb{P} & \mu\frac{\partial v}{\partial y} \\ \mu\frac{\partial v}{\partial y} & -\mathbb{P} \end{pmatrix}, \quad d = \begin{pmatrix} 0 & \frac{1}{2}\frac{\partial v}{\partial y} \\ \frac{1}{2}\frac{\partial v}{\partial y} & 0 \end{pmatrix}. \tag{2.99}$$

The dissipation density function, defined as $\phi \equiv \sum_{ij} \tau_{ij}\partial_i v_j$, is obtained

$$\phi = \mu(\partial_y v)^2 = \frac{\mathbb{P}^2}{\mu} y^2. \tag{2.100}$$

This quantity governs the rate at which the mechanical energy of the flow is converted to heat. And the outgoing heat flow J_U is obtained by integrating the dissipation over the whole system,

$$J_U = \mathcal{A}\int_{-h}^{h} \phi \mathrm{d}y = V\frac{\mathbb{P}^2 h^2}{3\mu}, \tag{2.101}$$

where $\mathcal{A}$ is the area of the plates and $V = \mathcal{A} \times 2h$ is the volume of the system.

Next, we assume that the heat transfer obeys Fourier's law as usual. This links the temperature gradient to the dissipation density function,

$$-k\frac{\partial^2 T}{\partial y^2} = \phi, \tag{2.102}$$

where k is the heat conductivity like before. Together with boundary conditions $T(\pm h) = T_0$, we obtain the temperature profile,

$$T(y) = \frac{\mathbb{P}^2}{12\mu k}(h^4 - y^4) + T_0. \tag{2.103}$$

We now have all the ingredients to calculate the energy storage of the system. The total energy of the system consists of the total kinetic energy and the total internal energy. First, the total kinetic energy is given by

$$\begin{aligned} E_k &= \int_V \frac{1}{2}\rho_0 \vec{v}(\vec{r})^2 \mathrm{d}r^3 \\ &= \frac{\rho_0\mathcal{A}}{2}\int_{-h}^{h} v^2(y)\mathrm{d}y = V\frac{\rho_0\mathbb{P}^2 h^4}{15\mu^2}, \end{aligned} \tag{2.104}$$

where ρ_0 is the density at equilibrium. Next, the local internal energy density is given by $\epsilon(\vec{r}) = 3n_0 k_B T(\vec{r})/2$ with the Boltzmann constant k_B and number density n_0. This expression originates from the local form of the ideal gas law (2.10), where the number density is now a constant since the fluid is incompressible. Therefore, the total internal energy is given by,

$$\begin{aligned} E_u &= \int_V \frac{3}{2} n_0 k_B T(\vec{r}) \mathrm{d}r^3 \\ &= \frac{3}{2} \mathcal{A} n_0 k_B \int_{-h}^{h} T(y) \mathrm{d}y = V \frac{n_0 k_B \mathbb{P}^2 h^4}{10 \mu k} + \frac{3}{2} V n_0 k_B T_0, \end{aligned} \tag{2.105}$$

where the number density $n_0 = \rho_0 / m$, with m the mass of a single atom or molecule. Finally, combining Eq. (2.104), (2.105), and (2.101), we obtain

$$\mathcal{T} = \frac{\Delta U}{J_U} = \frac{E_k + E_u - E_{u_0}}{J_U} = n_0 h^2 \left(\frac{m}{5\mu} + \frac{3k_B}{10k} \right). \tag{2.106}$$

Following the same procedure, we now repeat the calculation for the system under constraint. The velocity vector for subsystem 1 and 2 is given by $(v_1(y), 0, 0)$ and $(v_2(y), 0, 0)$, respectively. Since the constraint is an adiabatic slip wall, we have additional boundary conditions

$$\begin{cases} \mathrm{d}v_1/\mathrm{d}y \,|_{y=y_1} = 0, & \mathrm{d}v_2/\mathrm{d}y \,|_{y=y_1} = 0, \\ \mathrm{d}T_1/\mathrm{d}y \,|_{y=y_1} = 0, & \mathrm{d}T_2/\mathrm{d}y \,|_{y=y_1} = 0. \end{cases} \tag{2.107}$$

Hence, the velocity profiles are obtained as

$$v_1 = \frac{\mathbb{P}}{2\mu} \left((h - y_1)^2 - (y - y_1)^2 \right), \tag{2.108}$$

$$v_2 = \frac{\mathbb{P}}{2\mu} \left((h + y_1)^2 - (y - y_1)^2 \right), \tag{2.109}$$

and the temperature profiles are

$$T_1(y) = \frac{\mathbb{P}^2}{12\mu k} \left((h - y_1)^4 - (y - y_1)^4 \right) + T_0, \tag{2.110}$$

$$T_2(y) = \frac{\mathbb{P}^2}{12\mu k} \left((h + y_1)^4 - (y - y_1)^4 \right) + T_0. \tag{2.111}$$

From these quantities, we finally obtain

$$\mathcal{T}_{1|2} \equiv \frac{\Delta(U_1 + U_2)}{J_{U_1} + J_{U_2}} = n_0 \frac{(h - y_1)^5 + (h + y_1)^5}{(h - y_1)^3 + (h + y_1)^3} \left(\frac{m}{5\mu} + \frac{3k_B}{10k} \right). \tag{2.112}$$

Comparing $\mathcal{T}$ (2.106) and $\mathcal{T}_{1|2}$ (2.112), the comparison reduces to

$$h^2 \text{ and } \frac{\left((h - y_1)^5 + (h + y_1)^5 \right)}{\left((h - y_1)^3 + (h + y_1)^3 \right)}. \tag{2.113}$$

Since the position of the constraint $y_1 \in (-h, h)$, the denominator is positive, $(h - y_1)^3 +$

$(h+y_1)^3 \geq 0$. If we move this denominator to the left hand side, divide both sides with h^5 and rearrange terms, we retrieve

$$0 \text{ and } f(\delta) \equiv (1+\delta)^5 + (1-\delta)^5 - (1+\delta)^3 - (1-\delta)^3. \tag{2.114}$$

Taking derivative with respect to δ, we find $f'(\delta) \geq 0$ and thus $f(\delta) \geq f(0) = 0$. Therefore, we have shown that $\mathcal{T} \leq \mathcal{T}_{1|2}$. The result agrees with Hypothesis 2.1.1.

2.3.3 Rayleigh-Bénard Convection

Additionally, Hypothesis 2.1.1 is tested numerically in a two-dimensional Rayleigh-Bénard system consisting of hard disks. As stated previously, the simulation results in this section are reproduced from paper [1], performed by the group of Prof. Banaszak and not the author.

Generally, a Rayleigh-Bénard system is a fluid system subjected to both an upward heat flow and gravitation. The system is placed between two heat conducting plates. The upper plate is kept at temperature T_0 and the lower plate is heated to $T = T^*T_0$, where T^* is the dimensionless temperature and $T^* \geq 1$. At low temperature gradient, the system reaches a conductive steady state. As the temperature gradient increases, the system transit into a convective steady state. A scheme of the system is shown in Fig. 2.17. An example of the typical conductive state and convective state can be found in Fig. 2.18 (b) and (c), where the velocity fields are plotted.

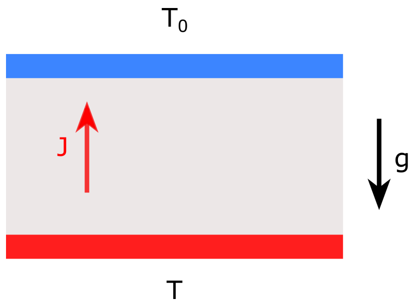

Figure 2.17: Scheme of Rayleigh-Bénard system. A fluid system is placed between two heat conducting plates: the bottom plate at temperature T, the top plate at T_0, and $T \geq T_0$. An energy flow J and a gravitational field g are present in the system.

For the simulation system in [1], the transition temperature is $T^*_{RB} \approx 15.5$. It is observed that, by inserting an internal constraint (adiabatic wall) into the middle of the system in an otherwise convective state, the system can be stabilized in the conductive state, up till a relatively high temperature gradient. In other words, an internal wall may stabilize the conductive state above the transition to the convective state. Furthermore, upon removing this constraint at $T^* > T^*_{RB}$, the two independent conductive states combine into a single convective state. This removal does not change the total energy storage nor the total heat flow. This is indicated in Fig. 2.18 (b) and (c), where these two systems are under the same temperature gradient, and the insertion of the internal wall in (b) prevents the system from becoming convective.

This system can be used to test Hypothesis 2.1.1 using the second method described in Sec. 2.1. Specifically, $\mathcal{T}$ is measured for both steady states: $\mathcal{T}_{\text{unconstrained}}$ for steady states of the system without constraint, which is in conductive states at $T^* < T^*_{RB}$ and convective states otherwise; $\mathcal{T}_{\text{constrained}}$ for steady states of the system with an internal wall inserted in the middle, which is in conductive states at all measured temperatures. Results of this comparison are shown in Fig. 2.18 (a). As we can see, results show that $\mathcal{T}_{\text{constrained}} \geq \mathcal{T}_{\text{unconstrained}}$, suggesting that the convective state is more stable, which is in accordance with observations. Hence, this result supports the hypothesis.

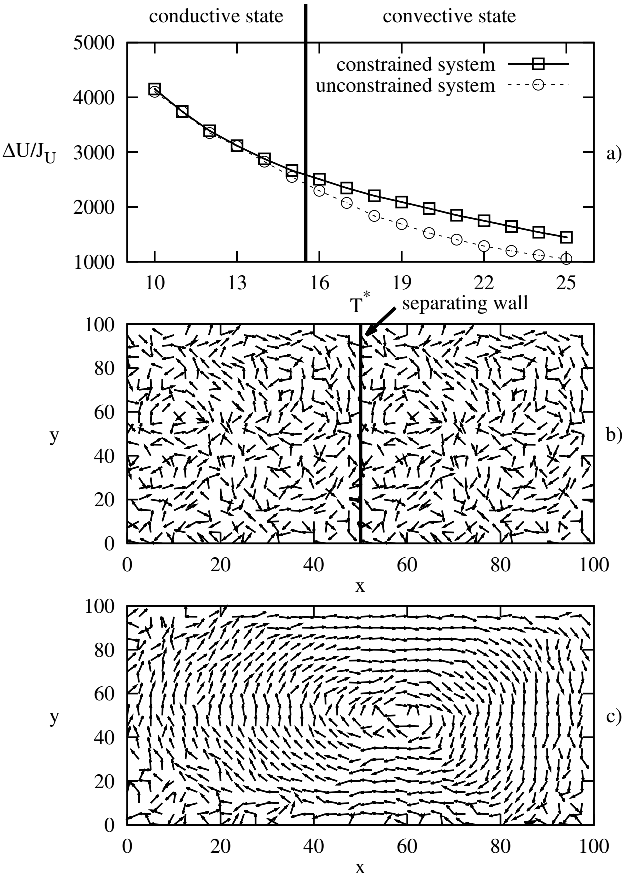

Figure 2.18: (a) $\mathcal{T} = \Delta U / J_U$ as a function of the (normalised) lower plate temperature T^* of a two-dimensional Rayleigh-Bénard system. The vertical solid line remarks the transition point around $T^* = T^*_{RB} = 15.5$. Open circles denote the MD results of the unconstrained system which is in the conductive state for $T^* < T^*_{RB}$ and the convective state for $T^* > T^*_{RB}$. Open squares denote the MD results of the constrained system which is in the conductive state at all simulated temperatures. (b) Example of the steady state velocity field in the conductive state (constrained state). (c) Example of the steady state velocity field in the convective state, stable for $T^* > T^*_{RB}$. Both (b) and (c) are at $T^* = 17$. Reproduced from [1].

Simulation Methods

This simulation is performed using *event-driven dynamics*, a method of molecular dynamics (MD). In this particular dynamics, the system is updated when an event (collision) occurs. Collisions between disks and a disk with the left and right boundary are elastic, whereas collisions with the upper and lower plates transfer thermal energy to the system. In the latter scenario, the velocity of the disk is discarded and reassigned randomly according to the appropriate Maxwell distribution, and the direction is chosen randomly between $\measuredangle = (0, 180)$ with respect to the plate [64].

Details of the simulation parameters are as follows. The system consists of N hard disks with diameter r_0 and mass m, where $N = 10,000$. The system is rectangular of size $L_x \times L_y = 100 \times 100$. All distances are measured in units of $r_0/\sqrt{0.4}$. Under these parameters, the system has a density of $\rho^* = 0.4$. Moreover, all disks were subjected to a gravitational field with strength $g^* = gmL_y r_0/(k_B T) = 0.15$.

The length of the simulation is naturally measured in the number of collisions n_c. The system equilibrate under $n_c = 9 \times 10^8$ collisions, and results are obtained for another $n_c = 9 \times 10^8$ collisions. It can also be measured using the dimensionless time, $t^* = t/t_0$, where $t_0 = \sqrt{mr_0^2/(k_B T)}$. In the case of system size 100×100, this corresponds to a duration of $t^* = 1.35 \times 10^4$ for $T^* = 10$, and $t^* = 1.1 \times 10^4$ for $T^* = 25$.

The total energy of the system is measured with,

$$U_{tot} = \sum_{i=1}^{N} \frac{mv_i^2}{2} + \sum_{i=1}^{N} mgy_i, \tag{2.115}$$

where v_i is the velocity and y_i is the y-coordinate of the i^{th} disk. The equilibrium energy U_{eq} is set as the averaged system energy at $T^* = 1$. All energies are represented in units of $k_B T$. On the other hand, the energy flow is calculated through

$$J_{\text{upper}} = \frac{1}{t} \sum_{\alpha=1}^{n_{c,\text{upper}}} E_\alpha, \tag{2.116}$$

$$J_{\text{lower}} = \frac{1}{t} \sum_{\alpha=1}^{n_{c,\text{lower}}} E_\alpha, \tag{2.117}$$

where $E_\alpha = (mv_{i,\alpha^+}^2 - mv_{i,\alpha^-}^2)/2$ is the energy transfer under collision event α of disk i, during which the velocity changes from v_{i,α^+} to v_{i,α^-}. The summation runs over all collision events with either plate, *upper* or *lower*. As discussed before, in steady states, $J_{\text{upper}} = -J_{\text{lower}}$, and the lower plate is chosen to calculate the heat flow. The heat flow results are represented in units of $k_B T/t_0$.

2.4 Energy Storage in Periodic Steady States

In previous sections 2.2 and 2.3, we have studied various models subjected to bulk energy supplies and through external energy flows. These systems are driven to nonequilibrium steady states.

In this section, we compile models under external drivings that are periodic in time and spatially inhomogeneous. We refer to these driving protocols as the local periodic energy supply. Furthermore, the underlying system is a lattice system, or more precisely, a two-dimensional Ising system. These models eventually reach periodic steady states. A periodic steady state is a nonequilibrium state where the properties of the system vary over a period, but their averaged values over this period are constant.

We perform numerical simulations using a combination of the Metropolis algorithm [69] and the *deterministic Ising algorithm* [70–72]. This combination gives us the freedom to supply energy locally, as well as define and measure temperatures locally. This method is different from what is often used for nonequilibrium lattice simulations.

This section is organized as follows. We first give an introduction to the algorithms we use. Next, we describe our model in Sec. 2.4.2. Details of the simulation procedure are outlined in Sec. 2.4.3. We summarize our results in Sec. 2.4.4.

2.4.1 Introduction

2.4.1.1 Lattice Models and Nonequilibrium Simulations

Lattice models are substantial to the study of statistical physics, equilibrium and nonequilibrium. The lattice models have been investigated both analytically and numerically. The energy states of a lattice model are naturally discrete, making the stochastic Markov processes easy to realise. These models are widely used as testing grounds for statistical physics [10, 69, 73–76].

Perhaps the simplest example of a lattice model is the Ising model, which is also the base system we use in this section. An Ising model is a set of spins arranged in a lattice. The spins are with magnetic dipole moments of ± 1, where $+1(-1)$ represents the spins pointing up(down). Each spin interacts with its nearest neighbours with strength J. Additional external magnetic fields B can be added to the system. The Hamiltonian of the system is given by

$$H = -J \sum_{\langle ij \rangle} s_i s_j - B \sum_i s_i, \tag{2.118}$$

where s_i is the spin value at site i, $\langle \cdot\cdot \rangle$ represent the pairs of neighboring sites. Despite its simplicity, the Ising model captures the essential features of phase transition. In equilibrium statistical physics, the Ising model is the paradigm model for studying phase transitions, critical phenomena, and universality classes.

Another important example of the lattice model is the driven lattice gas model. It is the paradigm model for studying nonequilibrium phenomena [10, 73, 76, 77]. Models built on the driven lattice gas model include the *asymmetric simple exclusion process* (ASEP), the *total asymmetric simple exclusion process* (TASEP), and their variations. With relatively simple rules, these models can already demonstrate complex nonequilibrium phenomena, such as spontaneous symmetry breaking, nonequilibirum phase separation and current fluctuations [40, 78–80]. External drivings can be achieved, for example, by attaching two reservoirs that induce transport of energy or particles through the system, or by assigning a biased transition rate in the preferable direction [10].

The author would like to point out that, in these models, it is often assumed that the temperature is homogeneous, and the external drives are uniformly applied. In contrast, similar to the other models in previous sections, our models have inhomogeneous temperature profiles, and the external drives can be locally applied.

2.4.1.2 Monte Carlo Method

The Monte Carlo (MC) method is a simulation technique that utilises statistical sampling to generate results. Ever since its devise in the 1940s, it has been used to explore a wide range of phenomena in equilibrium and nonequilibrium statistical physics. Usually, a sampling is drawn from a predetermined probability distribution, by generating a stochastic Markov chain [69, 74, 75]. Some examples of the problems that can be solved by the MC method are diffusion problems such as Brownian motion, phase transition problems, e.g., for a binary mixture, a surface growth, and much more.

As discussed in Chapter 1, in equilibrium statistical mechanics, the probability distribution over the phase space is well established: for the canonical ensemble, it is the Boltzmann distribution; for the microcanonical ensemble, the uniform distribution. A set of states are generated using a Markov chain with properly chosen transition probabilities ω_{mn} of all possible pairs of states m to n. To ensure that at sufficiently long time the system eventually settles in the equilibrium state with the Boltzmann distribution, the transition probabilities are chosen in accordance with the detailed balance relation,

$$\frac{\omega_{mn}}{\omega_{nm}} = \frac{p_n}{p_m} = e^{-\beta(E_n - E_m)}, \tag{2.119}$$

where $E_n(E_m)$ is the energy of state $n(m)$.

In practice, a Markov chain is formed by a series of transition steps, each broken down into two smaller steps, a generating step with probability $g(m \to n)$ and an acceptance step with probability $A(m \to n)$. Their relationships can be represented by [69]

$$\omega_{mn} = g(m \to n)A(m \to n). \tag{2.120}$$

In each step, given that the current state of the system as m, a new state n is first chosen with the selecting probability $g(m \to n)$. The new state can be accepted or rejected depending on $A(m \to n)$. If the state is accepted, then the system moves to the new state n; otherwise, the system stays in state m. This step repeats to generate a series of states.

For example, in the Metropolis algorithm [81], all possible states are chosen with equal probability, *i.e.*, $g(m \to n) = 1/N$. Then, the acceptance probabilities $A(m \to n)$ must satisfy [69]

$$\frac{A(m \to n)}{A(m \to n)} = e^{-\beta(E_n - E_m)}. \tag{2.121}$$

In the Metropolis algorithm, the acceptance probabilities are chosen as

$$A(m \to n) = \begin{cases} e^{-\beta(E_n - E_m)} & \textit{if } E_n - E_m > 0, \\ 1 & \textit{otherwise.} \end{cases} \tag{2.122}$$

In other words, if the new state decreases in energy, then the move is always accepted; if the new state has a higher energy, then the move is accepted with a probability of $e^{-\beta(E_n - E_m)} \in (0, 1)$. Note that in principle, one has the freedom to choose any values of $g(m \to n)$ and $A(m \to n)$ between 0 and 1 (without violating relation (2.119)). However, it is desirable to have $A(m \to n)$ as close to 1 as possible. In this case, the algorithm moves efficiently in phase space without dwelling in the same state for a long time.

In nonequilibrium systems, the detailed balance is broken, and external currents are present. In simulations, this can be achieved by modifying the transition rates to account for the external driving mechanism.

As an example, we briefly describe the driven lattice gas model. A lattice gas model is a model of gas where the particles are moving on lattice sites. The model can be simulated using the Ising model with the restriction that the order parameter is conserved. The up (down) spins now represent the occupied (vacant) sites. Since it is a gas model, the total number of particles, or the order parameter of the Ising model, needs to be conserved. Thus, instead of the spin-flip algorithm, the spins are exchanged using the Kawasaki algorithm.

There are several ways to modify the transition rates. In the simplest case, the transition rate $\omega_{mn} (\omega_{nm})$ is simply assigned to be $p(1-p)$. This is used in the one-dimensional biased random walk, in AESP and the TAESP. Alternatively, the transition rates can be modified to include an external driving field $\vec{E}$. The particle movements are biased along and against the field direction, but not on the orthogonal directions. In which case,

$$\omega_{mn} = \begin{cases} e^{-\beta \Delta E}, \text{ moves orthogonal to } \vec{E} \\ e^{-\beta(\Delta E \pm |\vec{E}|)}, \text{ moves along or against } \vec{E}. \end{cases} \tag{2.123}$$

where ΔE denotes the energy difference $E_n - E_m$, and $|\vec{E}|$ is the strength of the field. In this expression, the local detailed balance is preserved.

2.4.1.3 Deterministic Ising Algorithm

In a Monte Carlo simulation, the temperature is a parameter already set in the algorithm and is assumed homogeneous. In contrast, a molecular dynamics simulation is a deterministic simulation where no random number is involved. Moreover, the temperature is not predetermined but rather obtained as a result of the simulation.

The deterministic algorithm proposed by Creutz in 1985 is an algorithm between the Monte Carlo algorithm and the molecular dynamics algorithm (see [70] and [71, 72]). In this algorithm, the total energy is conserved like in a molecular dynamics simulation. A definition of the local temperature is provided along with the algorithm, and the local temperature can be measured. Since the algorithm is over an Ising model, the local temperature is measured (instead of preset) at each lattice point. This algorithm has been shown to behave in almost the same way as the Monte Carlo simulation of the original Ising model [82].

In the deterministic Ising algorithm, an extra variable $D(\vec{r})$ is associated to each spin $s(\vec{r})$ at position (lattice site) $\vec{r}$ [70]. This variable $D(\vec{r})$ serves as the momentum variable partner of $s(\vec{r})$. Alternatively, $D(\vec{r})$ can be interpreted as a local heat bath of only one degree of freedom. Assuming that the energy exchange between $s(\vec{r})$ and $D(\vec{r})$ is fast, the spin is in equilibrium with $D(\vec{r})$. Therefore, there is a relationship between the averaged momentum energy and the local temperature $T(\vec{r})$, given by

$$\langle D(\vec{r})\rangle \equiv \frac{\sum_0^\infty n\exp(-n/T(\vec{r}))}{\sum_0^\infty \exp(-n/T(\vec{r}))} = \frac{1}{\exp(1/T(\vec{r}))-1}, \tag{2.124}$$

where $\langle\cdot\rangle$ is the ensemble average, $n = 0, 1, 2, \cdots$. Eq. (2.124) can be rewritten to obtain the local temperature

$$T(\vec{r}) = \frac{1}{\ln(1/\langle D(\vec{r})\rangle + 1)}. \tag{2.125}$$

A discussion of the definition of temperature in nonequilibrium systems can be found in [83]. Here in this section, we consider only the temperature defined in the sense of the deterministic algorithm.

The system evolves according to the deterministic dynamics, where the local energy is preserved. The local Hamiltonian at time t is given by

$$\mathcal{H}(t) = -Js(\vec{r},t)\sum_{\vec{r}'} s(\vec{r}',t) + D(\vec{r},t), \tag{2.126}$$

where $\vec{r}'$ represents the nearest neighbors of the lattice site $\vec{r}$. For $\vec{r} = (x, y)$, $\vec{r}' \in \{(x, y \pm 1), (x \pm 1, y)\}$. To update a spin $s(\vec{r},t)$, we first calculate the local energy difference under the spin-flip with

$$\Delta E = 2Js(\vec{r},t)\sum_{\vec{r}'} s(\vec{r}',t). \tag{2.127}$$

The update (spin-flip) is always accepted if the flip lowers the local energy $\Delta E \leq 0$. In

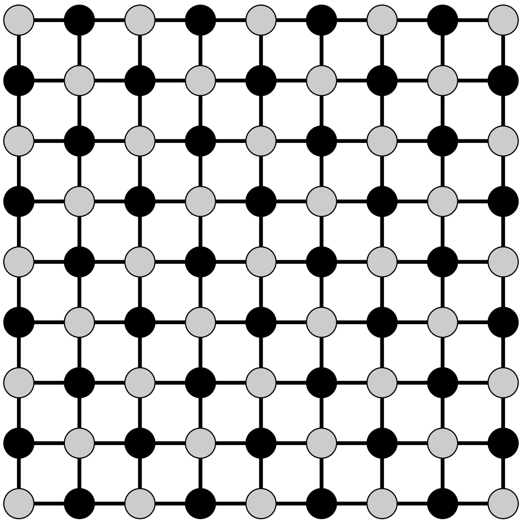

Figure 2.19: Scheme of the check-board update method. Each time step is broken down into two smaller steps. Starting from time t, firstly, all grey (or black) spins are updated at time $t + 1/2$. Then at time step $t + 1$, all black (or grey) spins are updated.

the case where the update costs energy $\Delta E > 0$, the update is also accepted, provided that the momentum counterpart $D(\vec{r}, t)$ can compensate the energy for this update, that is, if $D(\vec{r}, t) - \Delta E \geq 0$. Then, both the spin and its momentum variable are updated, $s(\vec{r}, t+1) = -s(\vec{r}, t), D(\vec{r}, t+1) = D(\vec{r}, t) - \Delta E$. Otherwise, this update is rejected and $s(\vec{r}, t+1) = s(\vec{r}, t), D(\vec{r}, t+1) = D(\vec{r}, t)$. This update method ensures that the local Hamiltonian is conserved $\mathcal{H}(t) = \mathcal{H}(t+1)$.

The whole lattice evolves from t to $t+1$ when each spin is updated accordingly. Additional consideration needs to be taken to ensure that the update of the whole lattice is simultaneous. If one updates sequentially, one would encounter a situation when updating a spin to time $t+1$, its neighbours are in a mixture of t and $t+1$. To avoid this situation, a check-board update scheme is adopted [84]. In a check-board update, the system is divided into two groups organized in a check-board manner. An example of this update is shown in Fig. (2.19) where the two groups of spins are represented in grey and black. At time t, firstly, all grey (or black) spins are updated, then all black (or grey) spins are updated.

The deterministic Ising algorithm has been used to study heat diffusion in an Ising system, since the temperature profile is obtained *a posteriori*. Previously, this algorithm has also been used, among other purposes, to simulate the electrocaloric effect in alloys [85] and to study dynamics of discrete systems with long-range interactions [86] or thermoconductivity in lattice systems without [87–91] and with an interface [92, 93], where the lattice is typically attached to two heat baths at different temperatures.

2.4.2 Model Description

Consider a two-dimensional closed Ising system embedded in a heat bath of temperature T_0. The system is of dimensions $L \times L$. The system is driven to nonequilibrium states with local periodic energy supplies $\sigma_E(\vec{r}, t)$. The energy is dissipated through the boundary, and the heat current is denoted by $\vec{J}_E(\vec{r})$. A scheme of the system is shown in Fig. 2.20.

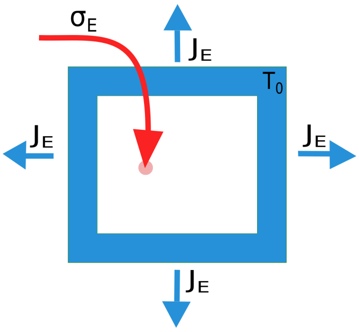

Figure 2.20: Scheme of an unconstrained system. A two-dimensional closed lattice system, denoted in white, is surrounded by a heat bath of temperature T_0. External energy σ_E is supplied into the system. Energy currents are denoted as $\vec{J}_E$.

Similar to the situation of previous models, the temperature is not homogeneous inside the system. Comparing to local excitation, heat dissipation is a slow process. We can imagine an excitation that happens deep inside the system would take longer to dissipate than an excitation close to the boundary.

Since the system does not perform work, the total heat flux can be calculated either from the energy dissipated (per time) across the boundary, or from the total energy supplied (per time) into the system (see Eq. (2.14), (2.15) and (2.16)). Unlike the ideal gas situation, an Ising model is discrete in space, and the spins are fixed at lattice sites. We can no longer assume that the local energy density is homogeneous, and in general $\epsilon = \epsilon(\vec{r})$. Moreover, the total heat flux J_U needs to be rewritten as

$$J_U \equiv \sum_{\vec{r} \in \partial\Omega} \vec{J}_E(\vec{r}) = \sum_{\vec{r} \in \Omega} \sigma_E(\vec{r}), \tag{2.128}$$

where Ω is the area of the system, and $\partial\Omega$ is the boundary of the system. In this case, it is also the boundary through which the energy is dissipated.

The external energy supply is periodic and inhomogeneous. Under such protocols, the system reaches a periodic steady state. In experiments, such excitations can be realized by shining a laser onto a material or a solution.

We define different protocols by specifying the energy supply function $\sigma_E(\vec{r}, t)$. We focus on a periodic supply with period τ. Periodic external drives occur in many situations in physics and biology [94–96]. The system reaches periodic steady states where quantities averaged through a period remain constants [95, 96]. Examples of periodic steady states driven by external magnetic fields can be found in [97].

In these states, instead of quantity $O(t)$, its corresponding average over one or several periods $\overline{O}$ is evaluated. Therefore, we will be using the averages of the quantities we previously studied. First, we define the averaged temperature profile as

$$\overline{T}(\vec{r},\tau) \equiv \frac{1}{\tau}\int_{t'}^{t'+\tau} T(\vec{r},t)\mathrm{d}t. \tag{2.129}$$

The averaged external energy flow at $\vec{r}$ is

$$\overline{\sigma_E}(\vec{r},\tau) \equiv \frac{1}{\tau}\int_{t'}^{t'+\tau} \sigma_E(\vec{r},t)\mathrm{d}t, \tag{2.130}$$

and the averaged total heat flow is

$$\overline{J_U} \equiv \frac{1}{\tau}\int_{t'}^{t'+\tau} J_U\mathrm{d}t. \tag{2.131}$$

And we define the averaged system energy as

$$\overline{U}_{\mathrm{sys}}(\tau) \equiv \frac{1}{\tau}\int_{t'}^{t'+\tau} U(t)\mathrm{d}t, \tag{2.132}$$

with the (averaged) stored energy

$$\Delta U(\tau) = \overline{U}_{\mathrm{sys}}(\tau) - U_{eq}. \tag{2.133}$$

2.4.3 Simulation Method

2.4.3.1 Update Procedure

In our simulation, we combine the Metropolis algorithm for exchanging energy with the heat bath [69] and the deterministic Ising algorithm for energy supply and internal energy diffusion [70]. The spins are separated into two categories, two layers of spins that serve as the heat bath (heat bath spins) surround spins that serve as the system (system spins). For an open system of size $L \times L$, we use $(L+4) \times (L+4)$ number of spins in the simulation. The heat bath spins are with index $x, y = 0, 1, L+2, L+3$. They are updated using the Monte Carlo Metropolis algorithm. The rest are the system spins and are updated with the deterministic Ising algorithm. A scheme of this spin arrangement is shown in Fig. 2.21.

This set-up is similar to the set-up in [87], except that our system is an open system. Additionally, the Ising lattice system under the local energy input has been studied in [98]. However, in that paper, the focus was on the nonequilibrium phase diagram, and the energy input was realized by dividing the system into two sectors in contact with thermal baths with markedly different temperatures.

The full procedure of a Monte Carlo step of the system $\{s(\vec{r},t)\}$ to $\{s(\vec{r},t+1)\}$ is as follows. First, we update all the heat bath spins using the Metropolis dynamics. The

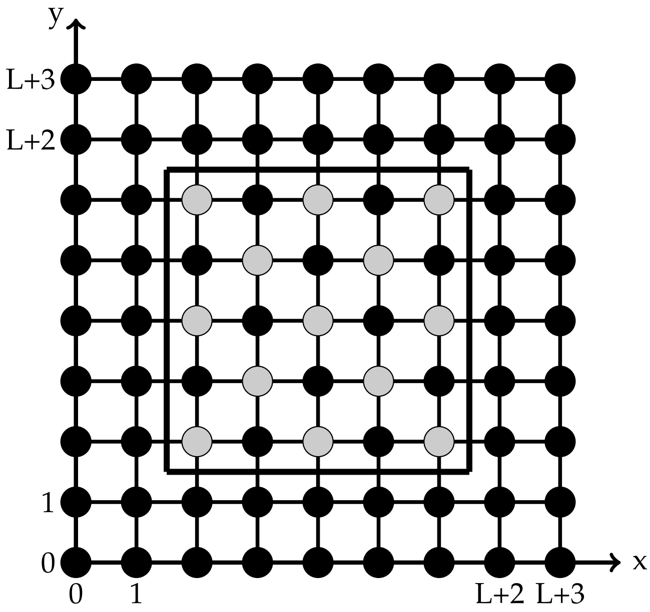

Figure 2.21: Scheme of the check-board update of the lattice system. The system of interest is inside the black lines and surrounded by two layers of spins representing the heat bath. Black and grey dots of the system denote the two groups of spins during the check-board update. For a system of size $L \times L$, x and y range from 0 to $L + 3$.

spins are selected sequentially. After a spin is selected, for example $s(\vec{r}, t), \vec{r} \in \partial\Omega$, a random number $\gamma \in (0, 1)$ is generated. The local energy difference under the spin-flip is calculated using Eq. (2.127). If $\Delta E \leq 0$, or if $\gamma \leq \exp(-\Delta E / T_0)$, then the spin is flipped $s(\vec{r}, t + 1) = -s(\vec{r}, t)$. Otherwise, $s(\vec{r}, t)$ remains the same.

Next, we update system spins using the deterministic Ising algorithm. The system spins are divided into two groups (as shown in Fig. 2.21), organized in a check-board manner. Each time step is composed of two half-steps where the spins in each group are updated. Local energy is conserved under this update. Heat is transferred through spin-spin interactions.

2.4.3.2 Energy Supply Realization

Local energy supply is realized by directly elevating the momentum energy $D(\vec{r}, t)$ with the driving protocol $\sigma_E(\vec{r}, t)$,

$$D(\vec{r}, t + 1) = D(\vec{r}, t) + \sigma_E(\vec{r}, t). \tag{2.134}$$

The explicit form of $\sigma_E(\vec{r}, t)$ is defined as

$$\sigma_E(\vec{r}, t) = E_0 h(t) X_{A_i}(\vec{r}), \tag{2.135}$$

where E_0 is the amplitude, and $h(t)$ is a periodic function $h(t) = h(t + \tau)$. The simplest case of a periodic supply is to supply every τ time unit (Monte Carlo steps). This can be represented using the delta function, $h(t) = \delta(t, n\tau)$, where $n = 1, 2, 3, \cdots$. $X_{A_i}(\vec{r})$ is an indicator function that has value 1 at the lattice sites where energy is supplied. In this section, we use three types of geometry $A_{1,2,3}$ (shown in Fig. 2.22). Specifically, A_1 covers the whole system, hence a homogeneous input; A_2 is a square of size 10×10 at the center of the system; A_3 is a stripe of size $L \times 4$ in the middle of the system. These geometries can be represented as follow

$$\begin{aligned}
&\text{case 1} \quad A_1 = \{\vec{r} | \forall \vec{r}\}, N_1 = L^2 \\
&\text{case 2} \quad A_2 = \{\vec{r} | L/2 - 4 \leq x \leq L/2 + 5, L/2 - 4 \leq y \leq L/2 + 5\}, N_2 = 100 \\
&\text{case 3} \quad A_3 = \{\vec{r} | L/2 - 1 \leq y \leq L/2 + 2\}, N_3 = 4L.
\end{aligned} \tag{2.136}$$

where N_i is the number of spins (or area) in geometry A_i, $i = 1, 2, 3$.

Using definitions from Eqs. (2.128) and (2.131), we represent the energy input protocol of geometry A_i as $J_U(A_i, E_0, \tau)$ and the averaged flux is

$$\overline{J_U}(N_i, E_0, \tau) = \frac{E_0}{\tau} N_i. \tag{2.137}$$

The averaged flux through the system depends on three variables, energy amplitude, the period, and the area of the geometry.

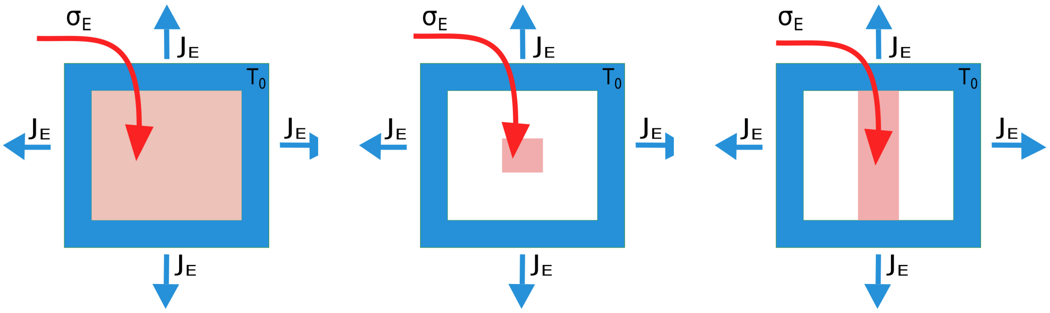

(a) A_1 (b) A_2 (c) A_3

Figure 2.22: Schemes of the three geometries $A_{1,2,3}$ used for energy supply. The region of energy supply of each geometry is shaded in red. $(a) A_1$ spans the whole system. $(b) A_2$ is a square of size 10×10 at the center of the system. $(c) A_3$ is a stripe of size $L \times 4$ in the middle of the system.

2.4.3.3 Measurement

The total energy of the system is defined as

$$U_{\text{sys}}(t) = -J \sum_{\langle \vec{r}, \vec{r}' \rangle} s(\vec{r}, t) s(\vec{r}', t) + \sum_{\vec{r}} D(\vec{r}, t), \tag{2.138}$$

where $\langle \vec{r}, \vec{r}' \rangle$ are neighboring lattice sites. The interaction strength J is set to 1. Note that, in simulation, the system energy includes its interaction energy with the heat bath spins. In other words, while $\vec{r} \in \Omega$, $\vec{r'}$ includes spins representing the first layer of the heat bath.

In steady states, the temperature profile is measured using Eq. (2.125). In simulation, the ensemble average is obtained through averaging over realizations

$$\langle D(\vec{r},t)\rangle = \frac{1}{N}\sum_{M=1}^{N} D_M(\vec{r},t), \tag{2.139}$$

where $D_M(\vec{r},t)$ is the local momentum energy at time t from realization M, and N denotes the total number of realizations. Typically in our simulation, N ranges from 100 to 500. For periodic steady states, we obtain the averaged local momentum energy as

$$\overline{D}(\vec{r},\tau) \equiv \frac{1}{\tau}\sum_{t'=t}^{t+\tau}\langle D(\vec{r},t')\rangle = \frac{1}{N\tau}\sum_{t'=t}^{t+\tau}\sum_{M=1}^{N} D_M(\vec{r},t'). \tag{2.140}$$

The averaged temperature profile $\overline{T}(\vec{r},\tau)$ is obtained through

$$\overline{T}(\vec{r},\tau) = \frac{1}{\ln\left(1/\overline{D}(\vec{r},\tau)+1\right)}. \tag{2.141}$$

Within each period, the temperature profile changes with time. An example of how the temperature profile relaxes within a period in such periodic steady states is shown in Fig. 2.23. Under adiabatic conditions (no energy flows outside the system) and using geometry A_3, we supply energy at time 0 with $E_0 = 100$. We average $T(\vec{r},t)$ over each column and every 200 MC simulation steps. Throughout the simulation, the temperature is measured in units of J/k_B. As we can see, this average relaxes and tends to equilibrate within the system.

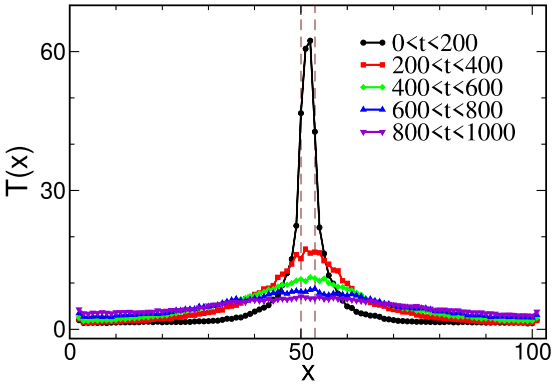

Figure 2.23: Averaged column temperature profiles under energy supply protocol $J_U(A_3, 100, 1000)$: energy supply of amplitude 100, period 1000 MC steps, and over geometry A_3. The whole period is divided into time intervals of 200 MC steps over which the temperature profiles are averaged. The x-coordinate of the stripe subjected to the energy supply lies between two vertical dashed lines. Temperatures are measured in units of J/k_B and energy in units of J.

2.4.4 Simulation Results

2.4.4.1 Energy Storage

First, we compute the stored energy under different protocols. Upon fixing the geometry A_i and the amount of total flux $\overline{J_U}$, we compare the stored energy ΔU under different pairs of (E_0, τ). A summary of the protocols we use in this section is shown in Table 2.3. The protocols are controlled by three parameters in the expression of σ_E in (2.135): A_i as shown in Fig. 2.22, E_0, and τ. Under each geometry, the pairs of E_0 and τ are chosen such that $\overline{J_U}$ stays the same, see Eq. (2.137).

Ising Model		
$A_1(E_0, \tau)$	$A_2(E_0, \tau)$	$A_3(E_0, \tau)$
$(20, 10000)$	$(100, 2000)$	$(100, 2000)$
$(40, 20000)$	$(200, 4000)$	$(200, 4000)$
$(60, 30000)$	$(400, 8000)$	$(400, 8000)$
$(80, 40000)$	$(500, 10000)$	$(500, 10000)$
$(100, 50000)$	$(800, 16000)$	$(800, 16000)$
		$(1000, 20000)$

Table 2.3: List of energy supply protocols used for simulation. Each protocol is specified by: amplitude E_0, period τ, and geometry A_i as in Fig. 2.22.

Examples of contour plots of the averaged temperature profile $\overline{T}(\vec{r}, \tau)$ under different geometries are shown in Fig. 2.24. For easier demonstration, we further define an averaged column temperature

$$\overline{T}(x, \tau) \equiv \sum_y \overline{T}(x, y, \tau)/L. \tag{2.142}$$

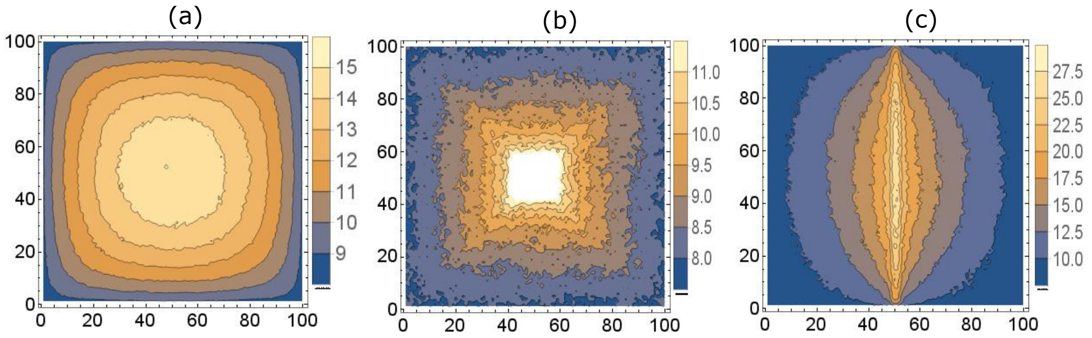

$\overline{J_U}(A_1, 20, 10000)/L^2 = 0.002$ $\overline{J_U}(A_2, 100, 2000)/L^2 = 0.0005$ $\overline{J_U}(A_3, 100, 2000)/L^2 = 0.002$

Figure 2.24: Contour plots of averaged temperature profiles $\overline{T}(\vec{r}, \tau)$ under different energy supply geometries shown in Fig. 2.22. Corresponding protocols and averaged fluxes for energy supply are denoted under each graph. Temperature is measured in units of J/k_B. The white area in the center of (b) denotes temperature higher than the shown scale.

Results of $\overline{T}(x, \tau)$ are shown in Fig. 2.25(a), 2.25(c), and 2.25(e). Each panel shows the results of the column temperature from a single geometry. Different curves in each panel correspond to the protocols in the columns of Table 2.3. The stored energy ΔU for each geometry are shown in Fig. 2.25(b), 2.25(d), and 2.25(f).

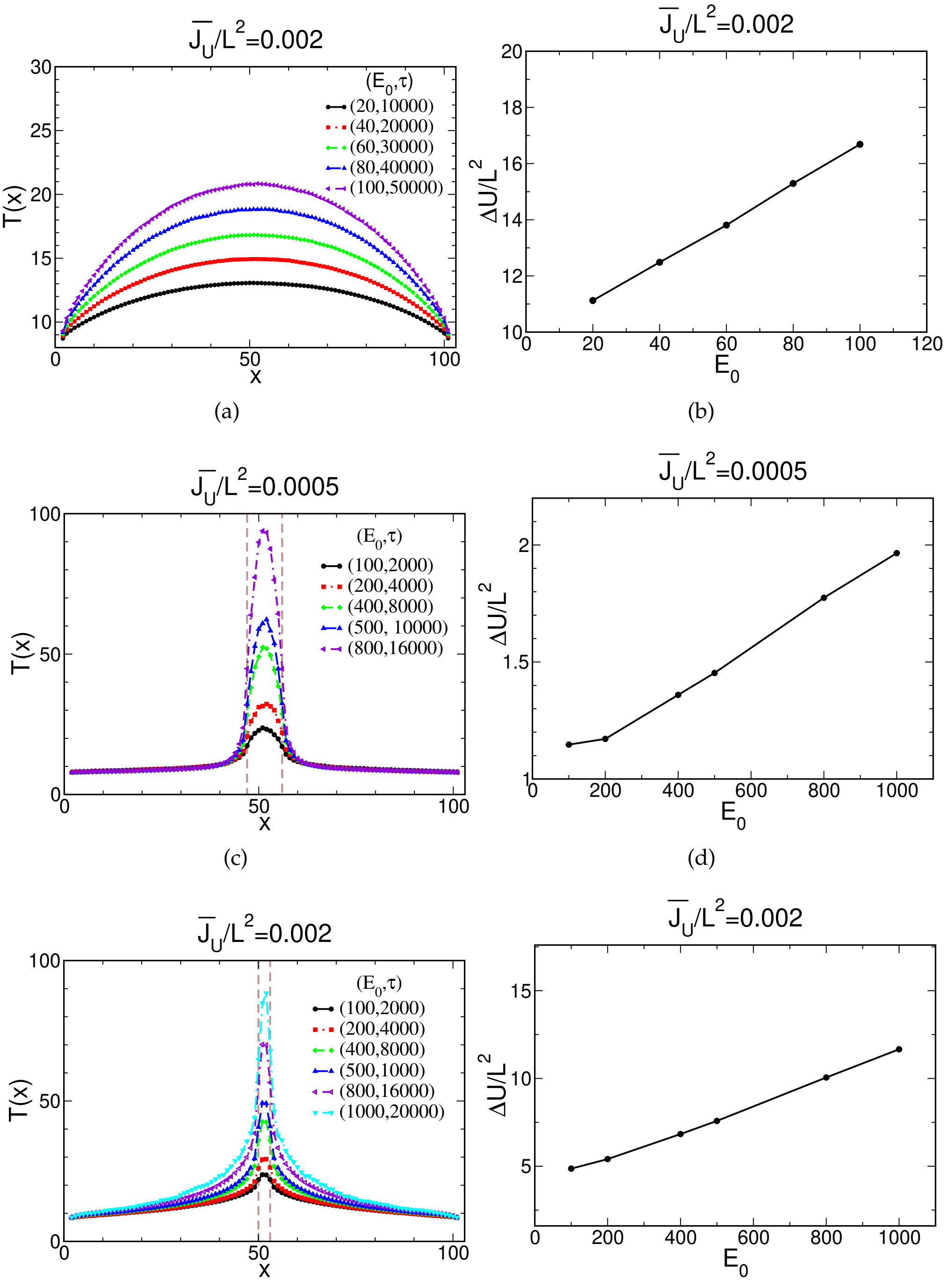

(a) (b)

(c) (d)

(e) (f)

Figure 2.25: $(a)(c)(e)$ Column temperature profiles $\overline{T}(x,\tau)$ under averaged constant energy flux $\overline{J_U}$ for different energy supply geometries. $\overline{J_U}$ per spin is denoted above each panel, and the specific values of the (E_0,τ) pairs are denoted for each curve. Temperature is measured in units of J/k_B. $(b)(d)(f)$ Energy storage ΔU per spin under constant $\overline{J_U}$ for different supply geometries. Panels $(a),(b)$ correspond to geometry A_1; $(c),(d)$ to A_2; $(e),(f)$ to A_3.

As we can see, different protocols of energy supply lead to different steady states, demonstrated by different temperature profiles and different stored energy. Further, in each geometry, we find that the energy stored from large but rare deliveries (large E_0 and τ) is greater than that from small but frequent deliveries (small E_0 and τ). This holds if the characteristic time scale $\mathcal{T} = \Delta U / J_U$ of energy outflow from the system is smaller than the period τ of the energy supply. For $\mathcal{T}$ comparable to τ, the stored energy is minimal. For $\mathcal{T}$ larger than τ, the system does not reach periodic steady states. In addition, comparing Fig. 2.25(b) and 2.25(f), we find that the energy storage is greater under a larger delivery area ($A_1 > A_3$).

2.4.4.2 Systems under Constraints

Now, we test Hypothesis 2.1.1. Following the same methodology used in previous sections, an adiabatic horizontal wall is placed between row y_w and $y_w + 1$. It separates the system into two subsystems: upper and lower. In practice, this is achieved by setting the interaction strength between spins at row y_w and $y_w + 1$ to zero. A scheme of this constrained system is shown in Fig. 2.26.

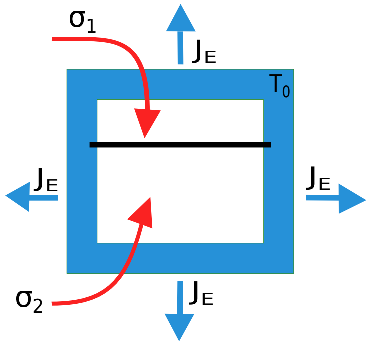

Figure 2.26: Scheme of a constrained system. The horizontal line denotes the constraint which is an adiabatic wall. The energy flux is kept non-zero in each subsystem.

The constraint does not change the total amount of energy influx, *i.e.*, $\overline{J_U} = \overline{J_U}_{\text{upper}} + \overline{J_U}_{\text{lower}}$. We use geometry A_1 and A_3 (Fig. 2.22) and protocols denoted in red in Table 2.3. The choice of the geometries ensures that when adjusting $y_w \in (2, L+1)$, each subsystem will have a nonzero heat flux.

For geometry A_1, the total heat flux is fixed at $\overline{J_U}(A_1, E_0, \tau) = \overline{J_U}(A_1, 20, 10000) = 0.002 \times L^2$. To observe the temperature change across the wall, we plotted the averaged row temperature

$$\overline{T}(y, \tau) = \sum_x \overline{T}(x, y, \tau)/L \tag{2.143}$$

against y. Results of $\overline{T}(y, \tau)$ and the stored energy at different y_w are shown in Fig. 2.27.

For geometry A_3, we fix the total flux $\overline{J_U} = 0.002 \times L^2$ and adjust four pairs of (E_0, τ). Fig. 2.28 shows the row temperature profiles for each pair of (E_0, τ) (panel $(a) - (d)$) and the stored energy in all situations (panel (e)). Similar to the results for geometry A_1,

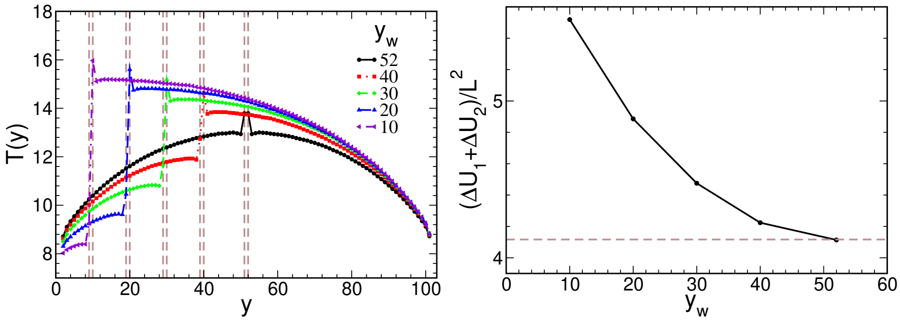

(a) (b)

Figure 2.27: (a) Row temperature profiles $\overline{T}(y,\tau)$ and (b) total energy storage per spin under energy supply protocol $\overline{J_U}(A_1, E_0, \tau) = \overline{J_U}(A_1, 20, 10000) = 0.002 \times L^2$. T is measured in units of J/k_B. A pair of dashed line in (a) denotes the position of a constraint placed between row y_w and $y_w + 1$. The horizontal line in (b) denotes the energy storage (per spin) without constraints.

under each protocol, the stored energy of the periodic steady state in the unconstrained system is equal to that where the constraint separates the system into two equal parts. It is also lower than all other partitions. These results are in accordance with Hypothesis 2.1.1.

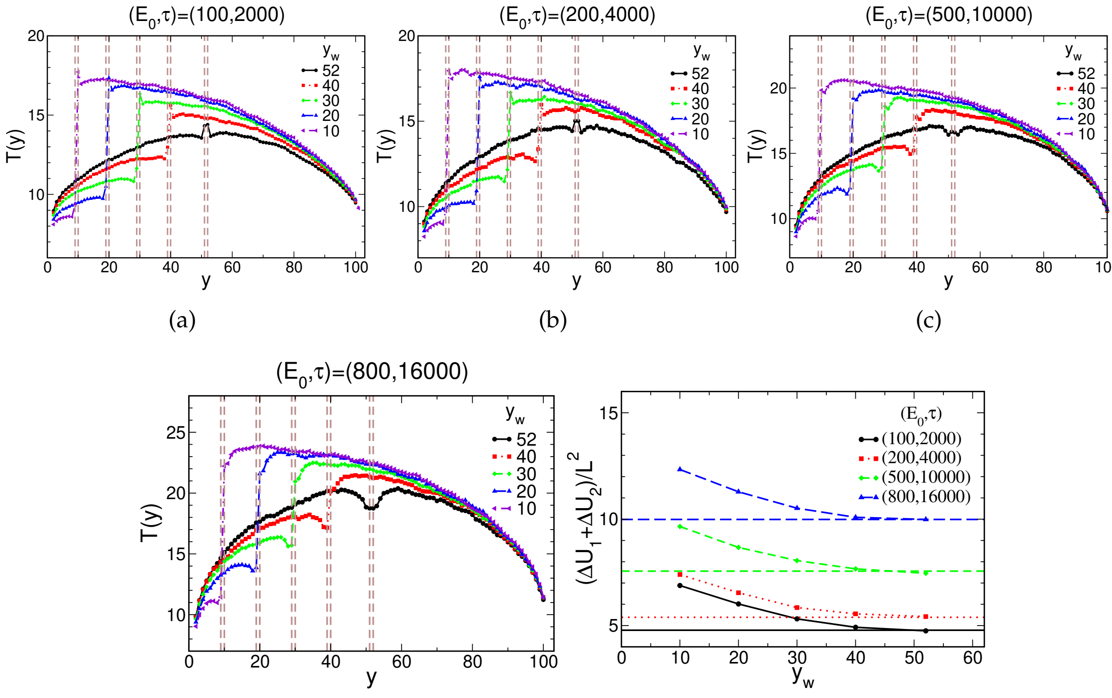

(a) (b) (c)

(d) (e)

Figure 2.28: Row temperature profiles $\overline{T}(y,\tau)$ and the total energy storage under A_3 geometry. The averaged total flux is fixed at $\overline{J_U}(A_3, E_0, \tau) = 0.002 \times L^2$. Panels $(a) - (d)$ show $\overline{T}(y)$ under different positions of the constraint y_w, for four pairs of (E_0, τ). The corresponding (E_0, τ) pair is denoted above the graph. Dashed lines denote the constraints between row y_w and $y_w + 1$. Panel (e) shows the stored energy against y_w for four pairs of (E_0, τ). The horizontal lines correspond to the stored energy without constraint. Temperature is measured in units of J/k_B.

2.5 Summary and Conclusion

In this chapter, we have analysed the energy storage ΔU and total heat flow J_U for a variety of systems in NESS. These models are distinct in nature and driven by diverse protocols. Using these results, we have addressed two main questions.

The first question concerns the energy storage in NESS under different driving protocols. Energy storage is an interesting and important problem. It is relevant for potential applications, for example, in energy harvesting [99]. Understanding how the average energy storage depends on the details of J_U, on the internal geometrical constraints of the system, points to directions to increase energy storage efficiency.

This question is explored in Sec. 2.4, where we have studied periodic steady states of a magnetic system under different protocols of local cyclic energy supply using simulation. We have manipulated the geometry, amplitude, and period of the protocol, while keeping the total flux constant and compared the resulting temperature profile and the energy storage in the periodic steady states.

In particular, we have pointed out the importance of the mode of energy transfer into the system. The energy storage depends not only on the total energy flow J_U, but also on the detailed method of energy transfer. Moreover, the system stores more energy under large and rare energy delivery than small and frequent delivery, and more under a large delivery area than a small delivery area. Further studies exploring this quantity in various examples of NESSs would shed light on the generality of this hypothesis.

Second, we have proposed our first hypothesis of variational principle based on the quantity $\mathcal{T} \equiv \Delta U / J_U$ (see Hypothesis 2.1.1). It states that $\mathcal{T}$ is minimized for NESS. $\mathcal{T}$ has an interpretation of the characteristic time scale of energy outflow from the system immediately after the shutdown of the energy input. This interpretation can be seen from simulation results of the Lennard-Jones fluid in Sec. 2.2.2. We have presented methodologies to examine this hypothesis in Sec. 2.1. For models in general, the method is to introduce constraints and check if $\mathcal{T} \leq \mathcal{T}_{1|2}$ (where the latter is the value of $\mathcal{T}$ under constraint). For models where competing steady states can be achieved, we check if $\mathcal{T}$ is the smallest for stable states.

We have checked this hypothesis against distinct models and under a variety of energy supply methods. In particular, we have checked using an ideal gas system under various bulk energy supplies (Sec. 2.2.1), under the external heat flow (Sec. 2.3.1); a fluid system driven by matter flow (Sec. 2.3.2); an Ising system under various periodic local energy supplies (Sec. 2.4). We have supplemented our message with the Lennard-Jones fluid (Sec. 2.2.2) and the Rayleigh-Bénard system (Sec. 2.3.3). Results of these two models are reproduced from [1]. In the end, results in all models have confirmed Hypothesis 2.1.1.

However, we are aware of an example where this hypothesis falls short. In an example pointed out by the referee of [1], a heat tank is connected to the system with a heat conducting wire. Depending on the position of the wire, the relation between $\mathcal{T}$ and $\mathcal{T}_{1|2}$ may be reverted depending on the size of the heat tank. To see this, let us consider the case of the ideal gas with a homogeneous energy supply (**case 1** of Sec. 2.2.1). The comparison of $\mathcal{T}$ and $\mathcal{T}_{1|2}$ becomes

$$U + \frac{3}{2}N_t k_B T(x_t) \quad \text{and} \quad U_1 + U_2 + \frac{3}{2}N_t k_B T'(x_t), \tag{2.144}$$

where U, U_1 and U_2 are the steady state energy of the system, subsystems 1 and 2, respectively; N_t is the number of particles in the tank; x_t is the position where the tank is attached. Rearranging terms, the comparison becomes

$$\frac{3}{2}N_t k_B \left(T(x_t) - T'(x_t)\right) \quad \text{and} \quad U_1 + U_2 - U. \tag{2.145}$$

When the constraint reduces the temperature of the heat tank, the relation depends heavily on the size of the tank. Hence, Hypothesis 2.1.1 does not hold for all cases and must be changed. In light of this counterexample, we seek to adapt our hypothesis in the next chapter.

Chapter 3

Embedded Energy in Nonequilibrium Steady States

3.1 Embedded Energy and the Second Hypothesis

Observations

It is interesting to notice that, for most models studied in the previous chapter, the steady state energy U can be written as a product of the equilibrium energy U_{eq} and a dimensionless function of the heat flow J_U, $U = U_{eq} \cdot f(J_U)$.

This seems to be a trivial observation, especially for ideal gas under bulk energy supplies. Since, in this case, U is a function of the normalised energy supply density λ and so is the total heat flow J_U, U can certainly be written as a function of J_U. However, our main concern is about the proper variables of the nonequilibrium steady states, where the heat may come in many forms. It would be intriguing if, in general, the steady state energy can be expressed as a function of the total energy flow.

Here, using the analytical expressions of U and J_U obtained from the test models in the previous chapter, we will rewrite U as a function of J_U. Specifically, these models are the five models of ideal gas under bulk energy supply in Sec. 2.2, ideal gas under heat flow Sec. 2.3.1, and the Poiseuille-Hagen flow in Sec. 2.3.2.

First, let us look at the expressions of the five ideal gas models in Sec. 2.2. For all of these models, the total heat flow is normalised with a constant $\mathcal{A}kT_0/L$ and becomes a dimensionless quantity

$$\widetilde{J}_U = \frac{L}{\mathcal{A}kT_0} J_U. \tag{3.1}$$

As stated before, $\mathcal{A}$ and L are the area and length of the system, k is the heat conductivity and T_0 is the heat bath temperature. (For an illustration of the model, see Fig. 2.1.) For **case 1** and **case 5**, $\widetilde{J}_U = 2\widetilde{\lambda}_1$, and the steady state energy can be written as (compare with Eq. (2.22)),

$$U = U_{eq} \frac{\sqrt{\widetilde{J}_U \left(\widetilde{J}_U + 4\right)}}{4\,\mathrm{Arctanh}(\sqrt{\widetilde{J}_U / \left(\widetilde{J}_U + 4\right)}}. \tag{3.2}$$

Similarly, for **case 2**, the total heat flow reduces to (compare to Eq. (2.37)),

$$\widetilde{J}_U = 2\sqrt{\widetilde{\lambda}_2}\tan(\sqrt{\widetilde{\lambda}_2}). \tag{3.3}$$

We define $\widetilde{J}_U = g(\widetilde{\lambda}_2)$, then since $\widetilde{J}_U$ is a monotonic function of $\widetilde{\lambda}_2$, $\widetilde{\lambda}_2$ can be expressed as an implicit function of $\widetilde{J}_U$, $\widetilde{\lambda}_2 = g^{-1}(\widetilde{J}_U)$. Then, U is expressed as (compare to Eq. (2.34))

$$U = U_{eq}\frac{2\sqrt{g^{-1}(\widetilde{J}_U)}}{\cos\left(\sqrt{g^{-1}(\widetilde{J}_U)}\right)\ln\left(\dfrac{1+\sin\left(\sqrt{g^{-1}(\widetilde{J}_U)}\right)}{1-\sin\left(\sqrt{g^{-1}(\widetilde{J}_U)}\right)}\right)}. \tag{3.4}$$

For **case 3**, the total heat flow reduces to $\widetilde{J}_U = 2\widetilde{\lambda}_3$ (compare to Eq. (2.55)). An intermediate quantity ω has been introduced in Eq. (2.53), and $\widetilde{\lambda}_3$ can be expressed as a function of ω, $\widetilde{\lambda}_3 = \sqrt{\pi}\,\mathrm{erf}(\omega)\omega\exp(\omega^2)$. We define this function as $m(\omega)/2$, and $\widetilde{J}_U = 2\widetilde{\lambda}_3 = m(\omega)$. Function m is again monotonic; hence ω can be expressed implicitly as $\omega = m^{-1}(\widetilde{J}_U)$. Then, from Eq. (2.52), the steady state energy can be written as,

$$U = U_{eq}\frac{\widetilde{J}_U}{4(m^{-1}(\widetilde{J}_U))^2}. \tag{3.5}$$

Finally, for **case 4**, unfortunately, it is difficult to examine if this conversion and rewriting are possible since it involves hypergeometric functions.

Likewise, the analysis can be applied to the ideal gas under heat flow (Sec. 2.3.1). Using the same normalization quantity $\mathcal{A}kT_0/L$, the total energy flow reduces to $\widetilde{J}_U = \widetilde{T}_1 - 1$ (see Eq. (2.85)). Consequently, the steady state energy is expressed as

$$U = U_{eq}\frac{\widetilde{J}_U}{\ln\left(\widetilde{J}_U + 1\right)}. \tag{3.6}$$

Lastly, for the Hagen-Poiseuille flow (Sec. 2.3.2), since the height of the model is denoted as $2h$, the normalisation factor is $\mathcal{A}kT_0/h$. The steady state internal energy can be rewritten as (compare Eq. (2.105))

$$U = U_{eq} + \frac{1}{10}\frac{J_U h}{\mathcal{A}kT_0} \times \frac{3}{2}n_0 k_B T_0 = U_{eq}(1 + \frac{1}{10}\cdot\widetilde{J}_U). \tag{3.7}$$

To summarise, for all analytically studied models (except **case 4**) in Chapter 2, the total heat flow is normalised using a factor of the form $\mathcal{A}kT_0/L$ or $\mathcal{A}kT_0/h$, and the steady state energy can be expressed in the form $U = U_{eq}\cdot f(\widetilde{J}_U)$.

Embedded Energy and Proposal of a Second Hypothesis

Can the above observations, $U(U_{eq}, J_U) = U_{eq} \cdot f(\widetilde{J}_U)$, be extended to nonequilibrium steady states in general? In other words, are J_U and U_{eq}, in fact, state parameters? It seems, so far, that these two quantities can be related to the state parameters. The observations, however, are certainly not conclusive, and the question remains open. Nevertheless, we can proceed to assume that indeed U_{eq} and J_U are the parameters of nonequilibrium steady states. Then, following the procedure in Chapter 2, we form a hypothesis and examine it with different models.

As reviewed in Sec. 1.1 of equilibrium thermodynamics, for an open system defined by a fixed temperature T, volume V and number of particles N, the Helmholtz free energy is obtained from the Legendre transform of U with respect to entropy S (see Eq. (1.25)),

$$F(T, V, N) = U - \frac{\partial U}{\partial S} S. \tag{3.8}$$

And F is minimized for equilibrium states. Following this fact, we propose an analog of the Helmholtz free energy for NESS – the Legendre transform of U with respect to J_U,

$$U^* \equiv U - \frac{\partial U}{\partial J_U} \cdot J_U. \tag{3.9}$$

This quantity is termed *embedded energy*. The analogy between U^* and the Helmholtz free energy is especially interesting. Since J_U/T_0 coincides with the entropy production rate, that is, the entropy flow leaving the system through the wall at temperature T_0, this suggests that U^* is a function of the entropy production rate $\dot{S}_{tot}$. And likewise, we propose the second hypothesis using the embedded energy:

Hypothesis 3.1.1. $\mathcal{U}^*$ is minimized in nonequilibrium steady states.

The embedded energy may be interpreted as the amount of energy that must stay in the system to keep the NESS. The derivative $\partial U/\partial J_U$ has a dimension of time. And the term $J_U \cdot \partial U/\partial J_U$ is the amount of heat flowing into the system during this time. The difference U^* is then the amount of energy that does not flow out of the system at all times, hence the name *embedded energy*.

The methodology for testing this hypothesis is the same as method 1 described in Sec. 2.1. Explicitly, for each model, U and J_U are firstly obtained, and U^* is calculated. Next, an external constraint is introduced into the system, and the energy and heat flow of each subsystem, U_i and J_{U_i}, are obtained. The embedded energy under constraint $U^*_{1|2}$ is

$$U^*_{1|2} = U_1 - \frac{\partial U_1}{\partial J_{U_1}} J_{U_1} + U_2 - \frac{\partial U_2}{\partial J_{U_2}} J_{U_2}. \tag{3.10}$$

In this chapter, Hypothesis 3.1.1 is tested with two models. The first model is the ideal gas under the homogeneous bulk energy supply $\sigma_E = \lambda_1$, same as in **case 1** of Sec. 2.2.1. The second model is the ideal gas under an external heat flow, same as in Sec. 2.3.1.

3.2 Ideal Gas under Bulk Energy Supply

Using the model in **case 1** of Sec. 2.2.1, we test Hypothesis 3.1.1: the minimization principle of the embedded energy in NESS. The schematic plot of this model is reproduced here in Fig. 3.1 for quick reference. Like before, the system is a three-dimensional ideal gas of fixed volume V and number of particles N, placed in a heat bath of temperature T_0; the system is placed between plates of area $\mathcal{A}$ at $x = \pm L$, and the volume is $V = 2\mathcal{A}L$; a homogeneous energy supply of density λ_1 is applied; a constraint is placed at x_1; heat conductivity is k.

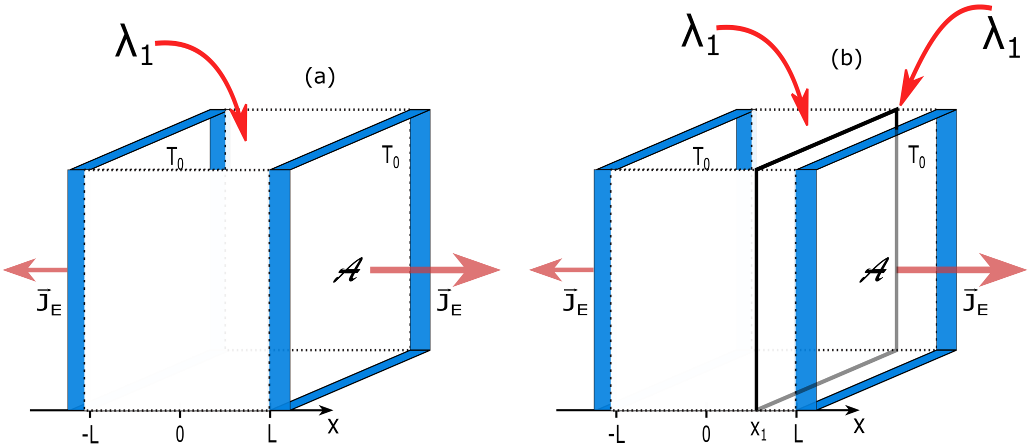

Figure 3.1: Reproduction of Fig. 2.1. Schemes of (a) unconstrained and (b) constrained ideal gas model under a homogeneous bulk energy supply of density λ_1. The two diathermal walls of area $\mathcal{A}$ and temperature T_0 are positioned at $x = \pm L$. The heat flux density $\vec{J}_E$ flows out of the system through boundaries. In (b), the vertical plane at $x = x_1$ represents the internal constraint – an adiabatic wall.

Using the reduced length of subsystems, $l_1 = 1 + \tilde{x}_1$ and $l_2 = 1 - \tilde{x}_1$ with $\tilde{x}_1 = x_1/L$, and the normalised energy supply density $\tilde{\lambda}_1 = \lambda_1 L^2/kT_0$, we rewrite the previously obtained steady state energy as follows (see Eqs. (2.22) and (2.25)),

$$U = \frac{U_{eq}}{2} \frac{\sqrt{\tilde{\lambda}_1(\tilde{\lambda}_1 + 2)}}{\text{Arctanh}(\sqrt{\tilde{\lambda}_1/(\tilde{\lambda}_1 + 2)})}, \tag{3.11}$$

$$U_1 = \frac{U_{eq}^{(1)}}{2} \frac{\sqrt{\tilde{\lambda}_1 l_1^2(\tilde{\lambda}_1 l_1^2 + 2)}}{\text{Arctanh}\left(\sqrt{\tilde{\lambda}_1 l_1^2/(\tilde{\lambda}_1 l_1^2 + 2)}\right)}, \tag{3.12}$$

$$U_2 = \frac{U_{eq}^{(2)}}{2} \frac{\sqrt{\tilde{\lambda}_1 l_2^2(\tilde{\lambda}_1 l_2^2 + 2)}}{\text{Arctanh}\left(\sqrt{\tilde{\lambda}_1 l_2^2/(\tilde{\lambda}_1 l_2^2 + 2)}\right)}. \tag{3.13}$$

$U_{eq}^{(1)} = \epsilon_0 \mathcal{A} L l_1$ and $U_{eq}^{(2)} = \epsilon_0 \mathcal{A} L l_2$ are the equilibrium energy of the corresponding subsystem, and ϵ_0 is the equilibrium energy density. And the total heat flow of the system and subsystems have been obtained

$$J_U = 2\mathcal{A}L\lambda_1, \quad J_{U_1} = \mathcal{A}Ll_1\lambda_1 \text{ and } J_{U_2} = \mathcal{A}Ll_2\lambda_1. \tag{3.14}$$

To obtain the expression for U^* (3.9), we first need to find the expression for the derivative. For the system without constraints, both U and J_U are functions of λ_1. Using the chain rule, the partial derivative with respect to J_U becomes a total derivative with respect to $\widetilde{\lambda}_1$. And the embedded energy is

$$U - \frac{\partial U}{\partial J_U} J_U = U - \frac{\mathrm{d}U}{\mathrm{d}\widetilde{\lambda}_1}\frac{\partial \widetilde{\lambda}_1}{\partial J_U} J_U = U - \frac{\mathrm{d}U}{\mathrm{d}\widetilde{\lambda}_1}\widetilde{\lambda}_1. \tag{3.15}$$

For the constrained system, both U_i and J_{U_i} are seemingly functions of l_i and $\widetilde{\lambda}_1$. Yet, since the constraint is fixed, l_i is fixed; hence the energy and the heat flow are again functions of a single variable $\widetilde{\lambda}_1$. Therefore, the embedded energy of subsystem i is

$$U_i - \frac{\partial U_i}{\partial J_{U_i}} J_{U_i} = U_i - \frac{\partial U_i}{\partial \widetilde{\lambda}_1}\frac{\partial \widetilde{\lambda}_1}{\partial J_{U_i}} J_{U_i} = U_i - \frac{\partial U_i}{\partial \widetilde{\lambda}_1}\widetilde{\lambda}_1. \tag{3.16}$$

Finally, substituting Eqs.(3.11), (3.12) and (3.13), we obtain U^* for the system as

$$U^* = \frac{U}{\widetilde{\lambda}_1 + 2}\left(1 + \frac{U}{U_{eq}}\right), \tag{3.17}$$

and the constrained system as

$$\begin{aligned} U^*_{1|2} &= U_1 - \frac{\partial U_1}{\partial \widetilde{\lambda}_1}\widetilde{\lambda}_1 + U_2 - \frac{\partial U_2}{\partial \widetilde{\lambda}_1}\widetilde{\lambda}_1 \\ &= \frac{U_1}{\widetilde{\lambda}_1 l_1^2 + 2}\left(1 + \frac{U_1}{U_{eq}^{(1)}}\right) + \frac{U_2}{\widetilde{\lambda}_1 l_2^2 + 2}\left(1 + \frac{U_2}{U_{eq}^{(2)}}\right). \end{aligned} \tag{3.18}$$

Due to the complex form of the embedded energy, it is difficult to compare U^* and $U^*_{1|2}$ analytically. Instead, we directly inspect their numerical values at several $\widetilde{\lambda}_1$. Results show that $U^* \leq U^*_{1|2}$, in accordance with Hypothesis 3.1.1. An example of the comparison at $\widetilde{\lambda}_1 = 10.0$ is shown in Fig. 3.2.

Adding a Heat Tank

At the end of Chapter 2, a counterexample of Hypothesis 2.1.1 was proposed. In this example, an additional adiabatic system is connected to the ideal gas model via a heat conducting wire. This extra system serves as a heat tank and stores energy depending on its size and the temperature it connects. $\mathcal{T}$ of this total system now depends on this heat tank, and the comparison between $\mathcal{T}$ and $\mathcal{T}_{1|2}$ may be reversed depending on the size of

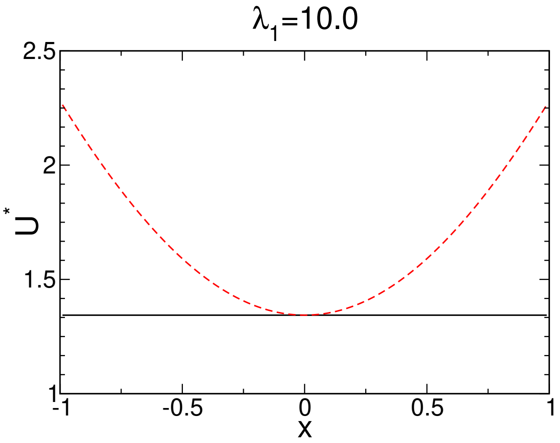

Figure 3.2: Comparison between the embedded energy U^* of constrained (red) and unconstrained system (black). The embedded energy is plotted against the position of the constraint x. The energy supply is homogeneous with density $\lambda_1 = 10.0$, measured in units of kT_0/L^2. And U^* is measured in units of U_{eq}.

the heat tank. Here, we discuss how such a heat tank influences the second hypothesis, the minimization of U^*.

Suppose now that the ideal gas is attached with such a heat tank via a heat conducting wire positioned at x_t. The tank is of a fixed volume V_t and number of particles N_t. The whole system now consists of both the system and the heat tank. When the whole system settles into a steady state, there is no heat flow between the system and the heat tank. In other words, the heat tank is in equilibrium with the temperature at x_t in the system, *i.e.*, $T_t = T(x_t)$. Thus, the energy of the heat tank is

$$U^T = \frac{3}{2} k_B N_t T_t = C_{V_t} T_t. \tag{3.19}$$

The embedded energy U^* of the whole system is now

$$U^* \equiv U + U^T - \frac{\partial (U + U^T)}{\partial J_U} J_U. \tag{3.20}$$

As stated previously, the partial derivative can be expressed with respect to λ_1 using the chain rule. The embedded energy can be separated into U^* of the system and the heat tank,

$$\begin{aligned} U^* &= \left(U - \frac{\mathrm{d}U}{\mathrm{d}\lambda_1} \lambda_1 \right) + \left(U^T - \frac{\mathrm{d}U^T}{\mathrm{d}\lambda_1} \lambda_1 \right) \\ &\equiv U^*_{system} + U^*_{tank}. \end{aligned} \tag{3.21}$$

Consider the term of the heat tank. Since only T_t is a function of λ_1, U^*_{tank} is simply $C_{V_t}(T_t - \lambda_1 \partial T_t / \partial \lambda_1)$. From the temperature profile of the system Eq. (2.21), T_t is given by

$$T_t = -\frac{\lambda}{2k} x_t^2 + 2\frac{\lambda L^2}{2k} + T_0. \tag{3.22}$$

And $T_t - \lambda\partial T_t/\partial\lambda$ leaves only T_0. Therefore,

$$U^* = U^*_{system} + U^T_{eq}, \tag{3.23}$$

where U^T_{eq} is the energy of the heat tank at equilibrium.

Analogously, the total embedded energy of the constrained system can be separated into two parts

$$\begin{aligned} U^*_{1|2} &= \left(U_1 - \frac{\partial U_1}{\partial\lambda}\lambda + U_2 - \frac{\partial U_2}{\partial\lambda}\lambda\right) + \left(U^{T'} - \frac{\partial U^{T'}}{\partial\lambda}\lambda\right), \\ &\equiv U^*_{1|2,system} + U^*_{1|2,tank}. \end{aligned} \tag{3.24}$$

Similarly, $U^*_{1|2,tank}$ is given by $C_{V_t}(T_t^{'} - \lambda\partial T_t^{'}/\partial\lambda)$ with a new temperature at x_t of the constrained system. Specifically, from Eq. (2.24), we have

$$T_t^{'} = -\frac{\lambda}{2k}(x_t - x_1)^2 + \frac{\lambda}{2k}(L + x_1)^2 + T_0 \quad \text{or} \tag{3.25}$$

$$T_t^{'} = -\frac{\lambda}{2k}(x_t - x_1)^2 + \frac{\lambda}{2k}(L - x_1)^2 + T_0, \tag{3.26}$$

where the former corresponds to a x_t in subsystem 1 and the latter in subsystem 2. In either case, however, $(T_t^{'} - \lambda\partial T_t^{'}/\partial\lambda)$ reduces to T_0. Thus, the embedded energy of the whole system under constraint is

$$U^*_{1|2} = U^*_{1|2,system} + U^T_{eq}. \tag{3.27}$$

Since the embedded energy of the tank reduces to U^T_{eq} with and without the constraint, the comparison between Eqs. (3.23) and (3.27) reduces to the contribution from the system. In other words, the tank does not influence the result of Hypothesis 3.1.1: U^* is minimised in steady states.

3.3 Ideal Gas under Heat Flow

In this section, we consider the system in Sec. 2.3.1, an ideal gas under external energy flow from temperature gradient present at its left and right boundary. Like before, the system is of fixed volume V and N; left and right boundary are of area $\mathcal{A}$ (height H and width Z), placed at $x = 0$ and L; the temperature at the left(right) boundary is $T_1(T_0)$. The internal constraints are adiabatic walls with configurations *vertical*, *linear*, and *cosine*. Their expressions are given in Eq. (2.79), and their parameters are height h, slope b, and wavenumber $\hat{k}$, respectively. The schematic plot of these models is reproduced in Fig. 3.3 for quick reference.

From previous results, the energy density and the heat flow of the system are obtained analytically (see Eqs. (2.82) and (2.85)). Both U and J_U are functions of $\widetilde{T}_1 = T_1/T_0$. The

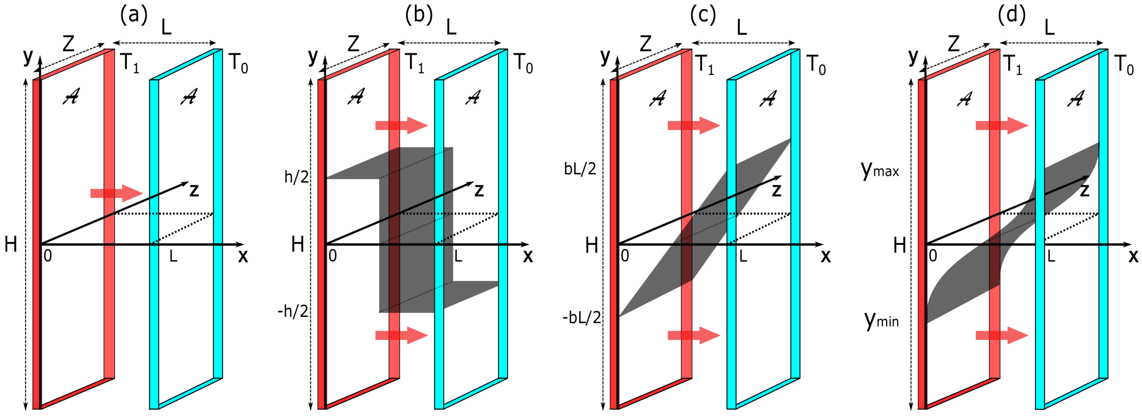

Figure 3.3: Reproduction of Fig. 2.8. Schemes of (a) unconstrained and $(b)(c)(d)$ constrained ideal gas systems under an external heat flow. Two diathermal walls are placed at $x = 0$ and L, kept at temperatures T_1 and T_0, respectively. The constraints are adiabatic walls, denoted in black. In (b), the constraint has a height h and extends from $(0, h/2)$ to $(L/2, h/2)$ to $(L/2, -h/2)$ to $(L, -h/2)$. In (c), the constraint has a slope b and stretches from $(0, -bL/2)$ to $(L, bL/2)$. In (d), the constraint is in the shape of a cosine function of wavenumber $\hat{k}$. It extends from $(0, H/2 + \pi/2\hat{k})$ to $(0, H/2 - \pi/2\hat{k})$, corresponding to phase $(0, \pi)$. The red arrows denote the heat flux.

partial derivative, therefore, can be expressed in terms of $\widetilde{T}_1$ using the chain rule. Thus, the expression of U^* is

$$U^* = U - \frac{\partial U}{\partial \widetilde{T}_1} \frac{\partial \widetilde{T}_1}{\partial J_U} J_U = \frac{U^2}{U_{eq} \widetilde{T}_1}. \tag{3.28}$$

For the constrained system, U^* is obtained numerically using the finite element method (FEM), explained in Sec. 2.3.1.2. First, for a fixed $\widetilde{T}_1$, the subsystem energy U_i and heat flow J_{U_i} are obtained using the same procedure described in Sec. 2.3.1. Primarily, the subsystem temperature profiles are obtained numerically using FEM implemented in Mathematica. Then, the values of U_i and J_{U_i} are obtained using numerical derivation and integrations. Second, the temperature at the left boundary is varied around the value $\widetilde{T}_1$. The same quantities are obtained under each new $\widetilde{T}_1$, giving $U_i(\widetilde{T}_1)$ and $J_{U_i}(\widetilde{T}_1)$. Consequently, the partial derivative $\partial U_i / \partial J_{U_i}$ can be evaluated directly. Finally, these results are combined to obtain

$$U^*_{1|2} = U_1 - \frac{\partial U_1}{\partial J_{U_1}} J_{U_1} + U_2 - \frac{\partial U_2}{\partial J_{U_2}} J_{U_2}. \tag{3.29}$$

Like in Sec. 2.3.1, we evaluate the following test models: $L = 10$ and $H = 60, 80, 100, 150, 180, 200, 400$ and 600 for constraint *vertical* and *linear*; $L = 10$ and $H = 80, 100, 120$ for constraint *cosine*. For each model, the scaled embedded energy U^*/V is evaluated as a function of the reduced parameter of the constraint (h/H for *vertical*, b/H for *linear*, and $1/\hat{k}H$ for *cosine*), at $\widetilde{T}_1 = 10.0$ (shown in Fig. 3.4). The derivations are obtained with respect to $\widetilde{T}_1 \in (9.8, 10.3)$.

From previous discussions (see Sec. 2.3.1), two sources of errors need to be considered. The first is numerical errors from FEM due to conflicting boundary conditions, and

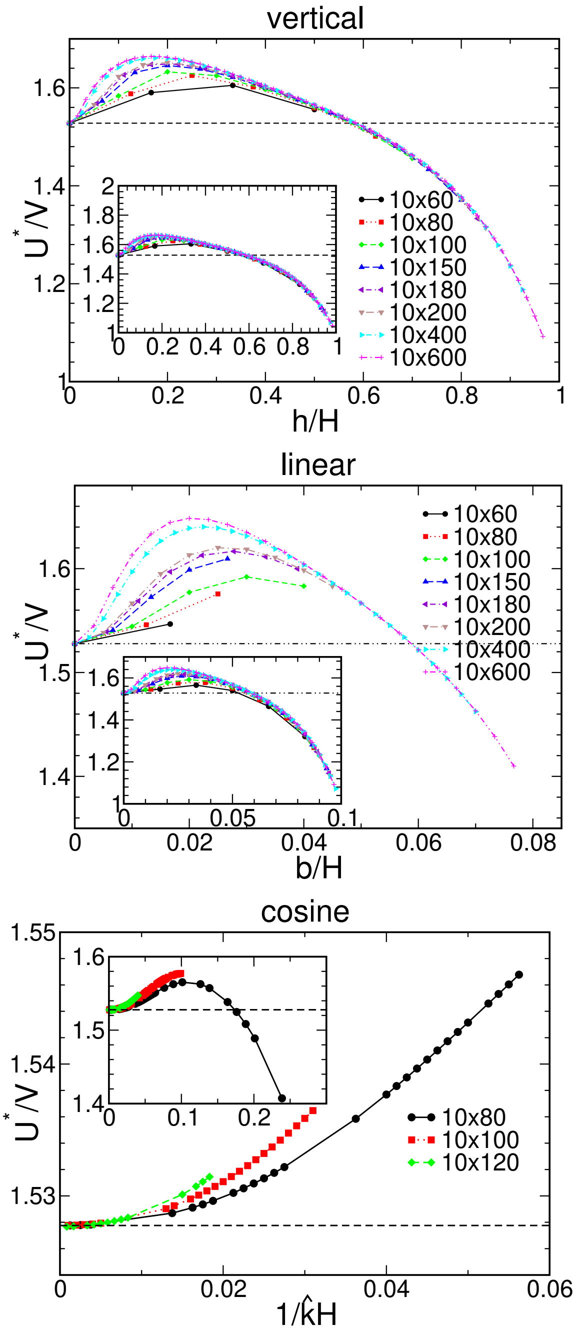

Figure 3.4: Scaled embedded energy U^*/V plotted against scaled parameters x. Specifically, $x = h/H, b/H$, and $1/\hat{k}H$ for configurations *vertical*, *linear*, and *cosine*, respectively. Each curve corresponds to a specific model of different dimensions, denoted in the legends. For *vertical* and *linear*, the length and height of the models are $L = 10, H = 60, 80, 100, 150, 180, 200, 400, 600$; for *cosine*, $L = 10, H = 80, 100, 120$. The horizontal line in each panel corresponds to U^* of the unconstrained model. The insets are results evaluated over a wider range.

the second is errors from the finite size effect.

For the first source of error, the valid parameter ranges for the test models are listed in Table 2.2. To account for the second source of error, we observe the scaled embedded energy $U^*(x)/V$ for regions showing data collapsing, and further restrict valid parameter ranges to these regions. The main panels in Fig. 3.4 show results within the parameter range listed in Table 2.2; the insets show results over a wider range. For constraints *vertical* and *linear*, we see that the larger the model, the wider the range of data collapsing. Especially for models with $H = 400$ and 600, data collapse over the full range of h/H and b/H. Within these new ranges, $U^* \leq U^*_{1|2}$ does not always hold. Therefore, Hypothesis 3.1.1 is not supported.

For constraint *cosine*, we see data collapsing over the region $1/\hat{k}H \leq 0.01$, and results show $U^* \leq U^*_{1|2}$, in accordance with the hypothesis. However, only models of relatively small dimensions are examined. And we expect models of larger dimensions to exhibit data collapsing over a wider range, especially toward the tail of $1/\hat{k}H$, and therefore contradict Hypothesis 3.1.1.

3.4 Summary and Conclusion

In this chapter, we have proposed our second hypothesis, which states that the embedded energy U^* is minimized at NESS (see Hypothesis 3.1.1). This hypothesis is adapted from our previous hypothesis 2.1.1, and we have discussed our motivation for this quantity in the first section. In short, this quantity takes the form "like" the Legendre transform of the energy U with respect to the total heat flow J_U, $U^* \equiv U - J_U \partial_{J_U} U$. This is analogous to the Helmholtz free energy, which is the Legendre transform of the (energetic) fundamental relation with respect to entropy.

Hypothesis 3.1.1 is then tested using two models. The methodology, same as before, is to introduce internal constraints into these models systematically and then compare U^* with $U^*_{1|2}$, the embedded energy under constraint. The first model is an ideal gas under a homogeneous bulk energy supply, same as **case 1** of Sec. 2.2.1. The expressions are obtained analytically. And direct inspections of the embedded energy under several energy supply densities support the hypothesis. In addition, we have discussed the case where a heat tank is attached to the model. (This model has been found to contradict Hypothesis 2.1.1.) Analysis shows that Hypothesis 3.1.1 is supported by this model.

The second model is an ideal gas under an external heat flow, same as Sec. 2.3.1. The results are obtained numerically using the finite element method. It turns out that $U^* > U^*_{1|2}$ under certain constraints, contradictory to the hypothesis. Therefore, Hypothesis 3.1.1 must be adapted.

Chapter 4

Competing Steady States and Phase Transitions

In previous chapters, one important test model is the ideal gas model under a homogeneous energy supply, with a fixed adiabatic wall as the internal constraint. This model is simple and analytical. Therefore, it is used as the first testing model for both hypotheses (see Sec. 2.2.1 and Sec. 3.2). The choice of internal constraint, a fixed and adiabatic wall, is also due to simplicity. This choice results in subsystems that are independent.

An interesting question arises: what would happen if the subsystems are coupled instead? This coupling, where some form of exchange happens between subsystems, could be achieved via a variety of methods. For example, we have studied the model with a diathermal internal constraint (**case 5** in Sec. 2.2.1), where subsystems are coupled through heat exchange.

In this chapter, we examine a new model that originated from the above question. An *adiabatic and movable* wall is chosen as the internal constraint. The two subsystems are now coupled via mechanical forces. We refer to this model as the *movable wall model*.

Interestingly, this model exhibits unexpected behaviours. Evaluations reveal that this system undergoes a nonequilibrium phase transition depending on the energy supply density λ_1. Moreover, beyond the transition point $\lambda_1 = \lambda_c$, the system exhibits competing steady states.

This chapter is organised as follows. In the first section, the movable wall model is defined and examined. We will also analyse the phase transition and the competing steady states beyond λ_c. The next two sections are devoted to using this model as the test model for various hypotheses. In Sec. 4.2, we will re-examine Hypothesis 2.1.1 and Hypothesis 3.1.1. In Sec. 4.3, out of curiosity, we will propose the expressions of four additional nonequilibrium potentials using the local equilibrium assumption; and we form hypotheses for each potential. The motivation is to check the form of nonequilibrium potentials analogous to the equilibrium thermodynamic potentials. Together with the paradigm model – the ideal gas with a fixed adiabatic wall – we examine these new hypotheses. Finally, we conclude in Sec. 4.4.

4.1 Movable Wall Model

4.1.1 Model Description

Starting from the paradigm model (**case 1** of Sec. 2.2.1), we again consider a closed ideal gas model under a homogeneous external energy supply of density $\sigma_E = \lambda_1$. A *movable wall model*, in this section, refers to the case where an adiabatic movable wall is introduced as the internal constraint. A scheme of the system is shown in Fig. 4.1. Like before, the system has a fixed volume V and number of particles N, placed in a heat bath of temperature T; the left and right boundary are of area $\mathcal{A}$, placed at $x = \pm L$; heat conductivity is a constant k.

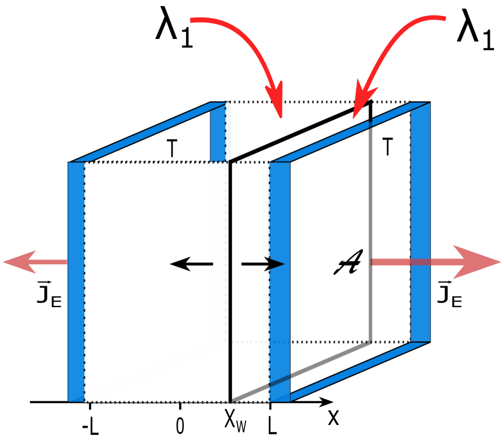

Figure 4.1: Schematic plot of movable wall model. An ideal gas is placed between two diathermal walls of area $\mathcal{A}$, placed at $x = \pm L$, and kept at temperature T. An adiabatic movable wall is present in the system, denoted by the vertical plane. Energy is supplied homogeneous with a density λ_1. The heat flux density is denoted by $\vec{J}_E$.

The movable wall model is different from **case 1** in one important aspect: the constraint in **case 1** is *fixed*; in the movable wall model, the constraint moves freely without friction. Consequently, the constraint in **case 1** is inserted such that the average particle density in each subsystem is the same; whereas in the movable wall model, the ratio of the number of particles of the subsystems, N_1/N_2, can be set arbitrarily. Practically, to achieve any intended partition N_1 and N_2, the wall can be inserted in equilibrium where, according to the ideal gas law

$$PV_i = N_i k_B T, \tag{4.1}$$

with pressure P and the Boltzmann constant k_B, the ratio of N_i corresponds to the ratio of volume V_i.

Now that the two subsystems are coupled via pressure and can exchange work, the system reaches steady states when the pressure exerted from each subsystem becomes the same

$$P_1(X_w) = P_2(X_w), \tag{4.2}$$

where X_w is the position of the constraint. From Eq. (2.10), this condition is equivalent to a match of subsystem energy density

$$\epsilon_1(X_w) = \epsilon_2(X_w). \tag{4.3}$$

The explicit expression of Eq. (4.3) is obtained as follows. The expression of the subsystem energy density is given in Eq. (2.18),

$$\epsilon_1 = \frac{3}{2}N_1 k_B \frac{1}{\displaystyle\int_{V_1} \frac{\mathrm{d}r^3}{T_1(\vec{r})}} \quad \text{and} \quad \epsilon_2 = \frac{3}{2}N_2 k_B \frac{1}{\displaystyle\int_{V_2} \frac{\mathrm{d}r^3}{T_2(\vec{r})}}. \tag{4.4}$$

The temperature profiles are the same as in **case 1** and given by Eq. (2.24). Then, the energy density is

$$\begin{aligned} \epsilon_1 &= \frac{3}{2}\frac{N_1 k_B T}{\mathcal{A}L}\frac{\sqrt{\widetilde{\lambda}_1(\widetilde{\lambda}_1 l_1^2+2)}}{2\,\text{Arctanh}\sqrt{\widetilde{\lambda}_1 l_1^2/(\widetilde{\lambda}_1 l_1^2+2)}} \equiv \frac{3}{2}\frac{N_1 k_B T}{V_1} f(\widetilde{\lambda}_1 l_1^2), \\ \epsilon_2 &= \frac{3}{2}\frac{N_2 k_B T}{\mathcal{A}L}\frac{\sqrt{\widetilde{\lambda}_1(\widetilde{\lambda}_1 l_2^2+2)}}{2\,\text{Arctanh}\sqrt{\widetilde{\lambda}_1 l_2^2/(\widetilde{\lambda}_1 l_2^2+2)}} \equiv \frac{3}{2}\frac{N_2 k_B T}{V_2} f(\widetilde{\lambda}_1 l_2^2), \end{aligned} \tag{4.5}$$

where l_i is the length of subsystem i normalised with L; with $x_w \equiv X_w/L$ as the normalised position of the wall, $l_1 = 1 + x_w$ and $l_2 = 1 - x_w$; $\widetilde{\lambda}_1 = \lambda_1 L^2/kT_0$ is the normalised energy supply density; function f is defined as

$$f(x) \equiv \frac{\sqrt{x(x+2)}}{2\,\text{Arctanh}\sqrt{x/(x+2)}}. \tag{4.6}$$

Moreover, the energy of each subsystem is simplified to

$$U_1 = \frac{3}{2}N_1 k_B T f(\widetilde{\lambda}_1 l_1^2) \quad \text{and} \quad U_2 = \frac{3}{2}N_2 k_B T f(\widetilde{\lambda}_1 l_2^2). \tag{4.7}$$

The author would like to point out that Eq. (4.5) is different from the energy density of **case 1** (see Eq. (2.25)). Finally, the condition for NESS (Eqs. (4.2) and (4.3)) simplifies to

$$\frac{N_1 f\left(\widetilde{\lambda}_1(1+x_w)^2\right)}{1+x_w} = \frac{N_2 f\left(\widetilde{\lambda}_1(1-x_w)^2\right)}{1-x_w}. \tag{4.8}$$

4.1.2 Phase Transition

As stated previously, the movable wall model is different from **case 1** in that the constraint is movable. This single difference results in an interesting nonequilibrium phase transition and competing steady states which we will discuss next. The order parameter is the stable position of the wall X_w.

Let us start from the simplest case by choosing $N_1 = N_2 = N/2$. The steady state condition (4.8) becomes

$$\frac{f\left(\widetilde{\lambda}_1(1+x_w)^2\right)}{1+x_w} = \frac{f\left(\widetilde{\lambda}_1(1-x_w)^2\right)}{1-x_w}. \tag{4.9}$$

Under a fixed λ_1, the (normalised) steady state positions of the wall $x_w^{(i)}$ are obtained by solving (4.9) numerically. In the following, we will denote the ith solution of a quantity with superscript $-^{(i)}$. Graphically, by plotting ϵ_1 and ϵ_2 as a function of x_w, the solutions are observed as the crossing points of these two curves. And their stabilities can be qualitatively analysed from the graph. Let us first look at this problem graphically.

Naturally, $x_w = 0$ is a solution. In this case, the system is separated into two identical subsystems. Hence, $P_1 = P_2$ trivially. We denote this solution as $x_w^{(1)}$. This is indeed the situation for small $\widetilde{\lambda}_1$, where the system has only one steady state $x_w^{(1)}$, and this state is stable. An example of this phase is shown in Fig. 4.2 (a). As shown in the figure, the curves are monotonic, and has only 1 crossing point at the center.

To see the stability of $x_w^{(1)}$, suppose now that the constraint is pushed away from the center. In Fig. 4.2 (a), it is indicated by the vertical line in $x_w \geq 0$. In this case, one observes that $\epsilon_2 \geq \epsilon_1$, or, $P_2 \geq P_1$, indicating that the net pressure is exerted towards $x_w^{(1)} = 0$. Next, from our previous assumption of fast establishing steady states, we assume that the movement of the constraint is a slow process. In other words, we assume that at every point of the movement process of the wall, the system is in steady states. This assumption allows us to continue using Eq. (4.5) and the curves in Fig. 4.2 (a). As a result, this unbalance of pressure continues until the wall is pushed back to the center. Therefore, in this case, $x_w^{(1)} = 0$ is stable.

For large $\widetilde{\lambda}_1$, interestingly, the system has 3 steady states: $x_w^{(1)} = 0$, and $x_w^{(2)} = -x_w^{(3)} \neq 0$ due to symmetry. Qualitatively, one can imagine the asymmetric solutions as follows. Since $N_1 = N_2$, the larger subsystem would have a smaller averaged particle density $\overline{n}_i \equiv N_i/V_i$, and the smaller system a larger $\overline{n}_i$, say $\overline{n}_1 \leq \overline{n}_2$. On the other hand, since the energy supply is homogeneous, that is, proportional to the volume and inverse proportional to $\overline{n}_i$, the larger subsystem would have a higher overall temperature than the smaller subsystem. According to Eq. (2.10), the energy density is the product of local particle density and the local temperature. As a result of this energy supply scheme, a compensation may happen under unequal volumes.

An example of this second phase is shown in Fig. 4.2 (b). As we can see from the figure, the curves are no longer monotonic and cross at 3 points. To see the stabilities between $x_w^{(1)}$ and $x_w^{(2)}$(and equivalently $x_w^{(3)}$), suppose now that the constraint is pushed away from steady states. Two situations can occur: in one case the constraint is between $x_w^{(1)}$ and $x_w^{(2)}$, and the other beyond $x_w^{(2)}$. In both situations, the pressure difference will

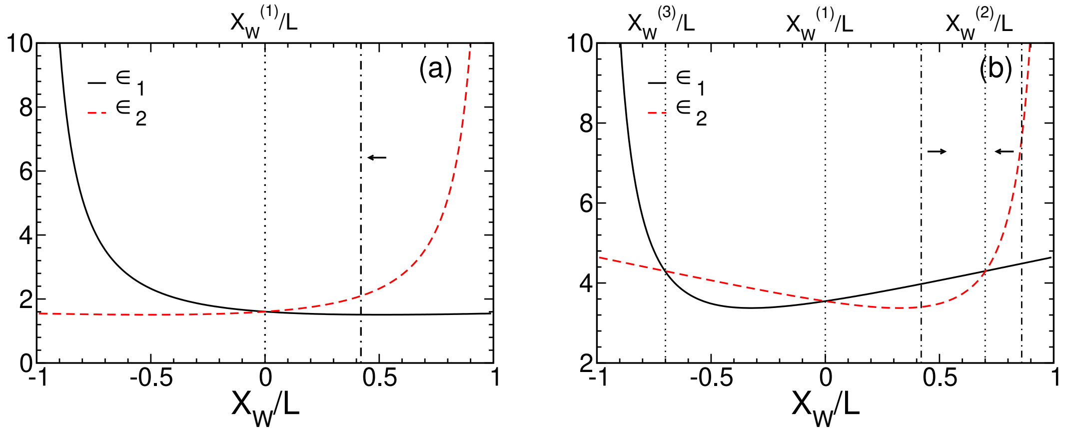

Figure 4.2: Subsystem energy density curves ϵ_i as a function of the normalised position of the constraint X_w/L. Energy supplies are of density $(a)\lambda_1 = 2.0$ and $(b)\lambda_1 = 10.0$, measured in units of kT/L^2. Vertical dashed lines indicates the position of the constraint and the arrow suggests the direction the wall moves. $X_w^{(i)}/L$ denotes the crossing points in each case.

push the constraint towards $x_w^{(2)}$. Due to symmetry, the same argument holds for $x_w^{(3)}$ when the starting point of the constraint is $x_w < 0$. This quick analysis, as indicated in the Fig. 4.2 (b), suggests that $x_w^{(2)}$ and $x_w^{(3)}$ are stable and $x_w^{(1)}$ is unstable.

Now, let us examine the problem quantitatively. The phase diagram $x_w(\widetilde{\lambda}_1)$ (under fixed T, V, N) is plotted in Fig. 4.3 (a). As shown in the figure, as $\widetilde{\lambda}_1$ increases, the system undergoes a phase transition with respect to the stable position of the wall, and the phase transition is continuous. The transition point is at $\lambda_c L^2/kT = 4.55344$. A derivation of this value is shown later. Beyond λ_c, the system exhibits competing steady states, and the stable states are with $X_w \neq 0$.

Further, the total energy of the system $U_{tot} = U_1 + U_2$ for all steady states are plotted in Fig. 4.3(b). Interestingly, the energy of the stable steady states is higher than the unstable steady state.

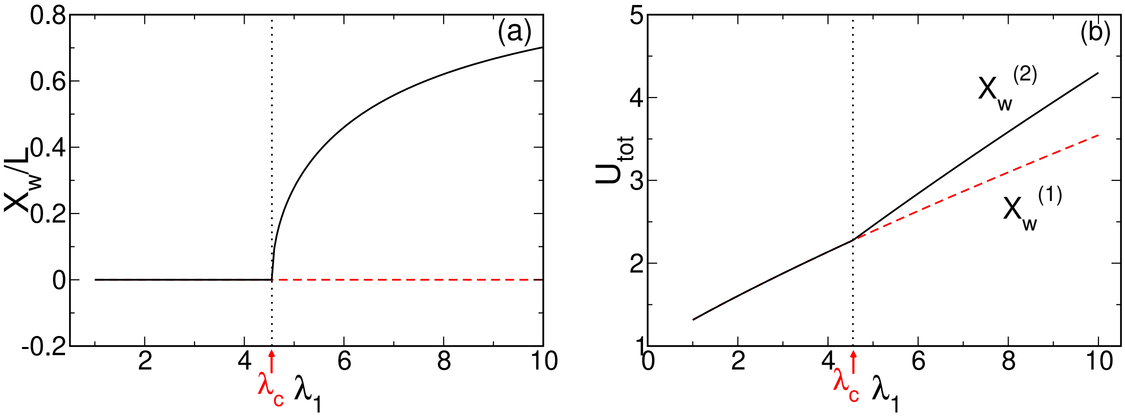

Figure 4.3: (a) Phase diagram in the parameter space $\{X_w, \lambda_1\}$. Stable (unstable) steady states are plotted in black (red). (b) Total Energy of the system U_{tot} as a function of the energy supply density λ_1. Stable (unstable) steady states is denoted as $X_w^{(2)}$ $(X_w^{(1)})$. The vertical lines denote the transition point λ_c. X_w is in units of L, λ_1 in units of kT/L^2 and energy in units of U_{eq}.

4.1.3 Derivation of the Critical Point

As stated previously, the phase transition of the movable wall model with $N_1 = N_2 = N/2$ occurs at $\widetilde{\lambda}_c = \lambda_c L^2/kT = 4.55344$. This value can be derived as follows.

We start by defining a new function, the (negative) differences between the energy densities,

$$G(x_w) \equiv -\Big(g(x_w) - g(-x_w)\Big), \quad g(x_w) \equiv \frac{f\left(\widetilde{\lambda}_1(1+x_w)^2\right)}{1+x_w}. \tag{4.10}$$

The negativity in $G(x_w)$ is not necessary, but it is chosen here to simplify the explanation in a later section. Since the function is odd with respect to x_w, it is sufficient to look at half of the axis, say $x_w \in [0, 1)$.

Consider the range $x_w \geq 0$. For this model, the phase transition occurs when the number of solutions of Eq. (4.9) transit from 1 to 2. Equivalently, this means that the number of times $G(x)$ crosses with the x-axis in this range transit from 1 to 2. Since $G(0) = 0$ and as $x \to 1, G(x) \to \infty$, when $G'(0) > 0, G(x)$ is monotonic and have only one crossing point at $x = 0$; when $G'(0) < 0, G(x)$ will have two crossing points. Therefore, the transition point is $G'(0) = 0 = -2g'(0)$, which is explicitly,

$$\left.\frac{\mathrm{d}g}{\mathrm{d}x}\right|_{x=0} = \frac{1}{2+\widetilde{\lambda}_1} - \frac{\widetilde{\lambda}_1^2 \operatorname{Arctanh}(\sqrt{\widetilde{\lambda}_1/(\widetilde{\lambda}_1+2)})}{(\widetilde{\lambda}_1(\widetilde{\lambda}_1+2))^{3/2}} = 0. \tag{4.11}$$

Solving this implicit equation numerically, we find that $\widetilde{\lambda}_c = \lambda_c L^2/kT \approx 4.55344$.

4.2 Re-examine Hypotheses

Since the movable wall model exhibits multiple competing steady states beyond $\widetilde{\lambda}_c$, it can be employed as a test for variational hypotheses. The methodology has been explained in Sec. 2.1 and we will recount here for quick reference. Explicitly, the minimization hypothesis of a general potential $\mathcal{F}$ indicates that $\mathcal{F}_{\text{stable state}} \leq \{\mathcal{F}_{\text{steady states}}\}$. For the movable wall model, this relation becomes $\mathcal{F}(x_w^{(2)}) = \mathcal{F}(x_w^{(3)}) \leq \mathcal{F}(x_w^{(1)})$.

We first re-examine Hypothesis 2.1.1: the minimization of $\mathcal{T}$, where $\mathcal{T}$ is the ratio of energy storage ΔU to the total heat flow J_U. For the movable wall system, the potential is $\mathcal{T}_{1|2} \equiv (U_1 + U_2 - U_{eq})/(J_{U_1} + J_{U_2})$, where U_{eq} is the equilibrium energy, and J_{U_i} is the total heat flow of subsystem i, as stated before. We will compare the expression of $\mathcal{T}_{1|2}$ at the steady states,

$$\mathcal{T}_{1|2}(x_w^{(i)}) = \frac{U_1(x_w^{(i)}) + U_2(x_w^{(i)}) - U_{eq}}{J_{U_1}(x_w^{(i)}) + J_{U_2}(x_w^{(i)})}. \tag{4.12}$$

Since the total heat flow is constant, the comparison simplifies to a comparison between $U_1(x_w^{(i)}) + U_2(x_w^{(i)})$. Further, since $\epsilon_1(x_w^{(i)}) = \epsilon_2(x_w^{(i)})$ from (4.3), the comparison becomes

$$\epsilon_i(x_w^{(2)}) = \epsilon_i(x_w^{(3)}) \quad \text{and} \quad \epsilon_i(x_w^{(1)}) \tag{4.13}$$

This comparison has been demonstrated in Fig. 4.3 (b) where, contrary to the prediction of the hypothesis, $\epsilon_i(x_w^{(2)}) \geq \epsilon_i(x_w^{(1)})$ for $\widetilde{\lambda}_1 \geq \widetilde{\lambda}_c$. Therefore, Hypothesis 2.1.1 is disproved by the movable wall model.

Next, we re-examine Hypothesis 3.1.1: the minimization of the embedded energy U^*. The expression of U^* at steady states are given by (see Eq. (3.10))

$$U^*_{1|2}(x_w^{(i)}) = U_1(x_w^{(i)}) - J_{U_1}(x_w^{(i)}) \cdot \left.\frac{\partial U_1}{\partial J_{U_1}}\right|_{x_w^{(i)}} + U_2(x_w^{(i)}) - J_{U_2}(x_w^{(i)}) \cdot \left.\frac{\partial U_2}{\partial J_{U_2}}\right|_{x_w^{(i)}}, \tag{4.14}$$

where

$$J_{U_1}(x_w^{(i)}) = \lambda_1 \mathcal{A} L(1 + x_w^{(i)}) = \lambda_1 \mathcal{A} L l_1^{(i)} \quad \text{and} \quad J_{U_2}(x_w^{(i)}) = \lambda_1 \mathcal{A} L(1 - x_w^{(i)}) = \lambda_1 \mathcal{A} L l_2^{(i)}. \tag{4.15}$$

For the movable wall model, the partial derivative with respect to J_{U_1} becomes a partial derivative with respect to $l_i^{(i)}$. Explicitly, the derivative becomes

$$U^*_{1|2} = U_1 - \frac{\partial U_1}{\partial l_1} l_1 + U_2 - \frac{\partial U_2}{\partial l_2} l_2. \tag{4.16}$$

Substituting Eq. (4.7), we obtain

$$\begin{aligned} U^*_{1|2}(x_w) =& \frac{2U_1}{\widetilde{\lambda}_1(1+x_w)^2 + 2}\left(1 + \frac{2U_1}{U_{eq}}\right) - U_1 \\ &+ \frac{2U_2}{\widetilde{\lambda}_1(1-x_w)^2 + 2}\left(1 + \frac{2U_2}{U_{eq}}\right) - U_2. \end{aligned} \tag{4.17}$$

Results of $U^*_{1|2}(x_w^{(i)})$, $i = 1, 2$, are plotted in Fig. 4.4. As we can see, the potential of the stable solutions is smaller than the unstable solution, $U^*(x_w^{(2)}) \leq U^*(x_w^{(1)})$, in accordance with the prediction from the hypothesis. Therefore, the movable wall model supports Hypothesis 3.1.1.

4.3 Various Potentials

It is interesting to see the form of nonequilibrium thermodynamics potentials based on the local equilibrium assumption. In this section, we propose expressions of four nonequilibrium thermodynamic potentials (of an ideal gas system): the steady state entropy S, the Helmholtz like free energy F, the Gibbs like free energy G, and the entropy

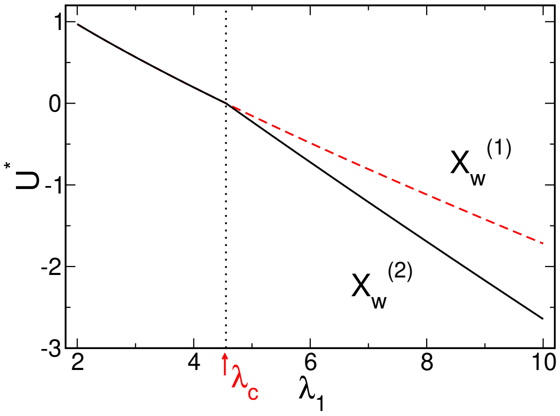

Figure 4.4: Embedded energy U^* at stable (black) and unstable (red) steady state plotted against energy supply density λ_1. The stable (unstable) state is denoted as $X_w^{(2)}$ ($X_w^{(1)}$). The vertical line remarks the transition point λ_c. U^* is in units of U_{eq} and λ_1 in units of kT/L^2.

production rate $\dot{S}$. For each potential, we will check if the expression could be a candidate for variational hypotheses.

The methodology is as follows. We measure these potentials over two models, the paradigm model with the fixed constraint (termed the *fixed wall model*) and the movable wall model. To differentiate between these models, we will denote the position of the fixed constraint as x_1; for the movable wall model, we use x_w as before. Practically, for the fixed wall model, $\mathcal{F}$ and $\mathcal{F}_{1|2}(x_1)$ are measured and compared for each potential $\mathcal{F}$; for the movable wall model, $\mathcal{F}(x_w^{(i)}), i = 1,2,3$ are measured and compared, where $x_w^{(i)}$ are the solutions of Eq. (4.9). Note that we do not presuppose whether the hypothesis is a maximization or minimization hypothesis; instead, we simply check if the predictions from both models agree. The extremum hypothesis and the corresponding predictions are shown in Table 4.1. The last two situations in the table suggest inconsistency, and the form of the potential will be ruled out as a candidate for variational hypotheses.

Hypothesis	Predictions
$\mathcal{F}$ is minimized	$\mathcal{F} \leq \mathcal{F}_{1\|2}(x)$ & $\mathcal{F}(x_w^{(2)}) \leq \mathcal{F}(x_w^{(1)})$
$\mathcal{F}$ is maximized	$\mathcal{F} \geq \mathcal{F}_{1\|2}(x)$ & $\mathcal{F}(x_w^{(2)}) \geq \mathcal{F}(x_w^{(1)})$
– –	$\mathcal{F} \geq \mathcal{F}_{1\|2}(x)$ & $\mathcal{F}(x_w^{(2)}) \leq \mathcal{F}(x_w^{(1)})$
– –	$\mathcal{F} \leq \mathcal{F}_{1\|2}(x)$ & $\mathcal{F}(x_w^{(2)}) \geq \mathcal{F}(x_w^{(1)})$

Table 4.1: Extremum hypotheses and their predictions.

Entropy

First, let us start with the proposition of the steady state entropy S. This expression will be used later to derive the other potentials.

For an ideal gas with a fixed temperature T, volume V and number of particles N, the equilibrium entropy S_{eq} is given by

$$\begin{aligned} S_{eq} &= \frac{5}{2}Nk_B \ln \frac{T_{eq}}{T_0} - Nk_B \ln \frac{P_{eq}}{P_0} + S_0 \\ &= \frac{5}{2}Nk_B \ln \widetilde{T}_{eq} - Nk_B \ln \widetilde{\epsilon}_{eq} + S_0. \end{aligned} \tag{4.18}$$

In this section, we will use $-_{eq}$ to denote variables at the equilibrium state of interest and subscript $-_0$ of a reference equilibrium state; symbol "$\widetilde{-}$" denotes the normalised variable with respect to the reference equilibrium state. For example, in Eq. (4.18), $\widetilde{T}_{eq} = T_{eq}/T_0$ is the normalised temperature with respect to state T_0, V_0, N_0; k_B denotes the Boltzmann condition as usual; P is the pressure, ϵ is the energy density, and the relation $P_{eq}/P_0 = \epsilon_{eq}/\epsilon_0 = \widetilde{\epsilon}_{eq}$ is from Eq. (2.10).

Assuming local equilibrium, we extend Eq. (4.18) to the local entropy density at NESS,

$$s(\vec{r}) = \frac{5}{2}n(\vec{r})k_B \ln \widetilde{T}(\vec{r}) - n(\vec{r})k_B \ln \widetilde{\epsilon} + s_0, \tag{4.19}$$

where $s_0 = S_0/V$, and $\widetilde{T} = T/T_0$, $\widetilde{\epsilon} = \epsilon/\epsilon_0$ as before. We define the nonequilibrium steady state entropy as

$$S \equiv \int_V s(\vec{r}) \mathrm{d}r^3. \tag{4.20}$$

The normalised $s(\vec{r})$ has a simpler form:

$$\widetilde{s}(\vec{r}) \equiv \frac{T_0 s(\vec{r})}{\epsilon_0} = \frac{5}{3}\frac{\widetilde{\epsilon} \ln \widetilde{T}(\vec{r})}{\widetilde{T}(\vec{r})} - \frac{2}{3}\widetilde{n}(\vec{r}) \ln \widetilde{\epsilon} + \widetilde{s}_0, \tag{4.21}$$

where $\widetilde{s}_0 \equiv T_0 s_0/\epsilon_0$, $n(\vec{r})$ is the local number density, and $\widetilde{n} = n/n_0$ is the normalised local number density as usual. This quantity can be integrated to obtain

$$\begin{aligned} \widetilde{S} &\equiv \frac{ST_0}{U_0} = \frac{1}{2}\int_{-1}^{1} \widetilde{s}(\widetilde{x}) \mathrm{d}\widetilde{x} \\ &= \frac{5}{6}\widetilde{\epsilon}\int_{-1}^{1} \mathrm{d}\widetilde{x} \frac{\ln \widetilde{T}(\vec{x})}{\widetilde{T}(\vec{x})} - \frac{2}{3}\ln \widetilde{\epsilon} + \widetilde{s}_0, \end{aligned} \tag{4.22}$$

with $\widetilde{x} = x/L$, same as before. And then, the steady state entropy is retrieved from $S = \widetilde{S}U_0/T_0$.

Similarly, we obtain the steady state entropy under an adiabatic internal constraint $S_{1|2}$. The normalised $\widetilde{S}_{1|2}$ is given by

$$\widetilde{S}_{1|2} \equiv \frac{S_{1|2}T_0}{U_0} = \frac{1}{2}\left(\int_{-1}^{\widetilde{x}_1} \widetilde{s}_1(\widetilde{x}) \mathrm{d}\widetilde{x} + \int_{\widetilde{x}_1}^{1} \widetilde{s}_2(\widetilde{x}) \mathrm{d}\widetilde{x}\right), \tag{4.23}$$

where $\widetilde{x}_1 = x_1/L$ is the normalised position of the adiabatic constraint, same as before. And

$$\widetilde{s}_1(\vec{r}) = \frac{5}{3}\frac{\widetilde{\epsilon}_1 \ln \widetilde{T}_1(\vec{r})}{\widetilde{T}_1(\vec{r})} - \frac{2}{3}\frac{\widetilde{\epsilon}_1 \ln \widetilde{\epsilon}_1}{\widetilde{T}_1(\vec{r})} + \widetilde{s}_0, \tag{4.24}$$

$$\widetilde{s}_2(\vec{r}) = \frac{5}{3}\frac{\widetilde{\epsilon}_2 \ln \widetilde{T}_2(\vec{r})}{\widetilde{T}_2(\vec{r})} - \frac{2}{3}\frac{\widetilde{\epsilon}_2 \ln \widetilde{\epsilon}_2}{\widetilde{T}_2(\vec{r})} + \widetilde{s}_0. \tag{4.25}$$

Therefore,

$$\begin{aligned}\widetilde{S}_{1|2}(\widetilde{x}_1) =& \frac{5}{6}\left(\widetilde{\epsilon}_1 \int_{-1}^{\widetilde{x}_1} \frac{\ln \widetilde{T}_1(\widetilde{x})}{\widetilde{T}_1(\widetilde{x})} \mathrm{d}\widetilde{x} + \widetilde{\epsilon}_2 \int_{\widetilde{x}_1}^{1} \frac{\ln \widetilde{T}_2(\widetilde{x})}{\widetilde{T}_2(\widetilde{x})} \mathrm{d}\widetilde{x}\right) \\ & - \frac{1}{3}\Big((1+\widetilde{x}_1)\ln \widetilde{\epsilon}_1 + (1-\widetilde{x}_1)\ln \widetilde{\epsilon}_2\Big) + \widetilde{s}_0.\end{aligned} \tag{4.26}$$

Then, the steady state entropy of the constrained system is retrieved with $S_{1|2} = \widetilde{S}_{1|2} U_0/T_0$.

Eq. (4.26) is applicable for both models. The value according to each model is obtained by substituting the appropriate temperature profiles and the energy density expressions. For the fixed wall model, $T_i(x)$ is given by Eq. (2.24) and ϵ_i given by Eq. (2.25); for the movable wall model, $T_i(x)$ is the same, ϵ_i is given by Eq. (4.5), and $\widetilde{x}_1 = x_w^{(i)}(\widetilde{\lambda}_1)$ is obtained numerically from Eq. (4.9). In both models, the integrations are obtained numerically.

Results of the comparison are shown in Fig. 4.5. For the fixed wall case, we find that $S \leq S_{1|2}(\widetilde{x}_1)$, and for the movable wall case, $S(x_w^{(2)}) \leq S(x_w^{(1)})$. For the fixed wall model, due to the numerical integration, we were not able to obtain an analytical comparison between S and $S_{1|2}(\widetilde{x}_1)$ and only numerical calculations at several $\widetilde{\lambda}_1$ are performed. Both results are in agreement with the minimization hypothesis (see Table 4.1). Therefore, the proposed expression of steady state entropy can be a candidate for variational hypotheses.

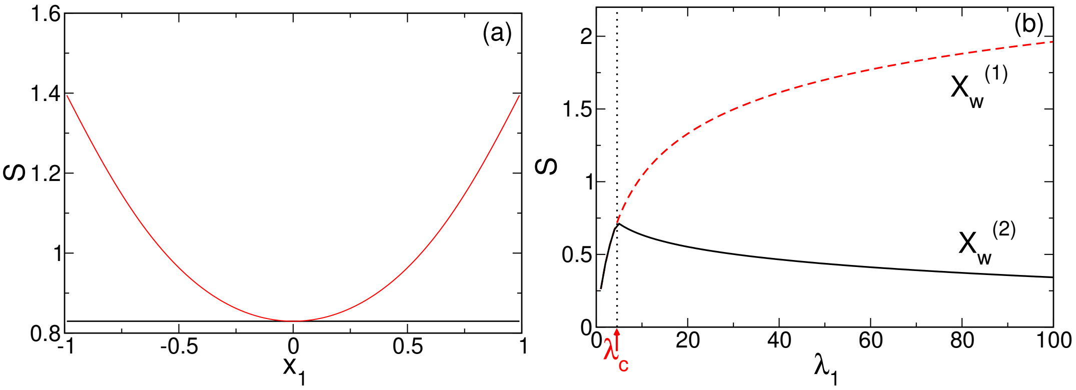

Figure 4.5: (a) Comparison between steady state entropy S of the fixed wall model, with (red) and without (black) constraint. S is plotted against the position of the constraint x_1. The energy supply density is $\lambda_1 = 6.0$. (b) Comparison between S at the stable (black) and unstable (red) steady state, plotted against λ_1. The stable (unstable) state is denoted with $X_w^{(2)}$ $(X_w^{(1)})$. The vertical line denotes the transition point λ_c. S is in units of U_0/T_0, x_1 in units of L, and λ_1 in units of kT_0/L^2.

Helmholtz like Free Energy

Next, we derive an expression of the steady state Helmholtz like free energy F using the local equilibrium assumption. From equilibrium thermodynamics, $F_{eq} = U_{eq} - T_{eq}S_{eq}$. Local equilibrium suggests

$$F = \epsilon V - \int_V T(\vec{r})s(\vec{r})\mathrm{d}r^3. \tag{4.27}$$

Once again, the normalised $\widetilde{F}$ has a simpler form

$$\widetilde{F} \equiv \frac{F}{U_0} = \widetilde{\epsilon} - \frac{1}{2}\int_{-1}^{1} \widetilde{T}(\widetilde{x})\widetilde{s}(\widetilde{x})\mathrm{d}\widetilde{x}, \tag{4.28}$$

where $\widetilde{s}(\widetilde{x})$ is given by Eq. (4.21) and

$$\widetilde{T}(\widetilde{x})\widetilde{s}(\widetilde{x}) = \frac{5}{3}\widetilde{\epsilon}\ln\widetilde{T}(\widetilde{x}) - \frac{2}{3}\widetilde{\epsilon}\ln\widetilde{\epsilon} + \widetilde{T}(\widetilde{x})\widetilde{s}_0. \tag{4.29}$$

Substituting the appropriate $T(x)$ and ϵ (Eqs. (2.21) and (2.22)), we obtain

$$\widetilde{F} = \frac{13}{3}\widetilde{\epsilon} + \frac{2}{3}\widetilde{\epsilon}\ln\widetilde{\epsilon} - \frac{5}{3}(\widetilde{\lambda}_1 + 2) - \widetilde{s}_0(\frac{\widetilde{\lambda}_1}{3} + 1). \tag{4.30}$$

And we retrieve $F = U_0\widetilde{F}$.

For the constrained system, the normalised $\widetilde{F}_{1|2}$ is given by

$$\begin{aligned}\widetilde{F}_{1|2} \equiv& \frac{F_1 + F_2}{U_0} \\ =& \frac{1}{2}\Big(\widetilde{\epsilon}_1(1+\widetilde{x}_1) + \widetilde{\epsilon}_2(1-\widetilde{x}_1)\Big) \\ &- \frac{1}{2}\left(\int_{-1}^{\widetilde{x}_1}\widetilde{T}_1(\widetilde{x})\widetilde{s}_1(\widetilde{x})\mathrm{d}\widetilde{x} + \int_{\widetilde{x}_1}^{1}\widetilde{T}_2(\widetilde{x})\widetilde{s}_2(\widetilde{x})\mathrm{d}\widetilde{x}\right).\end{aligned} \tag{4.31}$$

where $\widetilde{s}_1(x)$ and $\widetilde{s}_2(x)$ are given by Eqs. (4.24) and (4.25), respectively. Along with Eqs. (2.24) and (2.25), the expression of the fixed wall model is

$$\begin{aligned}\widetilde{F}_{1|2}(\widetilde{x}_1) =& \frac{13}{6}\Big(\widetilde{\epsilon}_1(1+\widetilde{x}_1) + \widetilde{\epsilon}_2(1-\widetilde{x}_1)\Big) \\ &+ \frac{1}{3}\Big((1+\widetilde{x}_1)\widetilde{\epsilon}_1\ln\widetilde{\epsilon}_1 + (1-\widetilde{x}_1)\widetilde{\epsilon}_2\ln\widetilde{\epsilon}_2\Big) \\ &- \frac{5}{3}(\widetilde{\lambda}_1 + 2 + 3\widetilde{\lambda}_1\widetilde{x}_1^2) - \widetilde{s}_0\left(\frac{\widetilde{\lambda}_1}{3} + \frac{\widetilde{\lambda}_1\widetilde{x}_1^2}{3} + 1\right).\end{aligned} \tag{4.32}$$

And if we substitute ϵ_i with Eq. (4.5) and solutions $x_w^{(i)}$, the corresponding expression of the movable wall case is obtained,

$$\begin{aligned}\widetilde{F}_{1|2}(x_w^{(1)}) &= \frac{13}{3}\widetilde{\epsilon}_1^{(1)} + \frac{2}{3}\widetilde{\epsilon}_1^{(1)}\ln\widetilde{\epsilon}_1^{(1)} - \frac{5}{3}(\widetilde{\lambda}_1 + 2) - \widetilde{s}_0(\frac{\widetilde{\lambda}_1}{3} + 1),\\ \widetilde{F}_{1|2}(x_w^{(2)}) &= \frac{13}{3}\widetilde{\epsilon}_1^{(2)} + \frac{2}{3}\widetilde{\epsilon}_1^{(2)}\ln\widetilde{\epsilon}_1^{(2)} - \frac{5}{3}(\widetilde{\lambda}_1 + \widetilde{\lambda}_1\widetilde{x}_1^2 + 2) - \widetilde{s}_0(\frac{\widetilde{\lambda}_1}{3} + \widetilde{\lambda}_1\widetilde{x}_1^2 + 1).\end{aligned} \tag{4.33}$$

Results of the comparison are shown in Fig. 4.6. Like before, only numerical inspections are performed for the fixed wall model. As we can see from the figure, $F \geq F(\widetilde{x}_1)$ and $F(x_w^{(2)}) \leq F(x_w^{(1)})$. According to Table 4.1, these results are contradictory to each other. Therefore, the proposed expression of F cannot be a candidate for variational hypotheses.

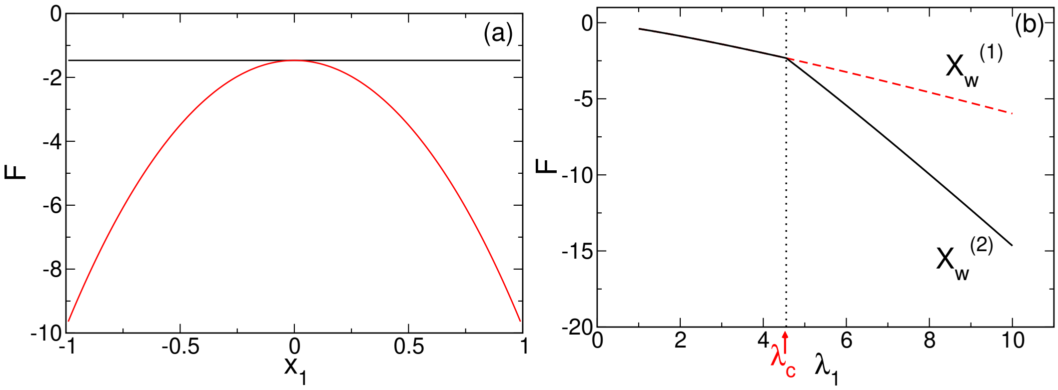

Figure 4.6: (a) Comparison between Helmholtz like free energy F of the fixed wall model, with (red) and without (black) constraint. F is plotted against the constraint position x_1. The energy supply density $\lambda_1 = 6.0$. (b) Comparison between F of the movable wall model, at the stable (black) and unstable (red) steady states, plotted against λ_1. The stable (unstable) state is denoted with $X_w^{(2)}$ $(X_w^{(1)})$. The vertical line denotes the transition point λ_c. F is in units of U_0, x_1 in units of L, and λ_1 in units of kT_0/L^2.

Gibbs Like Free Energy

Our proposed expression of the steady state Gibbs like free energy G is relatively simple. From equilibrium thermodynamics, the Gibbs free energy is given by

$$G_{eq} = U_{eq} + P_{eq}V_{eq} - T_{eq}S_{eq} = F_{eq} + P_{eq}V_{eq}, \tag{4.34}$$

Following the local equilibrium assumption, G is simply

$$G = F + PV. \tag{4.35}$$

And for the constrained system, we define

$$G_{1|2} = F_{1|2} + P_1V_1 + P_2V_2. \tag{4.36}$$

The normalised $\widetilde{G}$ has a simplified form. For the unconstrained system, this is

$$\widetilde{G} \equiv \frac{G}{U_0} = \widetilde{F} + \frac{2}{3}\widetilde{\epsilon}. \tag{4.37}$$

where $\widetilde{F}$ is given by Eq. (4.28). Then, for the fixed wall model with a constraint at $\widetilde{x}_1$

$$\widetilde{G}_{1|2}(\widetilde{x}_1) \equiv \frac{\widetilde{G}_{1|2}}{U_0} = \widetilde{F}_{1|2}(\widetilde{x}_1) + \frac{1}{3}\Big(\widetilde{\epsilon}_1(1+\widetilde{x}_1) + \widetilde{\epsilon}_2(1-\widetilde{x}_1)\Big). \tag{4.38}$$

where $\widetilde{F}_{1|2}(\widetilde{x}_1)$ is given by Eq. (4.32). And for the movable wall model, the expression becomes

$$\widetilde{G}_{1|2}(x_w^{(i)}) = \widetilde{F}_{1|2}(x_w^{(i)}) + \frac{2}{3}\widetilde{\epsilon}^{(i)}, \tag{4.39}$$

where $\widetilde{F}_{1|2}(x_w^{(i)})$ is given by Eq. (4.33). Finally, $G = \widetilde{G}U_0$ and $G_{1|2} = \widetilde{G}_{1|2}U_0$.

Comparisons for G are shown in Fig. 4.7. This figure is obtained from Fig. 4.6, adjusted with an additional term (P for $\widetilde{G}$ and P_i for $\widetilde{G}_{1|2}$). Similar to the case of F, the results from the two models contradict each other. Therefore, the proposed expression of G is also ruled out to be a candidate for variational hypotheses.

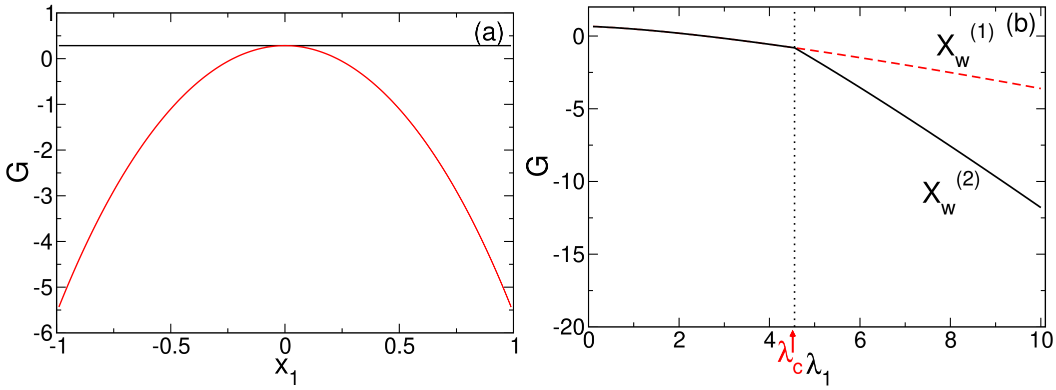

Figure 4.7: (a) Comparison between Gibbs like free energy G of the fixed wall model, with (red) and without (black) constraint. G is plotted against the constraint position x_1. The energy supply density $\lambda_1 = 6.0$. (b) Comparison between G of the movable wall model, at the stable (black) and unstable (red) steady states, plotted against λ_1. The stable (unstable) state is denoted with $X_w^{(2)}$ ($X_w^{(1)}$). The vertical line denotes the transition point λ_c. G is in units of U_0, x_1 in units of L, and λ_1 in units of kT_0/L^2.

Entropy Production Rate

Finally, we derive an expression of the entropy production rate of the ideal gas. From Eq. (1.40), the entropy production rate is given by the sum of the product of flux and affinity pairs. For the two test models, the pair is the heat flux density $J_E = -k\partial_x T(x)$ (from Fourier's law (1.51)), and the local affinity due to the temperature gradient $\mathcal{F}_E =$

$\partial_x T^{-1}(x)$. Therefore, the local entropy production rate (density) is

$$\sigma_s = J_E \mathcal{F}_E = \frac{\partial}{\partial_x}\left(\frac{1}{T(x)}\right)\left(-k\frac{\partial}{\partial_x}T(x)\right) = k\left(\frac{\partial_x T(x)}{T(x)}\right)^2. \tag{4.40}$$

And the total entropy production rate is given by

$$\dot{S}_{tot} \equiv \int_V \sigma_s \mathrm{d}^3 r. \tag{4.41}$$

The total entropy production rate per unit volume has a simpler form,

$$\overline{\sigma_s} \equiv \frac{\dot{S}_{tot}}{V} = \frac{1}{2L}\int_{-L}^{L}\sigma_s dx. \tag{4.42}$$

By substituting Eq. (2.21) into (4.40), we obtain

$$\overline{\sigma_s} = \frac{\lambda_1}{T_0}(1-\frac{1}{\widetilde{\epsilon}}) = \lambda_1(\beta_0 - \overline{\beta}), \tag{4.43}$$

where

$$\overline{\beta} \equiv \frac{1}{V}\int_V \frac{\mathrm{d}x}{T(x)} \quad \text{and} \quad \beta_0 \equiv \frac{1}{T_0}. \tag{4.44}$$

And the total entropy production rate is $\dot{S}_{tot} = \overline{\sigma_s}V$.

Similarly, $\overline{\sigma_s}$ for the constrained systems with a constraint at x_1 is given by

$$\overline{\sigma_s}_{1|2}(x_1) = \frac{1}{2L}\left(\int_{-L}^{x_1}\sigma_s^1 \mathrm{d}x + \int_{x_1}^{L}\sigma_s^2 \mathrm{d}x\right), \tag{4.45}$$

where $\overline{\sigma_s}^i$ is the subsystem entropy production rate. Explicitly, for the fixed wall model

$$\begin{aligned}\overline{\sigma_s}_{1|2}(\widetilde{x}_1) &= \frac{\lambda_1}{T_0}\left(\frac{1+\widetilde{x}_1}{2}(1-\frac{1}{\widetilde{\epsilon}_1}) + \frac{1-\widetilde{x}_1}{2}(1-\frac{1}{\widetilde{\epsilon}_2})\right)\\ &= \lambda_1\left(\beta_0 - \frac{1}{2}(1+\widetilde{x}_1)\overline{\beta}_1 - \frac{1}{2}(1-\widetilde{x}_1)\overline{\beta}_2\right),\end{aligned} \tag{4.46}$$

where

$$\overline{\beta_1} = \frac{1}{L+x_1}\left(\int_{-L}^{x_1}\frac{dx}{T_1(x)}\right) = \frac{1}{\widetilde{\epsilon}_1} \quad \text{and} \quad \overline{\beta_2} = \frac{1}{L-x_1}\left(\int_{x_1}^{L}\frac{dx}{T_2(x)}\right) = \frac{1}{\widetilde{\epsilon}_2}. \tag{4.47}$$

And for the movable wall model,

$$\begin{aligned}\overline{\sigma_s}_{1|2}(x_w^{(i)}) &= \frac{\lambda_1}{T_0}(1-\frac{1}{\widetilde{\epsilon}^{(i)}})\\ &= \lambda_1\left(\beta_0 - (1+\widetilde{x}_w^{(i)})\overline{\beta_1}^{(i)}\right) = \lambda_1\left(\beta_0 - (1-\widetilde{x}_w^{(i)})\overline{\beta_2}^{(i)}\right).\end{aligned} \tag{4.48}$$

The last equal sign comes from Eq. (4.3). Finally, we retrieve $\dot{S}_{tot}^{1|2} = \overline{\sigma_s}_{1|2}V$.

A comparison of the total entropy production rate for both models is shown in Fig. 4.8. As we can see, $\dot{S}_{tot} \leq \dot{S}^{1|2}_{tot}(x_1)$ and $\dot{S}^{1|2}_{tot}(x_w^{(2)}) \geq \dot{S}^{1|2}_{tot}(x_w^{(1)})$. According to Table 4.1, the results suggest a contradiction. Therefore, the proposed expression of $\dot{S}_{tot}$ is ruled out as a candidate for variational hypotheses.

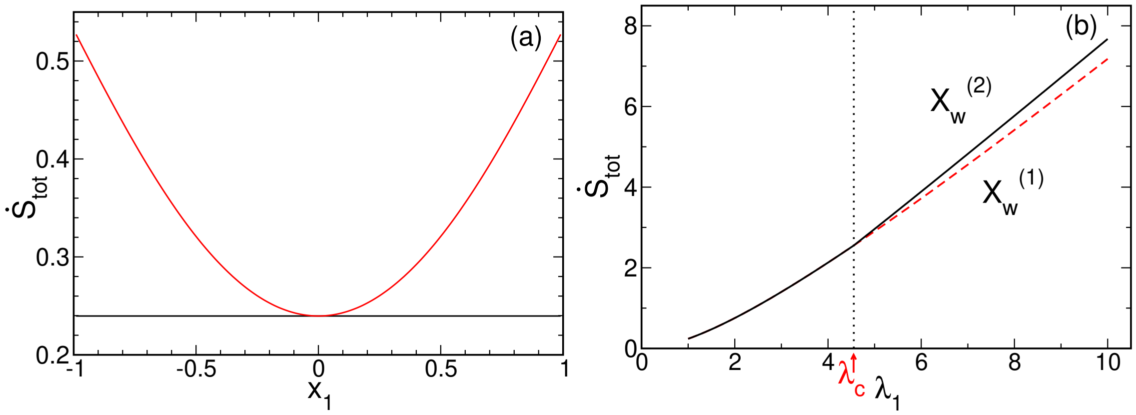

Figure 4.8: (a) Comparison between the entropy production rate $\dot{S}_{tot}$ of the fixed wall model, with (red) and without (black) constraint. $\dot{S}_{tot}$ is plotted against the constraint position x_1. The energy supply density is $\lambda_1 = 1.0$. (b) Comparison between $\dot{S}_{tot}$ of the movable wall model, at the stable (black) and unstable (red) steady states, plotted against λ_1. The stable (unstable) state is denoted with $X_w^{(2)}$ $(X_w^{(1)})$. The vertical line denotes the transition point λ_c. $\dot{S}_{tot}$ is in unit volume, x_1 in units of L, and λ_1 in units of kT_0/L^2.

4.4 Summary and Conclusion

In this chapter, we have introduced and analysed the movable wall model: an ideal gas driven by a homogeneous bulk energy supply, inserted with a movable adiabatic wall. For the simplest case where the subsystems have an equal number of particles, this model exhibits a second order nonequilibrium phase transition; beyond the transition point λ_c, the system exhibits three competing steady states. To our knowledge, this is the simplest model that exhibits nonequilibrium phase transitions and competing steady states. Moreover, the system can be solved analytically. Therefore, this model can be used as a paradigm model of nonequilibrium phase transitions.

Using the competing steady states, we re-examine Hypotheses 2.1.1 and Hypothesis 3.1.1 in Sec. 4.2. The model supports the latter, but not the former. In Sec. 4.3, we have also derived various nonequilibrium thermodynamic potentials using the local equilibrium assumption. These potentials are the steady state entropy S, the Helmholtz like free energy F, the Gibbs like free energy G, and the entropy production rate $\dot{S}_{tot}$. We have also checked if these expressions can be used as candidates for variational principles. To see this, we have measured these potentials in both the fixed wall model and the movable wall model, and then checked for consistency. The consistency test ruled out the last three expressions, leaving only S.

The movable wall model can be extended to more general conditions, for example, $N_1 \neq N_2$ and $\lambda_1 \neq \lambda_2$. These additional degrees of freedom introduce variations to the model. Further studies are needed to examine the existence and condition of phase transition, the corresponding transition points, the number of competing states, and much more.

Chapter 5

Nonequilibrium Steady State Potential: The Final Hypothesis

In this chapter, we propose a nonequilibrium state function B and the hypothesis that B is minimized for nonequilibrium steady states (NESS). At the time of preparing this thesis, this is our latest hypothesis. This potential B is analogous to the equilibrium Helmholtz free energy. We will give the definition of this potential and its justification in Sec. 5.1. In Sec. 5.2, we will analyse the potential B of an ideal gas under homogeneous energy supply and of the movable wall model. We will show that this potential correctly predicts the stable steady states for the movable wall model.

5.1 Potential B and the Last Hypothesis

Consider a typical nonequilibrium system, a closed system with a fixed number of particles N and volume V, placed in a heat bath of temperature T, and driven to nonequilibrium steady states with an external control parameter λ. For such an open system, we propose a nonequilibrium state function B that is minimized in NESS.

The development of this nonequilibrium state function is based on a series of postulates. First, we postulate the existence of a state function B, such that it is minimized for nonequilibrium steady states. Moreover, the relevant variables are postulated to be the thermodynamic variables T, V, N, same as in equilibrium thermodynamics, and the control parameter λ to account for nonequilibrium. To state formally,

Postulate 5.1.1. There exists a nonequilibrium state function B of thermodynamic variables T, V, N and the control parameter λ, $B(T, V, N, \lambda)$, such that it is minimized for nonequilibrium steady states.

The author would like to remark that, in the limiting case where the control parameter is 0, this potential must reduce to the equilibrium Helmholtz free energy,

$$\lim_{\lambda \to 0} B(T, V, N, \lambda) = F_{eq}(T, V, N). \tag{5.1}$$

This correspondence is a necessary and important requirement of any proposition of a nonequilibrium potential of a closed system. This requirement follows from the criteria that any new hypothesis must agree with previously established theories. In this case, from equilibrium thermodynamics, it is established that for a closed system of a fixed T, V, N, $F_{eq}(T, V, N)$ is minimized. Therefore, Eq. (5.1) is a necessary condition.

Second, we postulate the differential form of the potential in analogous to the equilibrium free energy, formally stated as,

Postulate 5.1.2. The state function $B(T, V, N, \lambda)$ satisfies

$$\mathrm{d}B(T, V, N, \lambda) = -S\mathrm{d}T - P\mathrm{d}V + \mu\mathrm{d}N - X\mathrm{d}\lambda \tag{5.2}$$

where P, S, μ, and X are state functions conjugate to V, T, N, and λ, respectively.

In other words, this postulate also contains, implicitly, the definitions of steady state pressure P, entropy S, and chemical potential μ,

$$-P(T, V, N, \lambda) \equiv \frac{\partial B}{\partial V}, \tag{5.3}$$

$$-S(T, V, N, \lambda) \equiv \frac{\partial B}{\partial T}, \tag{5.4}$$

$$\mu(T, V, N, \lambda) \equiv \frac{\partial B}{\partial N}. \tag{5.5}$$

The new variable X is purely due to nonequilibrium and has no equilibrium counterpart. From the postulate, this variable satisfies the relation

$$-X(T, V, N, \lambda) = \frac{\partial B}{\partial \lambda}. \tag{5.6}$$

Note that the first three terms of Eq. (5.2) are analogous to the differential form of the equilibrium free energy $\mathrm{d}F_{eq}(T, V, N) = -S_{eq}\mathrm{d}T - P_{eq}\mathrm{d}V + \mu_{eq}\mathrm{d}N$.

Finally, we propose the form of X. Previously in Chapters 2 and 3, we have extensively studied energy storage and the total heat flow, and defined $\mathcal{T}$. We have also derived the form of steady state energy and the total heat flow, and defined U^*. These quantities show minimization for certain models. Inspired by these results, we propose the form of X as follows,

Postulate 5.1.3. The form of X is given by

$$X(T, V, N, \lambda) \propto \frac{U - U_{eq}}{\lambda}. \tag{5.7}$$

In this case, X is linked to the previous hypotheses: the energy storage still plays a key role, and the external control parameter λ is related to the total heat flow. The coefficient is obtained through an argument of consistency which will be described in the next section.

5.2 Applications in Ideal Gas

In this section, using the ideal gas model, we derive the expressions of the potential $B(T, V, N, \lambda)$ and $X(T, V, N, \lambda)$ from the above postulates. Then, from these expressions, we perform consistency checks using the Maxwell relations of B. Finally, we demonstrate the use of B in the movable wall model. We will show that the minimization of B correctly predicts the stable steady states.

5.2.1 Expressions

Consider an ideal gas model placed under a homogeneous bulk energy supply of density λ. Like before, the model is of a fixed V and N; the area of the left and right boundary is $\mathcal{A}$, and the length is $2L$; it is placed in a heat bath of T; it has a heat conductivity of k. A schematic plot of the system can be found in Fig. 2.1.

For this model, since the energy is supplied through the whole volume, the external control parameter λ in B is identified as the energy supply density, and it coincides with the total heat flow per volume, $\lambda = J_U/V$. The steady state energy of the system is $U = \epsilon V$, where ϵ is the energy density, given by Eq. (2.22). We rewrite the expression of U as follows,

$$U = U_{eq} f(\lambda \cdot \frac{L^2}{kT}) = \frac{3}{2} N k_B T f(\lambda \cdot \frac{L^2}{kT}), \tag{5.8}$$

and f is given by Eq. (4.6). The author would like to remark that, here, the variable of f is separated to λ and L^2/kT. This separation is chosen to reflect that λ is the external control parameter; and the coefficient L^2/kT are independent parameters that are either of the intrinsic properties of the system (k, L), or of the environment that is not changed (T).

From Eq. (5.6) of Postulate 5.1.2, B can be obtained by

$$B(T, V, N, \lambda) = B(T, V, N, 0) - \int_0^\lambda X \mathrm{d}\lambda'. \tag{5.9}$$

As stated in Eq. (5.1), we have $B(T, V, N, 0) = F_{eq}(T, V, N)$. Therefore,

$$B(T, V, N, \lambda) = F_{eq}(T, V, N) - \int_0^\lambda X \mathrm{d}\lambda'. \tag{5.10}$$

Alternatively, the above expression can be obtained from the Maxwell relations of B. In analogous to the Maxwell relations of the equilibrium thermodynamics, there are in total six Maxwell relations of $B(T, V, N, \lambda)$ from four variables T, V, N, and λ. We use the Maxwell relation involving T and λ,

$$\frac{\partial^2 B}{\partial T \partial \lambda} = \frac{\partial^2 B}{\partial \lambda \partial T} \quad \Leftrightarrow \quad \frac{\partial S}{\partial \lambda} = \frac{\partial X}{\partial T}. \tag{5.11}$$

The second part of the relation comes from Eqs. (5.4) and (5.6). Hence, B is given by

$$\begin{aligned} B(T,V,N,\lambda) &= -\int_{T_{ref}}^{T} S\mathrm{d}T' + B(T_{ref},V,N,\lambda), \\ &= -\int_{T_{ref}}^{T} \mathrm{d}T' \left(\int_0^{\lambda} \frac{\partial X}{\partial T'} \mathrm{d}\lambda' + S_{eq}(T',V,N) \right) + B(T_{ref},V,N,\lambda). \end{aligned} \tag{5.12}$$

Exchange the order of integration, and the above expression becomes

$$\begin{aligned} B(T,V,N,\lambda) - B(T_{ref},V,N,\lambda) =& F_{eq}(T,V,N) - F_{eq}(T_{ref},V,N) \\ & - \int_0^{\lambda} \Big(X(T,V,N,\lambda') - X(T_{ref},V,N,\lambda') \Big) \mathrm{d}\lambda'. \end{aligned} \tag{5.13}$$

And therefore, Eq. (5.10) is retrieved.

The form of B in Eq. (5.10) can be interpreted as follows. Any state (T,V,N,λ) can be viewed as the combination of two independent processes. The first step is to move from an arbitrary reference state in equilibrium, perhaps $(T_{ref},V_{ref},N_{ref})$, to the equilibrium state (T,V,N) through a quasi-static process. This first step accounts for the component $F_{eq}(T,V,N)$ in Eq. (5.10). The second step is to move from the equilibrium (T,V,N), or $(T,V,N,0)$, to (T,V,N,λ) through a slow nonequilibrium process. The process is such that, at any time, the system is assumed to be in a nonequilibrium steady state, and each small change in λ results in an increment in the potential of $-X\mathrm{d}\lambda$. This second step accounts for the second component in Eq. (5.10).

The expression of pressure is known from Eq. (2.10): $P = 2U/3V$. On the other hand, the Maxwell relation involving P and X provides a link between them,

$$\frac{\partial^2 B}{\partial V \partial \lambda} = \frac{\partial^2 B}{\partial \lambda \partial V} \quad \Leftrightarrow \quad \frac{\partial P}{\partial \lambda} = \frac{\partial X}{\partial V}. \tag{5.14}$$

Using this relation, P can be expressed as

$$P(T,V,N,\lambda) = \int_0^{\lambda} \frac{\partial X}{\partial V} \mathrm{d}\lambda' + P_{eq}(T,V,N) \tag{5.15}$$

By demanding that Eq. (5.15) is equivalent to $2U/3V$, we identify the coefficient of X of this model as $1/3$

$$X = \frac{1}{3} \left(\frac{U - U_{eq}}{\lambda} \right). \tag{5.16}$$

With the explicit expression of X, the expression of the steady state entropy S can be obtained from Eq. (5.11),

$$\begin{aligned} S(T,V,N,\lambda) =& \int_0^{\lambda} \frac{\partial X}{\partial T} \mathrm{d}\lambda' + S_{eq}(T,V,N), \\ =& \frac{Nk_B}{2} \int_0^{\lambda} \frac{f(\lambda' \frac{L^2}{kT}) - 1}{\lambda'} \mathrm{d}\lambda' - \frac{Nk_B}{2} \left(f(\lambda' \frac{L^2}{kT}) - 1 \right) \\ &+ S_{eq}(T,V,N). \end{aligned} \tag{5.17}$$

And from the Maxwell relation involving μ and X,

$$\frac{\partial^2 B}{\partial N \partial \lambda} = \frac{\partial^2 B}{\partial \lambda \partial N} \quad \Leftrightarrow \quad -\frac{\partial \mu}{\partial \lambda} = \frac{\partial X}{\partial N}, \tag{5.18}$$

we obtain the last state function

$$\begin{aligned} \mu(T,V,N,\lambda) =& -\int_0^{\lambda} \frac{\partial X}{\partial N} \mathrm{d}\lambda' + \mu_{eq}(T,V,N), \\ =& \frac{k_B T}{2} \int_0^{\lambda} \frac{f(\lambda' \frac{L^2}{kT}) - 1}{\lambda'} \mathrm{d}\lambda' + \mu_{eq}(T,V,N). \end{aligned} \tag{5.19}$$

With expressions (5.10), (5.15), (5.16), (5.17), and (5.19), we perform consistency checks. First, it is easy to show that these expressions are in accordance with their definitions from Postulate 5.1.2. Second, we use the rest of the Maxwell relations

$$\frac{\partial^2 B}{\partial T \partial V} = \frac{\partial^2 B}{\partial V \partial T} \quad \Leftrightarrow \quad \frac{\partial S}{\partial V} = \frac{\partial P}{\partial T}, \tag{5.20}$$

$$\frac{\partial^2 B}{\partial T \partial N} = \frac{\partial^2 B}{\partial N \partial T} \quad \Leftrightarrow \quad -\frac{\partial S}{\partial N} = \frac{\partial \mu}{\partial T}, \tag{5.21}$$

$$\frac{\partial^2 B}{\partial V \partial N} = \frac{\partial^2 B}{\partial N \partial V} \quad \Leftrightarrow \quad -\frac{\partial P}{\partial N} = \frac{\partial \mu}{\partial V}. \tag{5.22}$$

to check the validity of these mixed derivatives. And indeed,

$$\frac{\partial S}{\partial V} = \frac{\partial P}{\partial T} = \frac{Nk_B f}{V} - \frac{Nk_B}{V} \frac{\lambda L^2}{kT} \frac{\mathrm{d}f}{\mathrm{d}y}, \tag{5.23}$$

$$-\frac{\partial S}{\partial N} = \frac{\partial \mu}{\partial T} = -\frac{k_B}{2} \int_0^{\lambda} \frac{f-1}{\lambda'} \mathrm{d}\lambda' + \frac{k_B}{2}(f-1) + \frac{\partial \mu_{eq}}{\partial T}, \tag{5.24}$$

$$-\frac{\partial P}{\partial N} = \frac{\partial \mu}{\partial V} = -\frac{k_B T}{V} f, \tag{5.25}$$

where $y = \lambda L^2/kT$, and we have used the equilibrium Maxwell relation $\partial_N S_{eq} = -\partial_T \mu_{eq}$. This analysis shows that the expressions of the state functions are consistent with the Maxwell relations. Third, note that as $\lambda \to 0$, $f \to 1$. It is then obvious to check that, as $\lambda \to 0$, the correct equilibrium values of these five expressions are retrieved. These checks further support the postulates and the expressions.

From Eqs. (5.8), (5.10), (5.16), and (5.17), we also obtain the integral form of B

$$B = U - TS - 4X\lambda. \tag{5.26}$$

This form, again, turns out to be analogous to the Helmholtz free energy where $F_{eq} = U_{eq} - TS_{eq}$. The additional term is the conjugate pair due to nonequilibrium $-X\lambda$ with a coefficient 4.

5.2.2 Movable Wall Model and Minima of B

Here, we demonstrate the use of the state function B, given by Eq. (5.10), with the full expression of X, given by Eq. (5.16), in the movable wall model.

For the movable wall model with an internal constraint at X_w, the potential B is given by

$$B(T, V, N_1, N_2, X_w, \lambda) = F_{eq}(T, V, N_1, N_2, X_w) - \int_0^{\lambda} X(T, V, N, \lambda, X_w)\mathrm{d}\lambda', \tag{5.27}$$

where

$$X(T, V, N_1, N_2, X_w, \lambda) = \frac{1}{3}\frac{U_1 + U_2 - U_{eq}}{\lambda}. \tag{5.28}$$

The subsystem energy is given by Eq. (4.7) and is now written as

$$\begin{aligned} U_1 &= U_{1,eq} f(\lambda \cdot \frac{L_1^2}{kT}) = \frac{3}{2} N_1 k_B T f(\lambda \cdot \frac{L_1^2}{kT}), \\ U_2 &= U_{2,eq} f(\lambda \cdot \frac{L_2^2}{kT}) = \frac{3}{2} N_2 k_B T f(\lambda \cdot \frac{L_2^2}{kT}), \end{aligned} \tag{5.29}$$

where U_{eq} and $U_{i,eq}$ are the system and subsystem energy in equilibrium, L_i is the length of the subsystem with $L_1 = L + X_w$ and $L_2 = L - X_w$.

The extrema of B are obtained from

$$\left.\frac{\partial B}{\partial X_w}\right|_{X_w^*} = 0. \tag{5.30}$$

which is separated into two parts. First, the Helmholtz free energy is given by

$$F_{eq}(T, V, N_1, N_2, X_w) = \frac{3}{2} N k_B T - T\left(S_{1,eq} + S_{2,eq}\right) \tag{5.31}$$

From equilibrium thermodynamics, we know that $\partial F_{eq}/\partial V = -P_{eq} = -2U_{eq}/3V$. Hence, the first part of the partial derivative is

$$\frac{\partial}{\partial X_w} F_{eq}(T, V, N_1, N_2, X_w) = -\left(\frac{N_1 k_B T}{L + X_w} - \frac{N_2 k_B T}{L - X_w}\right). \tag{5.32}$$

Second, the partial derivative containing X is given by

$$\int_0^\lambda \frac{\partial X}{\partial X_w}\mathrm{d}\lambda' = \frac{N_1 k_B T}{2}\int_0^\lambda \frac{\partial f(\Lambda_+)}{\partial X_w}\frac{\mathrm{d}\lambda'}{\lambda'} + \frac{N_2 k_B T}{2}\int_0^\lambda \frac{\partial f(\Lambda_-)}{\partial X_w}\frac{\mathrm{d}\lambda'}{\lambda'}. \tag{5.33}$$

where $\Lambda_+ = \lambda L_1^2/kT$ and $\Lambda_- = \lambda L_2^2/kT$. Using the chain rule and exchange of variables, the partial derivative is now

$$\frac{\partial f}{\partial X_w}\frac{\mathrm{d}\lambda}{\lambda} = \frac{\mathrm{d}f}{\mathrm{d}\Lambda_\pm}\frac{\partial \Lambda_\pm}{\partial X_w}\frac{\mathrm{d}\Lambda_\pm}{\lambda L_i^2/kT} = \frac{2}{L_i}\mathrm{d}f. \tag{5.34}$$

Eq. (5.33) then becomes

$$\begin{aligned}\int_0^\lambda \frac{\partial X}{\partial X_w}\mathrm{d}\lambda' &= \left(\frac{N_1 k_B T f(\Lambda_+)}{L+X_w} - \frac{N_2 k_B T f(\Lambda_-)}{L-X_w}\right) - \left(\frac{N_1 k_B T}{L+X_w} - \frac{N_2 k_B T}{L-X_w}\right), \\ &= A(P_1 - P_2) - \left(\frac{N_1 k_B T}{L+X_w} - \frac{N_2 k_B T}{L-X_w}\right).\end{aligned} \tag{5.35}$$

The first two terms have been identified as P_1 and P_2, since from Eq. (5.29),

$$P_1 = \frac{N_1 k_B T}{V_1} f(\lambda\frac{(L+X_w)^2}{kT}), \tag{5.36}$$

$$P_2 = \frac{N_2 k_B T}{V_2} f(\lambda\frac{(L-X_w)^2}{kT}). \tag{5.37}$$

Together with Eq. (5.32), the extrema of B is equivalent to the condition of matching pressure

$$\left.\frac{\partial B}{\partial X_w}\right|_{X_w^*} = 0 \Leftrightarrow -A(P_1 - P_2) = 0, \tag{5.38}$$

This relation is indeed the same as the steady state condition (4.8). Therefore, we have shown that the extrema correctly predicts the steady states in the movable wall model.

Next, we check the properties of the extrema for a movable wall model with $N_1 = N_2 = N/2$. Equivalently, it is to check the positivity of the second order derivative $\partial^2 B/\partial X_w^2$ at extrema $X_w^{(i)}, i = 1,2,3$, given by the solutions X_w^* of Eq. (5.38). In particular, $X_w^{(i)}$ is a local maximum if $(\partial^2 B/\partial X_w^2)(X_w^{(i)}) < 0$, and a local minimum if $(\partial^2 B/\partial X_w^2)(X_w^{(i)}) > 0$.

The second order derivative of B is explicitly

$$\begin{aligned}\left.\frac{\partial^2 B}{\partial X_w^2}\right|_{X_w^{(i)}} &\Leftrightarrow -\frac{\partial}{\partial x_w}\left.\left(\frac{f(\widetilde{\lambda}(1+x_w)^2)}{1+x_w} - \frac{f(\widetilde{\lambda}(1-x_w)^2)}{1-x_w}\right)\right|_{x_w^{(i)}} \\ &\Leftrightarrow G'(x_w)\Big|_{x_w^{(i)}},\end{aligned} \tag{5.39}$$

where we have used $G(x_w)$ defined in Eq. (4.10). The properties of $G(x)$ has been discussed in Sec. 4.1.3. In particular, it has been shown that beyond the transition point, $G'(0) < 0$. This suggests that $X_w^{(1)} = 0$ corresponds to a local maximum. Furthermore, since $G(1) > G(0)$, the derivative at the crossing point $X_w^{(2)} > 0$ must be positive, and $G'(x_w^{(2)}) > 0$. This suggests that solution 2 is a local minimum. Finally, since $G(x)$ is an odd function, $G'(-x_w) = G'(x_w)$ and the crossing point $X_w^{(3)} < 0$ is also a local minimum. In other words, the minimum points of B are at $X_w^{(2)}$ and $X_w^{(3)} \neq 0$, which correspond to stable steady states; B at $X_w^{(1)} = 0$ corresponds to the unstable steady state. This conclusion is in accordance with the analysis in Sec. 4.1.2. Hence, the minimization of B correctly predicts the stable steady states of the movable wall model.

5.3 Summary and Conclusion

In this chapter, we have proposed our last hypothesis: the minimization of potential B, an analogous of the Helmholtz free energy. Our description mimics the description of equilibrium thermodynamics (see Sec. 1.1.1): the complete set of nonequilibrium thermodynamic variables and the differential form of B are proposed.

Using the ideal gas model, we have derived the explicit form of B and its integral form. From this expression, the steady state functions – pressure P, entropy S, and chemical potential μ – are obtained. We have performed consistency checks using the Maxwell relations. And in the equilibrium limit, all expressions correctly reduce to their equilibrium value. Further, using the movable wall model, we have shown that the minimization hypothesis correctly predicts the stable steady states.

This description potentially opens up a new direction for nonequilibrium thermodynamics. Remember that in equilibrium thermodynamics (as described in Sec. 1.1), all thermodynamic information can be obtained from the thermodynamic potentials. The discovery of the correct form of the nonequilibrium thermodynamics potential may allow us to have a full description of the nonequilibrium steady state.

Chapter 6

Conclusion and Perspectives

In this thesis, we went on a journey of searching for a possible potential that exhibits extremum in nonequilibrium steady states (NESS). Just as in equilibrium thermodynamics, where a thermodynamic potential contains all thermodynamic information of the system and accompanies a variational principle, we look for a nonequilibrium thermodynamic potential that would provide the same properties for NESS. This is a less common approach to nonequilibrium physics. An introduction to the history and some important results of nonequilibrium physics is given in Chapter 1 for a general picture of the field. To achieve our purpose, we have proposed mainly three hypotheses, or more precisely, forms of three potentials hypothesized to be minimized in steady states. And these hypotheses are examined in a variety of models. This forms the main message of this thesis.

The examination methodology is discussed in Sec. 2.1. Particularly, for a general system, we measure the potential of the constrained system and compare it with its unconstrained value; for systems with competing steady states, we measure the potential of all steady states and compare. Most of our hypotheses are of the form of minimization hypotheses, where it predicts that the potential of the constrained system is greater than that of the unconstrained system; the potential of the stable steady state would be the smallest among all steady states. And for a maximization hypothesis, the predictions will be reversed.

In Chapter 2, we have studied our first hypothesis where a quantity $\mathcal{T}$, defined as the ratio of energy storage (with respect to the equilibrium energy) to the total heat flow, is minimized in NESS (Hypothesis 2.1.1). This quantity has the physical interpretation, from the Lennard-Jones fluid simulation (Sec. 2.2.2), of the (initial) characteristic time of energy dissipation. The hypothesis is driven by the intuition that the system would "prefer" to return to equilibrium, and hence the "time" is hypothesized to be minimum.

This hypothesis is examined most extensively. According to the energy supply method, the test models were grouped into three. First, under the external bulk energy supply scheme, we have analysed the ideal gas under five different supply functions in Sec. 2.2.1. Then, molecular dynamics (MD) simulation results of the Lennard-Jones fluid are recounted in Sec. 2.2.2. Second, under the external energy flow, an ideal gas driven by a temperature gradient has been studied numerically using the finite element method in Sec. 2.3.1; a Hagen-Poiseuille flow was studied analytically in Sec. 2.3.2; to complete the section, the MD simulation results of a Rayleigh-Bénard system was presented in Sec. 2.3.3. Third, in Sec. 2.4, we have considered a variety of periodic inhomogeneous energy supply schemes, and the base model is an Ising model. The results are obtained using a combination of the deterministic Ising algorithm and the Monte Carlo method. Eventually, all results are in accordance with the predictions of Hypothesis 2.1.1.

However, at the end of the chapter, a counterexample – an ideal gas attached with a heat tank – is studied. We have shown that the resulting potential of the constrained system, depending on the size of the tank, may be smaller than the unconstrained one – a contradiction to the hypothesis. This model motivated us to change our hypothesis.

In Chapter 3, an adaptation of Hypothesis 2.1.1 is presented, where the central potential is a quantity called the embedded energy U^* (Hypothesis 3.1.1). U^* is defined as the Legendre transform of the steady state energy with respect to the heat flow. The motivation of this form is the Helmholtz free energy, where it is the Legendre transform of the energetic fundamental relation with respect to entropy. This hypothesis was first tested with the ideal gas under a homogeneous energy supply and the case where a heat tank is attached (which had disproved Hypothesis 2.1.1). Results are in accordance with the hypothesis. However, the study of the second model – an ideal gas under an external heat flow – does not support this hypothesis. Therefore, Hypothesis 3.1.1 was discarded.

Finally, in Chapter 5, we have hypothesized the minimization of a Helmholtz-like potential B in NESS, for a closed system of a fixed volume and number of particles and placed in a heat bath. The form of B is introduced through a series of postulates (5.1.1, 5.1.2, and 5.1.3). The motivation is the correspondence principle. According to which, in the equilibrium limit, B should have the same form as the Helmholtz free energy. Therefore, the differential form of B is postulated to resemble the differential form of the Helmholtz free energy, with an additional term X to account for the contribution from nonequilibrium; this additional term is proportional to $\mathcal{T}$. The thermodynamic parameters are postulated to be temperature, volume, number of particles, and the control parameter (conjugate with X).

Using the ideal gas model under a homogeneous energy supply, we derive the expression of B. And just like equilibrium thermodynamic, we have obtained the state functions from B. We have performed consistency checks of these expressions: they satisfy the Maxwell relations; in the equilibrium limit, their forms correctly reduce to their equilibrium counterparts. Then, this hypothesis is tested using the movable wall model – a model exhibiting multiple steady states. We found that the hypothesis correctly predicts the stable steady states. The explanation of the movable wall model is recounted later.

This hypothesis may open up new directions for studying nonequilibrium thermodynamics. It is an example of generalising equilibrium thermodynamic potentials and techniques to nonequilibrium steady states. It would be interesting for future studies to examine the validity of B for other closed systems and generalise it to systems under other types of external constraints using the Legendre transform.

Along with the study of energy storage and the total heat flow in Hypothesis 2.1.1, we have also studied how the former is influenced by the latter. Using the Ising model in Sec. 2.4, we have compared energy storage under a fixed amount of energy supply (and therefore, the same amount of total heat flow in NESS) but delivered using different methods. We found that energy storage in steady states depends not only on the total energy delivered, but also on the details of the supply method. Specifically, energy storage is influenced by the ratio of the amplitude and time-period of the supply, and the area of delivery.

Particularly, we have found that the system stores more energy under rare and large energy delivery than small and frequent delivery; more energy storage when the delivery area is large than small. The shape of the lattice may also influence the final energy storage, and it would be interesting in future studies to analyse energy storage of different shapes of delivery area and over different lattice types.

The problem of energy storage efficiency has important real-world applications. A better understanding of energy storage under the influence of delivery methods is essential to this problem.

The last important message of this thesis is the discovery of the movable wall model. In Chapter 4, we have described a simple model – an ideal gas under a homogeneous energy supply, with an adiabatic movable wall as the internal constraint – that exhibits nonequilibrium phase transition. The order parameter is the (stable) steady state position of the wall. Beyond the critical energy supply density, the system exhibits multiple steady states. The system is more stable when the subsystems are not symmetric (the wall is not in the center) and stores more energy in the stable steady state.

This model has a simple setting and is analytical. Models that exhibit nonequilibrium phase transition, which can be calculated analytically, are extremely rare. Therefore, this model has the potential to be a paradigm model for nonequilibrium physics.

For us, this model has been instrumental. All hypotheses have been tested using this model (Sec. 4.2 and Sec. 5.2.2). Furthermore, we have generalised the expressions of various thermodynamic potentials to NESS (and the entropy production rate) using the local equilibrium assumption in Sec. 4.3. All of these expressions have been tested using the movable wall model.

At the time of preparing this thesis, potential B in Chapter 5 was our latest hypothesis. This thesis will end here, but our search for nonequilibrium variational principles and the study of nonequilibrium physics will continue. So will the author's interest in this field and its intriguing phenomena around us. The author hopes to continue this adventure and bring back new information in the future.

Bibliography

[1] R. Hołyst, A. Maciołek, Y. Zhang, M. Litniewski, P. Knychała, M. Kasprzak, and M. Banaszak. “Flux and storage of energy in nonequilibrium stationary states”. In: *Phys. Rev. E* 99 (2019), p. 042118.

[2] Y. Zhang, R. Hołyst, and A. Maciołek. “Energy storage in steady states under cyclic local energy input”. In: *Phys. Rev. E* 101 (2020), p. 012127.

[3] Y. Zhang, K. Giżyński, A. Maciołek, and R. Hołyst. “Storage of energy in constrained non-equilibrium systems”. In: *Entropy* 22 (2020), p. 557.

[4] Y. Zhang, M. Litniewski, K. Makuch, P. J. Zuk, A. Maciolek, and R. Holyst. “Continuous non-equilibrium transition driven by the heat flow”. In: (2021). arXiv: `2103.12765`.

[5] I. Prigogine. *Introduction to thermodynamics of irreversible processes*. 3rd. New York: Wiley, 1965.

[6] R. Penrose. *The road to reality: a complete guide to the laws of the universe*. London: Random house, 2005.

[7] C. Rovelli. *Seven brief lessons on physics*. Allen Lane, 2016.

[8] É. Fodor and M. C. Marchetti. “The statistical physics of active matter: from self-catalytic colloids to living cells”. In: *Physica A* 504 (2018), p. 106.

[9] U. Seifert. “Stochastic thermodynamics, fluctuation theorems and molecular machines”. In: *Rep. Prog. Phys.* 75 (2012), p. 126001.

[10] T. Chou, K. Mallick, and R. K. P. Zia. “Non-equilibrium statistical mechanics: from a paradigmatic model to biological transport”. In: *Rep. Prog. Phys.* 74 (2011), p. 116601.

[11] S. Toyabe, T. Sagawa, M. Ueda, E. Muneyuki, and M. Sano. “Experimental demonstration of information-to-energy conversion and validation of the generalized Jarzynski equality”. In: *Nature Phys.* 6 (2010), p. 988.

[12] C. Bechinger, R. Di Leonardo, H. Löwen, C. Reichhardt, G. Volpe, and G. Volpe. “Active particles in complex and crowded environments”. In: *Rev. Mod. Phys.* 88 (2016), p. 045006.

[13] W. Ebeling and I. Sokolov. *Statistical thermodynamics and stochastic theory of nonequilibrium systems*. Singapore: World Scientific, 2005.

[14] S. Carnot. *Réflexions sur la puissance motrice du feu et sur les machines propres à développer cette puissance*. Paris: Bachelier, 1824.

[15] J. W. Gibbs. *Elementary principles in statistical mechanics: developed with especial reference to the rational foundations of thermodynamics*. New York: Scribner, 1902.

[16] S. R. de Groot and P. Mazur. *Non-Equilirbium Thermodynamics*. Amsterdam: North-Holland, 1962.

[17] D. Kondepudi and I. Prigogine. *Modern thermodynamics: from heat engines to dissipative structures*. 2nd. New York: Wiley, 1998.

[18] L. Onsager. "Reciprocal relations in irreversible processes. I.". In: *Phys. Rev.* 37 (1931), p. 405.

[19] L. Onsager. "Reciprocal relations in irreversible processes. II.". In: *Phys. Rev.* 38 (1931), p. 2265.

[20] L. Boltzmann. "Weitere Studien über das Wärmegleichgewicht unter Gasmolekülen." In: *Sitz.-Ber. Akad. Wiss. Wien* 66 (1872). (Reprinted and translated in S. G. Brush, *Kinetic theory volume 2: irreversible processes*, Oxford: Pergamon Press, 1966), p. 275.

[21] N. Pottier. *Nonequilibrium statistical physics: linear irreversible processes*. New York: Oxford University Press, 2010.

[22] R. Kubo, M. Toda, and N. Hashitsume. *Statistical physics II: nonequilibrium statistical mechanics*. 2nd. Berlin: Springer, 1991.

[23] R. Kubo. "The fluctuation-dissipation theorem". In: *Rep. Prog. Phys.* 29 (1966), p. 255.

[24] U. Marconi, A. Puglisi, L. Rondoni, and A. Vulpiani. "Fluctuation-dissipation: response theory in statistical physics". In: *Phys. Rep.* 461 (2008), p. 111.

[25] N. G. Van Kampen. *Stochastic processes in physics and chemistry*. 3rd. Amsterdam: North-Holland, 2007.

[26] C. W. Gardiner et al. *Handbook of stochastic methods: for physics, chemistry and natural sciences*. 3rd. Berlin: Springer, 2004.

[27] R. Rao and M. Esposito. "Nonequilibrium thermodynamics of chemical reaction networks: wisdom from stochastic thermodynamics". In: *Phys. Rev. X* 6 (2016), p. 041064.

[28] C. Bustamante, J. Liphardt, and F. Ritort. "The nonequilibrium thermodynamics of small systems". In: *Phys. Today* 58 (2005), p. 43.

[29] G. Gallavotti and E. G. Cohen. "Dynamical ensembles in nonequilibrium statistical mechanics". In: *Phys. Rev. Lett.* 74 (1995), p. 2694.

[30] J. L. Lebowitz and H. Spohn. "A Gallavotti–Cohen-type symmetry in the large deviation functional for stochastic dynamics". In: *J. Stat. Phys.* 95 (1999), p. 333.

[31] J. Kurchan. "Fluctuation theorem for stochastic dynamics". In: *J. Phys. A: Math. Gen.* 31 (1998), p. 3719.

[32] D. J. Evans and D. J. Searles. "Equilibrium microstates which generate second law violating steady states". In: *Phys. Rev. E* 50 (1994), p. 1645.

[33] C. Jarzynski. "Nonequilibrium equality for free energy differences". In: *Phys. Rev. Lett.* 78 (1997), p. 2690.

[34] G. E. Crooks. "Path-ensemble averages in systems driven far from equilibrium". In: *Phys. Rev. E* 61 (2000), p. 2361.

[35] U. Seifert and T. Speck. "Fluctuation-dissipation theorem in nonequilibrium steady states". In: *Europhys. Lett.* 89 (2010), p. 10007.

[36] M. Baiesi and C. Maes. "An update on the nonequilibrium linear response". In: *New J. Phys.* 15 (2013), p. 013004.

[37] H. Touchette. "The large deviation approach to statistical mechanics". In: *Phys. Rep.* 478 (2009), p. 1.

[38] R. Marsland III and J. England. "Limits of predictions in thermodynamic systems: a review". In: *Rep. Prog. Phys.* 81 (2017), p. 016601.

[39] A. C. Barato and U. Seifert. "Thermodynamic uncertainty relation for biomolecular processes". In: *Phys. Rev. Lett.* 114 (2015), p. 158101.

[40] T. R. Gingrich, J. M. Horowitz, N. Perunov, and J. L. England. "Dissipation bounds all steady-state current fluctuations". In: *Phys. Rev. Lett.* 116 (2016), p. 120601.

[41] J. M. Horowitz and T. R. Gingrich. "Proof of the finite-time thermodynamic uncertainty relation for steady-state currents". In: *Phys. Rev. E* 96 (2017), p. 020103.

[42] C. Maes. "Frenesy: time-symmetric dynamical activity in nonequilibria". In: *Phys. Rep.* 850 (2020), p. 1.

[43] E. T. Jaynes. "Information theory and statistical mechanics". In: *Phys. Rev.* 106 (1957), p. 620.

[44] E. T. Jaynes. "Information theory and statistical mechanics. II". In: *Phys. Rev.* 108 (1957), p. 171.

[45] E. T. Jaynes. "On the rationale of maximum-entropy methods". In: *Proc. IEEE* 70 (1982), p. 939.

[46] M. Polettini and M. Esposito. "Effective fluctuation and response theory". In: *J. Stat. Phys.* 176 (2019), p. 94.

[47] H. B. Callen. *Thermodynamics and an introduction to thermostatistics*. 2nd. New York: Wiley, 1985.

[48] N. Borghini. *Topics in nonequilibrium physics*. 2012.

[49] R. K. P. Zia, E. F. Redish, and S. R. McKay. "Making sense of the Legendre transform". In: *Am. J. Phys.* 77 (2009), p. 614.

[50] L. Boltzmann. *Lectures on gas theory*. Trans. by S. G. Brush. New York: Dover, 1995.

[51] M. Toda, R. Kubo, and N. Saito. *Statistical physics I: equilibrium statistical mechanics*. 2nd. Berlin: Springer, 1992.

[52] R. Livi and P. Politi. *Nonequilibrium statistical physics: a modern perspective*. Cambridge: Cambridge University Press, 2017.

[53] P. Curie. "Sur la symétrie dans les phénomènes physiques, symétrie d'un champ électrique et d'un champ magnétique". In: *J. Phys. Theor. Appl.* 3 (1894), p. 393.

[54] M. Polettini. "Macroscopic constraints for the minimum entropy production principle". In: *Phys. Rev. E* 84 (2011), p. 051117.

[55] G. B. Arfken and H. J. Weber. *Mathematical methods for physicists*. 6th. Amsterdam: Elsevier, 2005.

[56] R. Brown, F.R.S., Hon. M.R.S.E. & R.I. Acad., V.P.L.S.. "XXVII. A brief account of microscopical observations made in the months of June, July and August 1827, on the particles contained in the pollen of plants; and on the general existence of active molecules in organic and inorganic bodies". In: *Philos. Mag.* 4 (1828), p. 161.

[57] A. Einstein. "Zur Theorie der Brownschen Bewegung". In: *Ann. Phys.* 19 (1906), p. 371.

[58] A. Einstein. "Über die von der molekularkinetischen Theorie der Wärme geforderte Bewegung von in ruhenden Flüssigkeiten suspendierten Teilchen". In: *Ann. Phys.* 4 (1905).

[59] V. M. Smoluchowski. "Zur kinetischen Theorie der Brownschen Molekular Bewegung und der Suspensionen". In: *Ann. Phys.* 21 (1906), p. 756.

[60] C. Maes. "On the origin and the use of fluctuation relations for the entropy". In: *Séminaire Poincaré* 2 (2003), p. 29.

[61] R. Hołyst and M. Litniewski. "Heat transfer at the nanoscale: evaporation of nanodroplets". In: *Phys. Rev. Lett.* 100 (2008), p. 055701.

[62] M. L. Boas. *Mathematical methods in the physical sciences*. 3rd. USA: Wiley, 2006.

[63] A. Rahman. "Correlations in the Motion of Atoms in Liquid Argon". In: *Phys. Rev.* 136 (1964), A405.

[64] D. C. Rapaport. *The art of molecular dynamics simulation*. 2nd. Cambridge: Cambridge University Press, 2004.

[65] N. Gershenfeld. *The nature of mathematical modeling*. Cambridge: Cambridge University Press, 1999.

[66] H. P. Langtangen and K. A. Mardal. *Introduction to numerical methods for variational problems*. Switzerland: Springer Nature, 2019.

[67] J. N. Reddy. *An introduction to the finite element method*. 3rd. Boston: McGraw-Hill, 2006.

[68] W. P. Graebel. *Advanced fluid mechanics*. Amsterdam: Academic Press, 2007.

[69] M. E. J. Newman and G. T. Barkema. *Monte Carlo methods in statistical physics*. New York: Oxford University Press, 1999.

[70] M. Creutz. "Deterministic Ising dynamics". In: *Ann. Phys.* 167 (1986), p. 62.

[71] M. Creutz. "Microcanonical Monte Carlo simulation". In: *Phys. Rev. Lett.* 50 (1983), p. 1411.

[72] G. Bhanot, M. Creutz, and H. Neuberger. "Microcanonical simulation of Ising systems". In: *Nucl. Phys. B* 235 (1984), p. 417.

[73] B. Schmittmann and R. K. P. Zia. "Statistical mechanics of driven diffusive systems". In: *Phase transitions and critical phenomena*. Vol. 17. London: Academic Press, 1995.

[74] D. P. Landau and K. Binder. *A guide to Monte Carlo simulations in statistical physics*. 4th. Cambridge: Cambridge University Press, 2015.

[75] K. Binder, D. Landau, and M. Müller. "Monte Carlo studies of setting, interface localization and capillary condensation". In: *J. Stat. Phys.* 110 (2003), p. 1411.

[76] J. Marro and R. Dickman. *Nonequilibrium phase transitions in lattice models*. Cambridge: Cambridge University Press, 2005.

[77] S. Katz, J. L. Lebowitz, and H. Spohn. "Nonequilibrium steady states of stochastic lattice gas models of fast ionic conductors". In: *J. Stat. Phys.* 34 (1984), p. 497.

[78] D. Mukamel. "Phase transitions in nonequilibrium systems". In: *Soft and fragile matter*. Ed. by M. E. Cates and M. R. Evans. Bristol: Institute of Physics, 2000.

[79] M. R. Evans, D. P. Foster, C. Godrèche, and D. Mukamel. "Spontaneous symmetry breaking in a one dimensional driven diffusive system". In: *Phys. Rev. Lett.* 74 (1995), p. 208.

[80] B. Derrida, E. Domany, and D. Mukamel. "An exact solution of a one-dimensional asymmetric exclusion model with open boundaries". In: *J. Stat. Phys.* 69 (1992), p. 667.

[81] N. Metropolis, A. W. Rosenbluth, M. N. Rosenbluth, A. H. Teller, and E. Teller. "Equation of state calculations by fast computing machines". In: *J. Chem. Phys.* 21 (1953), p. 1087.

[82] N. Aktekin. "The simulation of the Ising model on the Creutz cellular automaton". In: *Annual Reviews of Computational Physics VII*. Ed. by D. Stauffer. Singapore: World Scientific, 2000, p. 1.

[83] J. Casas-Vazquez and D. Jou. "Temperature in non-equilibrium states: a review of open problems and current proposals". In: *Rep. Prog. Phys.* 66 (2003), p. 1937.

[84] G. Y. Vichniac. "Simulating physics with cellular automata". In: *Physica D* 10 (1984), p. 96.

[85] I. Ponomareva and S. Lisenkov. "Bridging the macroscopic and atomistic descriptions of the electrocaloric effect". In: *Phys. Rev. Lett.* 108 (2012), p. 167604.

[86] A. Lederhendler and D. Mukamel. "Long-range correlations and ensemble inequivalence in a generalized ABC model". In: *Phys. Rev. Lett.* 105 (2010), p. 150602.

[87] K. Saito, S. Takesue, and S. Miyashita. "Transport phenomena at a critical point: thermal conduction in the Creutz cellular automaton". In: *Phys. Rev. E* 59 (1999), p. 2783.

[88] R. Harris and M. Grant. "Thermal conductivity of a kinetic Ising model". In: *Phys. Rev. B* 38 (1988), p. 9323.

[89] M. Neek-Amal, R. Moussavi, and H. R. Sepangi. "Monte Carlo simulation of size effects on thermal conductivity in a two-dimensional Ising system". In: *Physica A* 371 (2006), p. 424.

[90] J. Muglia and E. V. Albano. "Dynamical and stationary critical behavior of the Ising ferromagnet in a thermal gradient". In: *Euro. Phys. J. B* 85 (2012), p. 258.

[91] M. Casartelli, N. Macellari, and A. Vezzani. "Heat conduction in a two-dimensional Ising model". In: *Euro. Phys. J. B* 56 (2007), p. 149.

[92] Y. Masumoto and S. Takesue. "Characteristic power spectrum of diffusive interface dynamics in the two-dimensional Ising model". In: *Phys. Rev. E* 97 (2018), p. 052141.

[93] Y. Masumoto and S. Takesue. "Diffusion of interface and heat conduction in the three-dimensional Ising model". In: *Phys. Rev. E* 99 (2019), p. 052128.

[94] L. Glass and M. C. Mackey. *From clocks to chaos: the rhythms of life*. Princeton: Princeton University Press, 1988.

[95] S. W. Sides, P. A. Rikvold, and M. A. Novotny. "Kinetic Ising model in an oscillating field: finite-size scaling at the dynamic phase transition". In: *Phys. Rev. Lett.* 81 (1998), p. 834.

[96] T. Tomé and M. J. de Oliveira. "Dynamic phase transition in the kinetic Ising model under a time-dependent oscillating field". In: *Phys. Rev. A* 41 (1990), p. 4251.

[97] B. K. Chakrabarti and M. Acharyya. "Dynamic transitions and hysteresis". In: *Rev. Mod. Phys.* 71 (1999), p. 847.

[98] L. Li and M. Pleimling. "Formation of nonequilibrium modulated phases under local energy input". In: *Europhys. Lett.* 98 (2012), p. 30004.

[99] F. Cottone, H. Vocca, and L. Gammaitoni. "Nonlinear energy harvesting". In: *Phys. Rev. Lett.* 102 (2009), p. 080601.

Acknowledgements

I want to thank everyone who has encouraged and helped me during my Ph.D. studies. Without their support, this thesis would not have been possible — particularly Dr. Anna Maciołek and Prof. Robert Hołyst. I am especially grateful to Dr. Anna Maciołek for providing me the opportunity of this doctoral study. Moreover, for the guidance, discussion, and help she has provided. I am also deeply thankful to Prof. Robert Hołyst for the discussions and career advice, his help, and support during my study. I have also benefited greatly from the scientific discussions with Dr. Karol Makuch and Dr. Paweł Żuk. In addition to their knowledge and expertise, they also make the journey of discovery much more enjoyable. Scientifically, these are the people who have helped me the most.

In addition, I want to thank Patrycja Kuźma for her help with administrative affairs during the past year. Also, to group members, both past and present, whose kindness has generated a friendly work environment. This thesis is partially supported by Polish National Science Centre (Harmonia Grant No.187 2015/18/M/ST3/00403).

Finally, I am grateful to my parents and friends who have supported me during this Ph.D. study. Their care and attention have been crucial to me in facing this challenging process and various unique obstacles related to the current pandemic. My friends, especially Piero, Mahsa, Qing-Yuan, and Milutin, have repeatedly helped me regain confidence and encouraged me to go the extra mile. From time to time, I am amazed by the goodwill from people around me: they far outshine the negativity. I often forget about this, only to be reminded again during difficult times. Thank you all for your help and all the effort it might have taken.

Institute of Physical Chemistry
Polish Academy of Sciences

Kasprzaka 44/52
01-224 Warsaw, Poland

www.ichf.edu.pl